



Advancing the representation of flows along topography in z-coordinate ocean models

Antoine-Alexis Nasser

► To cite this version:

Antoine-Alexis Nasser. Advancing the representation of flows along topography in z-coordinate ocean models. Ocean, Atmosphere. Sorbonne Université, 2023. English. NNT : 2023SORUS446 . tel-04399405

HAL Id: tel-04399405

<https://theses.hal.science/tel-04399405>

Submitted on 17 Jan 2024

HAL is a multi-disciplinary open access archive for the deposit and dissemination of scientific research documents, whether they are published or not. The documents may come from teaching and research institutions in France or abroad, or from public or private research centers.

L'archive ouverte pluridisciplinaire **HAL**, est destinée au dépôt et à la diffusion de documents scientifiques de niveau recherche, publiés ou non, émanant des établissements d'enseignement et de recherche français ou étrangers, des laboratoires publics ou privés.



Distributed under a Creative Commons Attribution 4.0 International License



THESE DE DOCTORAT DE SORBONNE UNIVERSITE

Ecole Doctorale : 129 - Sciences de l'Environnement d'Ile de France

Spécialité : Océanographie Physique

réalisée au

Laboratoire Jean Kuntzmann

et au

Laboratoire d'Océanographie et du Climat: Expérimentations et Approches
Numériques

présentée par

Antoine-Alexis NASSER

pour obtenir le grade de

Docteur de Sorbonne Université

Titre de la thèse

Advancing the representation of flows along topography in z-coordinate ocean models

Soutenue le 21 septembre 2023 devant le jury composé de :

Rapporteur	David Marshall	Oxford University
Rapporteur	Nicholas Kevlahan	McMaster University
Présidente du jury	Pascale Bouruet-Aubertot	LOCEAN, Paris
Examinatrice	Anne-Marie Tréguier	LOPS, Brest
Examineur	Patrick Marchesiello	LEGOS, Toulouse
Directeur de thèse	Gurvan Madec	LOCEAN, Paris
Directeur de thèse	Laurent Debreu	LJK, Grenoble
Encadrant de thèse	Casimir de Lavergne	LOCEAN, Paris



Abstract

Variations in seafloor depth exert a major control on ocean circulation. The discrete representation of marine topography in geopotential Ocean General Circulation Models (OGCMs) creates artificial steps that have adverse effects on the simulated circulation. This thesis aims at finding suitable ways to address the adverse effects of stepped topography in z-coordinate OGCMs. Using idealised configurations and exploring the potential of the Brinkman Volume Penalisation (BVP) method, we investigate the sensitivity of modelled currents to the presence of artificial steps along model boundaries.

We first address the spurious lateral form drag (or *staircase problem*) highlighted by Adcroft and Marshall (1998). First, to become insensitive to staircase coastlines (or isobaths), numerical models should ideally achieve physical convergence (i.e. the main characteristics of the flow are not affected by increasing spatial resolution while keeping viscous and frictional parameters constant). This convergence can be attained at lower resolution with a careful treatment of discrete momentum advection involving a large stencil.

Second, the application of free-slip as a *true* mirror condition makes step-like coastlines slippery for all numerical formulations. It is shown that the usual discrete implementation of free-slip using a symmetric viscous stress tensor and flux-form advection actually corresponds to no-slip along step-like topography. Furthermore, we demonstrate that the detachment of a vortex flowing past an outgoing corner of the coastline is missed with a free-slip condition at the corner. The choice of viscous boundary condition should thus vary with location to represent both the detachment of boundary currents at a cape and the unperturbed flow along a smooth continuous coastline.

We also highlight the impact of momentum advection schemes on the fidelity of simulated downslope currents within an idealised overflow configuration. The BVP method allows to spread the land-ocean interface, by introducing porous cells that are part land part ocean. We find that this spreading allows to smooth bottom currents and to reduce spurious mixing during downslope flow.

It is shown that the representation of topography with the BVP method provides a better alternative to the use of shaved-cells (Adcroft et al. 1997). The numerical stability of the BVP, without modifying the reference time-step of the simulation, can be guaranteed by sufficient spreading of the porous boundary and by defining friction within porous cells in a consistent way. The results underscore the potential of the BVP method to better represent flows along topography in OGCMs.

Résumé

Les variations de profondeur du fond des océans exercent un contrôle majeur sur la circulation de l'océan. La représentation discrète de la topographie dans les modèles de circulation générale océanique (OGCMs) géopotentiels crée des marches artificielles qui ont des effets néfastes sur la simulation des courants. Cette thèse vise à établir des solutions adaptées pour résoudre les effets adverses des marches dans les OGCMs. En utilisant des configurations idéalisées et en explorant le potentiel de la méthode de Pénalisation des Volumes de Brinkman (BVP), nous étudions la sensibilité des courants modélisés aux frontières en marche d'escalier.

Il est montré comment résoudre le "spurious form drag" latéral (ou "staircase problem") mis en évidence par Adcroft et Marshall (1998). Pour devenir insensible aux lignes de côtes (ou isobathes) en marche d'escalier, les modèles numériques devraient idéalement être physiquement convergés (c'est-à-dire que les caractéristiques principales de l'écoulement ne sont pas affectées par l'augmentation de la résolution spatiale en conservant les paramètres de viscosité et de friction constants). Cette convergence peut être atteinte à une résolution plus faible par un traitement minutieux de l'advection discrète des moments qui implique des schémas utilisant un stencil élargi.

L'utilisation d'une condition miroir *exacte* pour appliquer le glissement sans frottement rend les lignes de côtes en marche d'escalier glissantes pour toutes les formulations numériques. La formulation usuelle de la condition de glissement sans frottement dans le tenseur visqueux symétrique et l'advection sous forme de flux produit une condition de non-glissement le long des topographies en marche d'escalier. Il est également montré que le détachement d'un vortex au passage d'une marche de la ligne de côte n'est pas capturé avec une condition de glissement sans frottement au coin. Le choix de la condition limite visqueuse devrait donc varier en fonction de l'emplacement pour représenter à la fois le détachement d'un courant à un cap et l'écoulement non perturbé le long d'une ligne de côte continue et lisse.

Nous montrons également l'impact de la résolution discrète des moments sur la précision des écoulements le long des pentes en marche d'escalier à travers une configuration idéalisée d'un "overflow". La méthode de BVP permet d'étaler l'interface terre-océan en définissant des cellules poreuses mi-terres et mi-océans. Il est montré qu'en étalant ainsi l'interface, les courants sont lissés et le mélange artificiel est considérablement réduit pendant la descente.

Il est montré que la représentation de la topographie avec la BVP offre une meilleure alternative à l'utilisation des "shaved cells" (Adcroft et al. 1997). La stabilité numérique de la BVP, sans modification du pas de temps de référence de la simulation, peut être garantie en étalant suffisamment la frontière, et en définissant de manière cohérente la friction dans les cellules poreuses. Les résultats soulignent le potentiel de la méthode de BVP pour une meilleure représentation des courants le long de la topographie dans les OGCMs.

List of Figures

1	'World Ocean Floor' map from (Berann et al., 1977)	14
2	Discrete representation of topography in a z -coordinate model	18
3	From (Deremble et al., 2016) (their figure 3)	19
4	From Adcroft and Marshall (1998) (adaption of their figure 3 and figure 8e,f)	20
5	Idealisation of a barotropic flow across a slope (inspired from Adcroft, Hill, and Marshall (1997)).	24
II.1	The Arakawa C grid. Location of T nodes (black circle) and (u,v,w,f) nodes (grey circles) on a single unit cell. This figure is derived from (Madec & NEMO System Team, 2022).	56
II.2	Schematic illustration depicting the representation of a steep topographic slope intersecting a numerical cell.	60
II.3	Factors r_x and r_{ux} with various level of smoothing.	62
III.1	Evolution of the temperature field during the overflow.	73
III.2	Snapshots of the overflow simulations solved in z -coordinate with partial bottom cells, for the four combinations of advection schemes listed in Table III.1.	78
III.3	Snapshots of the overflow simulations solved in s -coordinate, for the four combinations of advection schemes listed in Table III.1. Bathymetry is shaded in grey.	79
III.4	Temperature distribution of waters reaching the foot of the slope, accumulated until a total volume of 20 Gm^3 has crossed $x = 60 \text{ km}$.	81
III.5	Snapshots of the overflow simulations solved in z -coordinate with BVP and a varying degree of porosity smoothing.	85
III.6	Temperature distribution of dense waters reaching the foot of the slope at $x = 60 \text{ km}$.	87
III.7	Snapshots of the overflow simulations solved in z -coordinate and s -coordinate with a smoothed topography.	88
III.8	Diagram of simulated overflows for the conservation of dense waters.	90
IV.1	Steady state of the linear solutions. Shading and isolines (in black) depict the active layer thickness h (the 500 m isoline is thickened).	102
IV.2	Steady state of the linear solutions resorting to the BVP method.	103
V.1	Description of the RIDGE configuration implemented in NEMO.	110



List of Tables

II.1	Location of grid-nodes for a single cell.	56
III.1	Tested combinations of momentum advection formulations, in horizontal and vertical directions, for z -coordinate and s -coordinate systems.	77



Scientific Activities during the thesis

Publications in peer-reviewed scientific journals

Nasser, A.-A., Madec, G., de Lavergne, C., Debreu, L., Lemarié, F., Blayo, E. (2023). *Sliding or stumbling on the staircase: Numerics of ocean circulation along piecewise-constant coastlines*. Journal of Advances in Modeling Earth Systems, 15, [e2022MS003594](#).

Rathore S., de Lavergne C., Sallée J.-B., Madec G., Nasser A.-A., Ethé C. (in preparation). *Effects of improved tidal mixing in NEMO 1° global ocean model*

International Conferences

Nasser, A.-A., Madec, G., de Lavergne, C., Debreu. Finding better numerical solutions for circulation along piecewise-constant coastlines in ocean models, Drakkar 2022, held online.

Nasser, A.-A., Madec, G., de Lavergne, C., Debreu. Finding better numerical solutions for circulation along piecewise-constant coastlines in ocean models, Ocean Science Meeting 2022, held online.

Nasser, A.-A., Madec, G., de Lavergne, C., Debreu. Finding better numerical solutions for circulation along piecewise-constant coastlines in ocean models, EGU General Assembly 2022, held in Vienna (Austria).

Nasser, A.-A., Madec, G., de Lavergne, C., Debreu. Sliding or stumbling on the staircase: numerics of ocean circulation along piecewise-constant coastlines. Drakkar 2023, held in Grenoble.

Seminars

Nasser, A.-A., Madec, G., de Lavergne, C., Debreu. (2021), The Brinkman Volume Penalisation Method for improving the representation of flows along a topography, ANDIAMO research group.

Nasser, A.-A., Madec, G., de Lavergne, C., Debreu. (2021), Searching for better numerical solutions along piecewise-constant coastlines, PhD seminars in LOCEAN.

Nasser, A.-A., Madec, G., de Lavergne, C., Debreu. (2022), Toward better numerical solutions for circulation along piecewise-constant coastlines in ocean models, seminar in UCT in Cape Town (South Africa).

Nasser, A.-A., Madec, G., de Lavergne, C., Debreu. (2023), Sliding down the slope with the volume penalisation technic, ANDIAMO research group.

Oceanographic cruises

BOCATS21-OVIDE cruise: monitored the CTD, took on the role of secretary for samplings on board the Sarmiento de Gamboa (30 days).

Seamster V 2022: Winter school on board the ice-breaker S.A. Aghulas II (10 days).

Activities in the Laboratory

In charge of coordinating a PhD seminar series at LOCEAN (2021-2022), which involved organizing monthly sessions where a PhD student presented their work and engaged in discussions with all the members of the laboratory. Each presentation lasted for approximately 30 minutes. Additionally, shorter sessions were organized for young interns.



Acknowledgements

I would like to start by thanking David Marshall and Nicholas Kevlahan for accepting to review this thesis, Anne-Marie Tréguier and Patrick Marchesiello for accepting to be an examiner and Pascale Bouruet-Aubertot for being the president of the jury of the PhD. Thank you to all of you for your time and dedication.

L'accomplissement de cette thèse a été rendu possible grâce à la présence de nombreuses personnes au cours de ces dernières années.

Je suis profondément reconnaissant envers Gurvan, Laurent et Casimir pour m'avoir accompagné et soutenu tout au long de cette aventure. Merci Gurvan pour ta confiance et ton soutien indéfectible. Merci pour ton optimisme contagieux et ces discussions infinies, à toutes heures, en tous lieux, traitant de la modélisation de l'océan et d'innombrables d'autres sujets. Merci Laurent pour ta confiance, ta gentillesse et ton dévouement. J'ai énormément appris à tes côtés lors de ces précieuses semaines grenobloises. J'aurais simplement adoré descendre plus souvent. Merci Casimir pour ta présence, ta justesse et tes encouragements. Merci d'avoir su trouver les mots dans les moments délicats durant la thèse. Merci d'avoir veillé à ce qu'elle se déroule dans les meilleures conditions.

Je souhaite remercier Anne-Marie Tréguier, Jean-Baptiste Sallée et Patrick Marchesiello d'avoir accepté d'être membres de mon comité thèse et d'avoir pris le temps de me suivre tout au long de cette thèse. Merci pour votre écoute et vos précieux conseils.

Je tiens à remercier Florian Lemarié et Eric Blayo avec qui j'ai eu la chance de collaborer lors de la conception de l'article, ce fut un réel plaisir d'échanger avec vous !

Je souhaite remercier LOCEAN ainsi que le LJK de m'avoir accueilli dans des environnements sains et bienveillants. Je tiens à remercier les admins de chacun des laboratoires pour m'avoir accompagné et sauvé parfois de situations inextricables.

Je suis reconnaissant envers l'équipe NEMO R&D et les formidables personnes qui la composent. Merci Sibylle pour tes milles encouragements, pour nos discussions sur le boulot et la vie en général, mais aussi pour ton aide sur ce fameux bassin carré. Merci Sébastien pour ta soutien, ta bonne humeur, tes conseils avisés sur la vie ainsi que tes tricks sur comment affronter la console de NEMO. Merci Julie pour ta bienveillance et les discussions stimulantes à propos des modèles, merci de m'avoir permis de faire mes premiers pas sur un bateau d'océanographie. Merci Katherine pour ta confiance et tes précieux conseils sur la recherche. Merci mille fois de m'avoir permis d'avoir un glimpse sur l'Afrique du Sud. Merci Martin pour ton humour inventif et tes encouragements, tout a commencé par un entretien avec toi. Merci Christian pour ta gentillesse et ton aide. Merci à toutes les personnes que j'ai eu la chance de rencontrer aux laboratoires du LOCEAN et du LJK, ce fut un plaisir.

I am deeply grateful to Rosa and John Hutchinson for hosting me in Cape Town, for taking care of me with such kindness and attention, and for showing me the beauty of the surroundings from various perspectives.

Merci à Damien, Lidia, Philippe, Michel du LOPS pour votre bonne humeur et votre accueil sur le Sarmiento de Gamboa. Thanks to the hippies for the enjoyment at sea.

Merci à l'infailible famille du LOCEAN, sans vous les journées auraient été bien grises. Merci pour votre bonne humeur, vous constituez l'âme de ce labo. Souvenirs éternels du prince du croissant, de *robins fishing*, du "*coucou* !" de la cantine, des joyeuses pauses cantines/café/gouters/jeux/bières/diners/soirées/beerpongs sauvages, des danses sur les quais, des blagues douteuses, des discussions insensés, de vous. Merci Chab, Kenz, Linux et Diego pour vos relectures *last minute* du manuscrit. Merci à mes teammates de bureau Sara, Gaston, Yona, Clément et Carlos pour m'avoir supporté (pas facile) et nourri de gateaux inventifs et gourmands (et végan).

Merci à ma team ENSTA pour votre soutien, pour votre intérêt constant vis à vis des tréfonds de l'océan et de mes avancées de ma thèse. Merci aux petits suisses pour le ressourcement impromptu au début de la rédaction du manuscrit. Merci à ma team de lycée pour votre soutien et curiosité. Merci à mes amis et à mes proches pour vos encouragements.

A mon père et à ma mère, vous m'encouragez, réconfortez et soutenez sans cesse depuis le premier jour. A ma soeur, tu es ma première fan, ton excitation à propos de ma thèse me dépasse et me motive à la fois. A Laura, tu m'encourages à donner le meilleur de moi-même, merci pour ton aide et ton soutien dans les moments heureux comme dans les moments difficiles.

Τώρα που έφαγες τον ταύρο, θα αφήσεις την ουρά·
Now that you've eaten the calf, will you leave the tail?



Contents

Introduction	13
Facing Obstacles with Step-Wise Topography	17
I Addressing the Lateral Form Drag of Piecewise Constant Coastlines	29
II Advective Stability Condition of the Brinkman Volume Penalisation Method	51
III Addressing the Staircase Effect in Overflows With the Brinkman Volume Penalisation Method	69
IV Toward Global Realistic Simulations	95
V General Conclusion	105
Appendix A: Lipschitz condition for vertical advection	113
References	117

Introduction

The world ocean is central in shaping and regulating Earth's climate. Its vast expanse and tremendous heat capacity make it the primary heat reservoir of the climate system. Between 1971 and 2010, approximately 91% of Earth's energy accumulation due to the greenhouse effect was absorbed by the ocean ([Masson-Delmotte et al., 2021](#)), which thus acts as the planet's thermometer. The ocean also plays a vital role as a conduit for redistributing the excess of energy received from the Sun at the tropics towards the poles. This redistribution occurs mostly via upper ocean currents – from transient small-scale flows to major boundary currents like the Gulf Stream and Kuroshio – and to a smaller extent via deep meridional overturning circulations ([Forget & Ferreira, 2019](#)). On the other hand, these overturning circulations largely determine the ocean's ability to store carbon and heat in deep layers, and therefore impact both transient and equilibrium climate sensitivity to increasing greenhouse forcing ([Marshall & Speer, 2012](#)).

The large-scale ocean circulation is fundamentally shaped by ocean geometry. While the circulation is mostly forced at the surface, it is largely dissipated at the bottom. The depth and shape of the bottom boundary is a critical factor controlling the nature and intensity of dissipative processes, and thereby an essential factor setting the circulation which exists as a balance between sources and sinks of kinetic energy ([Naveira Garabato, 2012](#)).

Furthermore, the bottom boundary has a blocking effect that constrains the allowed circulation patterns and strengths. Unlike the atmosphere, the ocean has a solid boundary (the seafloor) that rises through the entire depth of the fluid. Indeed the ocean is divided by continents into basins. The three major basins are the Atlantic, Indian and Pacific, connected via the Southern Ocean, the Arctic Ocean and the Indonesian Seas. This compartmentalisation of the ocean by continental masses is a zero-order constraint on ocean circulation ([Ferreira et al., 2018](#)).

The blocking effect of the solid bottom boundary is not restricted to continental boundaries: submarine ridges, trenches and mounts create a complex network of underwater basins that channels deep currents and shapes deep overturning circulations ([Ferron et al., 1998](#); [MacKinnon et al., 2008](#)) (Figure 1). This channelling effect on deep ocean flows is augmented by a steering effect that can be felt all the way up to the surface. Such steering stems from a fundamental dynamical constraint on the depth-average component of ocean circulation, which tends to

follow f/H contours where f is the Coriolis frequency and H the seafloor depth (Pedlosky, 1987). Variations in seafloor depth, hereafter referred to as *topography*, thus exert a major constraint on the pathway of major ocean currents, such as western boundary currents (Hughes & Cuevas, 2001; Jackson et al., 2006; Schoonover et al., 2016).

The presence of geothermal heating along the seafloor and the tendency of small-scale turbulence to be intensified near the bottom confer an additional role to the bottom boundary: lightening of deep waters is largely confined to a near bottom layer (Ferrari et al., 2016; Lavergne et al., 2016). As a result, the vertical distribution of the seafloor exerts a major constraint on the upwelling rate and meridional circulation of abyssal waters at basin scale (de Lavergne et al., 2017). More generally, the intensity and distribution of mixing by small-scale turbulence in the ocean interior is tied to topography, which catalyses dissipative processes (Holmes et al., 2019; Naveira Garabato et al., 2013; Melet et al., 2014). Topography thus affects ocean circulation indirectly via its impacts on vertical mixing.

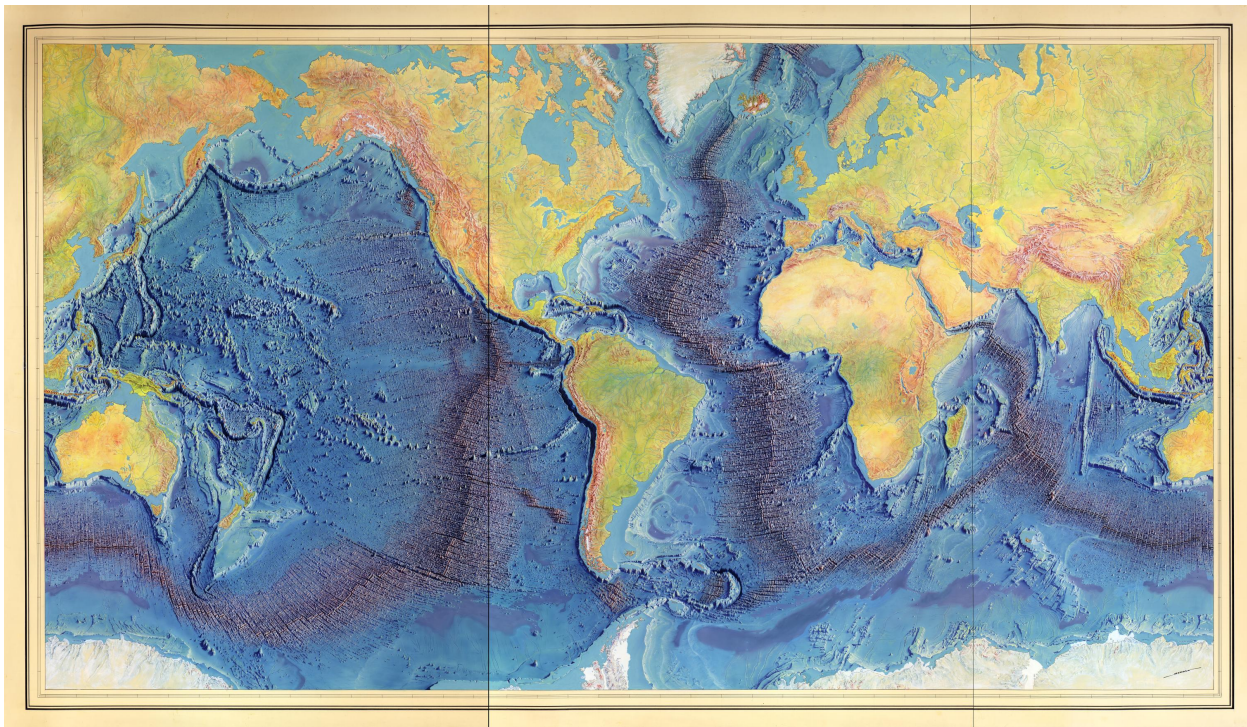


Figure 1: 'World Ocean Floor' map from (Berann et al., 1977). This manuscript painting by Heezen-Tharp portrays the topography of the earth, with continents and their reliefs depicted in shades of green to red. The oceanic depth is represented by varying shades of blue, ranging from light to dark. The fractured mid-ocean ridge is visually emphasized through greyish brushing, illustrating the cracks through which deep water masses can potentially flow. Notably, the map showcases the division of the world ocean floor into underwater basins enclosed by either continents or underwater ridges.

Hence, topography emerges as a primary constraint on the large-scale ocean circulation. Accurate simulation of ocean circulation requires an adequate representation of topography and its impacts on ocean flows. This thesis focuses on investigating methods to improve the representation of flows along topography in Ocean General Circulation Models (OGCMs),

specifically those utilising a z -coordinate for vertical representation, which are known to be susceptible to adverse effects resulting from discrete topographic steps. The limitations of conventional approaches for representing topography in such OGCMs are discussed, with a particular emphasis on addressing issues related to spurious form drag exerted by piecewise constant coastlines and spurious mixing caused by topographic steps encountered by downslope flows. A novel approach called the Brinkman volume penalisation method is introduced and explored as a potential solution for improving the representation of topography in OGCMs.



Facing Obstacles with Step-Wise Topography

The simplicity and maturity of the geopotential (or z) coordinate system have made it the prevailing choice in present-day Oceanic General Circulation Models (OGCMs) ([S. M. Griffies, 2004](#)). In this system, the ocean is discretised into rectangular boxes (or cells) along the three spatial dimensions, forming a connected grid (or mesh) for the model. Within the z -coordinate system, vertical levels align with geopotential surfaces, which greatly facilitates calculations of pressure gradients and seawater densities. However, this gridding approach requires the masking of cells (i.e., excluding them from the calculation domain) below a certain depth, typically the observed or target seafloor, to represent the model topography. As a result, bottom seafloor and coastlines are represented in a step-wise manner, as illustrated in [Figure 2](#).

The representation of topography as a series of steps has implications for various aspects of ocean circulation, impacting both gyre and overturning circulations ([Beckmann & Haidvogel, 1999](#)). Simply increasing spatial resolution to reduce the size of steps does not guarantee the elimination of adverse effects caused by staircase-like topographies ([Adcroft & Marshall, 1998](#)), highlighting the need for a deeper understanding of how boundary currents respond to artificial steps. Furthermore, the ability to increase spatial resolution is limited in climate simulations due to the computational cost of long (order 1000 years) integrations. Finding ways to address nonphysical repercussions of stepped topography is an active area of research and the focus of this thesis. We next present some long-standing issues associated to step-wise boundaries and consider the potential of the novel Brinkman Volume Penalisation method ([Debreu et al., 2022, 2020](#); [Kevlahan et al., 2015](#)) to better represent flow-topography interactions in z -coordinate models. We then summarize recent developments and formulate key questions.

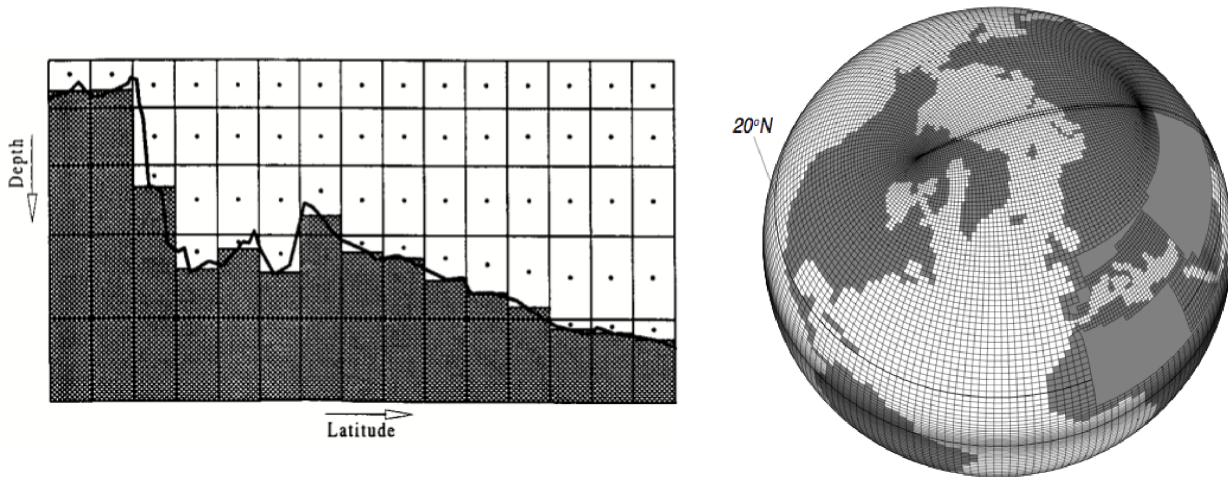


Figure 2: Discrete representation of topography in a z -coordinate model. On the left (from (Pacanowski & Gnanadesikan, 1998), their figure 1), discretized bottom topography for a given horizontal resolution using partial cells. On the right, the ORCA1 grid is shown on a sphere, emphasizing the presence of horizontal staircase coastlines. The ORCA grid is a tripolar grid based on the semi-analytical method of (Madec & Imbard, 1996).

1 Recurrent issues linked to stepped boundaries

Finding the appropriate lateral viscous condition in OGCMs

The presence of vertical sidewalls in the model's stepped topography requires the definition of a lateral viscous boundary condition (Ezer, 2016; Adcroft & Marshall, 1998; Dengg, 1993). Specifying such a condition is a challenging issue with significant implications for the simulated currents. The very presence of vertical sidewalls is artificial since the ocean has a small aspect ratio and therefore only a gently sloping seafloor; this makes it even more difficult to physically base the lateral boundary condition.

The 'no-slip' condition is the physical condition for fluid-solid boundary interactions (Dalibard & Gérard-Varet, 2011; Richardson, 1973). However, its translation into global OGCMs is not straightforward due to the limited spatial resolution (typically 10-100 km in the horizontal) that does not allow the viscous boundary layer to be resolved (Deremble et al., 2011). In such cases, the combined use of bottom drag and a no-slip condition at the sidewall may potentially overestimate frictional boundary effects.

Realistic topography exhibits a fractal nature: it contains features at all scales. Coarse-graining of the target bathymetry is required when constructing the model bathymetry. Moderate smoothing of the bathymetry is sometimes also applied to avoid noise in the simulated solutions (Le Sommer et al., 2009). However, these procedures may suppress some important effects of topographic roughness, such as damping of currents (Özgökmen & Fischer, 2008; Richardson, 1973; Barnier et al., 2006; Smith, 2014).

In practice, slippery or mixed lateral boundary conditions, such as 'free-slip' or 'partial slip,' are often preferred in coarse OGCMs (Penduff et al., 2007). Studies have demonstrated that stochastic boundary conditions based on observed currents yield a mixed response between no-slip and free-slip conditions, advocating for a slippery condition (Mariano et al., 2003). Theoretical support for the use of free-slip conditions has been provided, showing better agreement with classical turbulence theory compared to the no-slip condition (Deremble et al., 2011). However, it is clear that lateral viscous conditions do not fully capture all the unresolved physics of the turbulent boundary layer.

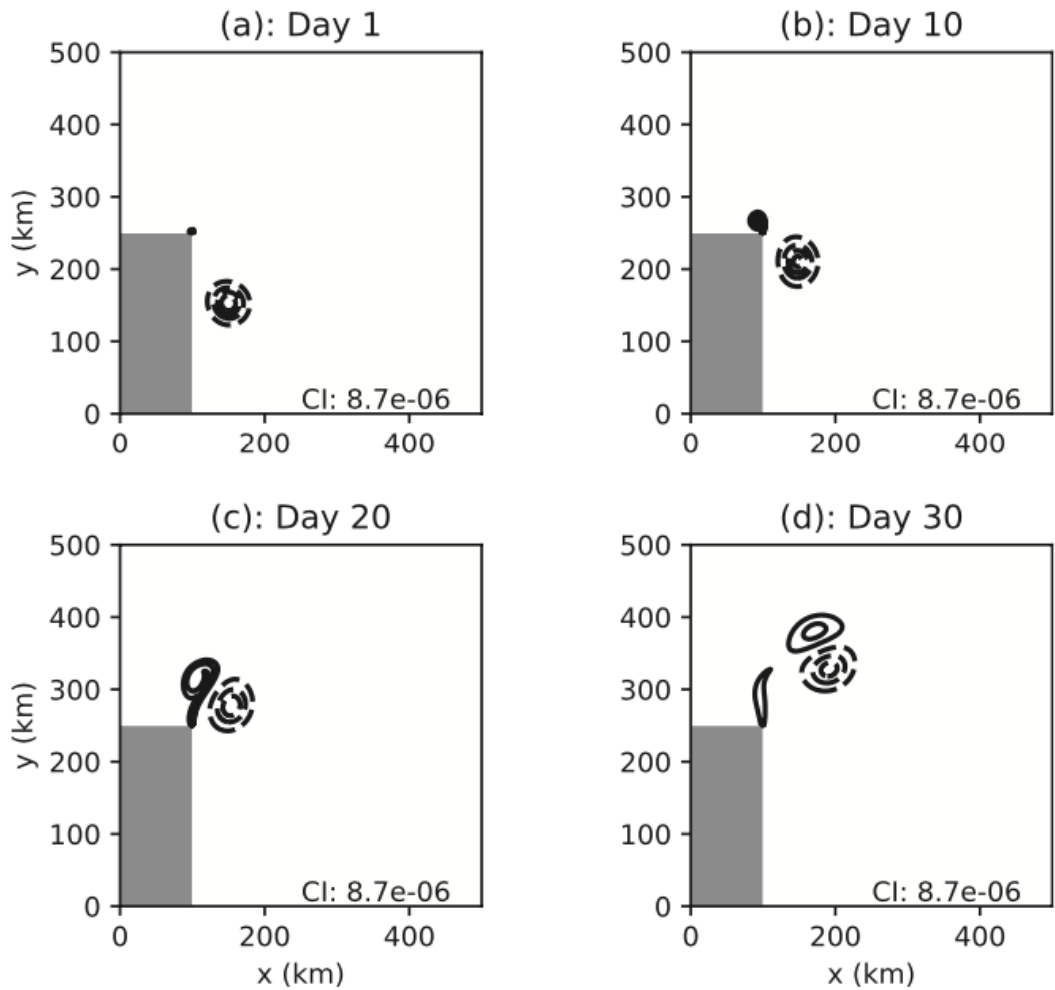


Figure 3: From (Deremble et al., 2016) (their figure 3). Time evolution of the vorticity field at (a) 1, (b) 10, (c) 20, and (d) 30 days. Dashed contours are negative values, and solid contours are positive values. Contour interval is $8.7 \cdot 10^{-6} \text{ s}^{-1}$. The x- and y-axes are in kilometers.

For instance, Deremble et al. (2016) demonstrate that the interaction between an eddy and a sharp topographic feature, such as an isolated step, induces a retroflection of the current at the tip (Deremble et al., 2016). Sharp turns in the coastline can result in retroflection of boundary currents and eddy generation (Magaldi et al., 2008; Warner & MacCready, 2009). Numerical studies aimed to reproduce this process (Figure 3), but the simulated response is highly sensi-

tive to the formulation of discrete advection or diffusion and the nature of the viscous condition applied at the tip (Dengg, 1993; Deremble et al., 2016; Dupont & Straub, 2004). Dengg (1993) argues that the retroflection of the current at a cape is better captured in numerical simulations when a no-slip viscous condition is used instead of a free-slip condition. Therefore, it remains unclear whether a slippery viscous boundary condition is appropriate to represent retroflection at a sharp turn in the coastline.

Apparent roughness exerted by staircase-like coastlines

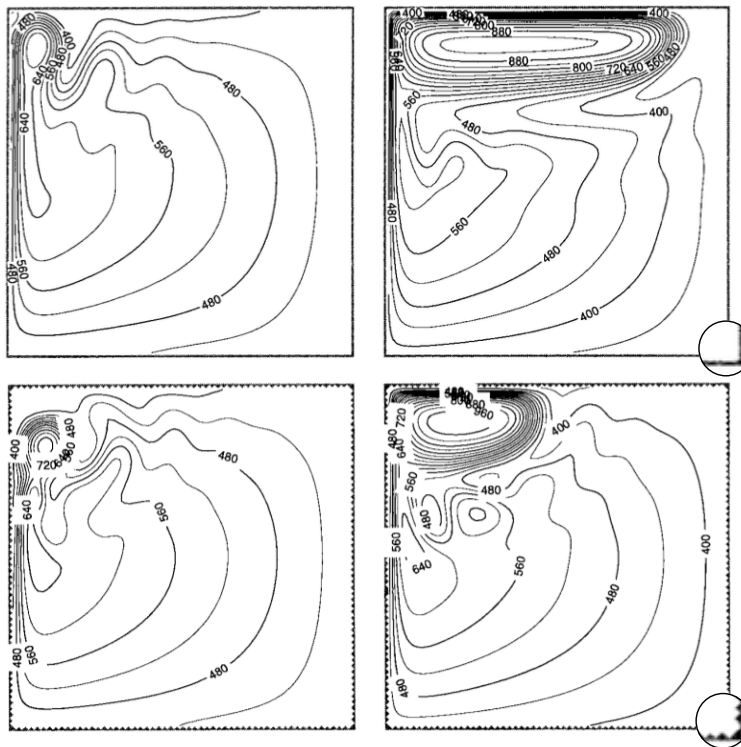


Figure 4: From Adcroft and Marshall (1998) (adaption of their figure 3 and figure 8e,f). Steady solutions solved with a no-slip (left column) and a free-slip (right column) viscous boundary condition, under the rot-div stress tensor. Isolines depict the active layer thickness h of the reduced gravity model. In the upper column, the mesh is aligned with the borders of the basin. In the bottom row, the mesh is turned at 45° relative to the borders, as illustrated in the bottom-right zooms. Notably, both no-slip and free-slip solutions contract under the presence of staircase coastlines.

Irrespective of the chosen boundary condition, boundary currents in OGCMs are affected by the staircase-like nature of the lateral boundary. Adcroft and Marshall (1998) (hereafter AM98) conducted experiments using an idealised square basin configuration and different orientations of the numerical mesh. They found that the broken aspect of the shoreline consistently causes a 'spurious form drag' that slows down the coastal flow, even when a free-slip boundary condition is applied at the coast (Figure 4). Subsequent investigations within similar configurations suggested that the spurious drag may persist at higher resolution because coastal steps in-

crease in number as they become smaller (Adcroft & Marshall, 1998; Dupont et al., 2003). These results conflict with the expectation that undesirable effects of artificial indentation of model coastlines should vanish with resolution high enough to well approximate the target shoreline.

This 'staircase problem' is troublesome for more realistic geometries as artificial steps are unavoidable in OGCMs, since isobaths are generally misaligned with the grid. Artificial steps along isobaths can affect boundary currents but also any horizontal current following f/H contours (f is the Coriolis frequency and H the seafloor depth), ultimately affecting the basin-scale three-dimensional circulation (Edwards & Pedlosky, 1998). Hence, artificial steps appear to exert a lateral 'spurious form drag' despite using free-slip conditions or reducing the size of the steps.

Spurious mixing within downslope currents

Artificial steps in the topography can also induce strong vertical velocities and spurious convective mixing, particularly when bottom currents descend along staircase-like slopes. As a result, there is often an overestimation of mixing in water mass properties during overflows, as highlighted by numerous past studies (Legg et al., 2009; Riemenschneider & Legg, 2007; Ilıcak et al., 2012). This overestimation generally leads to deep water that is excessively warm and fresh (Winton et al., 1998) or bottom water that is overly warm and salty (Downes et al., 2011). Such discrepancies between simulated and actual hydrographic properties impact the realism of the model and carries important consequences for the large-scale circulation (Dickson et al., 2008; H. Wang et al., 2015). Consequently, inaccuracies in the numerical models used to simulate these overflows can lead to important consequences for climate predictions. Legg et al. (2009) emphasize that models lacking precise representation of overflows may incorrectly locate deep-water formation sites (Kösters et al., 2005), and inaccurately depict the vertical structure of the Meridional Overturning Circulation (MOC) and meridional heat transport. As another example, modelling of the ice shelf-ocean interface with a z -coordinate system shares some similar difficulties: excessive diapycnal mixing of the light plume occurs around boundary steps (Losch, 2008).

However, numerous studies focusing on idealised and realistic overflows have consistently concluded that a significant reduction in excessive mixing can be achieved by substantially increasing the spatial resolution. While most of these studies recommend prioritising refinement in the horizontal direction (Legg et al., 2006; Riemenschneider & Legg, 2007; Legg et al., 2008; Q. Wang et al., 2008; Colombo et al., 2020), some have also shown that refining the vertical resolution or both resolutions (Reckinger et al., 2015; Laanaia et al., 2010) can also have a positive impact on mitigating spurious mixing. However, Winton et al. (1998) suggest that the optimal resolution of the topography is achieved when the discrete aspect ratio corresponds to the ac-

tual slope. Naturally, increasing resolution may not always be feasible nor desirable in realistic OGCM configurations. Finding suitable ways to reduce spurious mixing in climate models is crucial.

Thus, although the spurious mixing created by topographic steps along downslope currents tends to decrease as the steps become smaller, the staircase problem persists. Considering the diverse behaviours exhibited by staircase-like topographies, it is important to better understand the physical impact of an isolated step or a collection of steps along a boundary.

Spurious effects of partial bottom cells

The presence of steps in the model topography leads to discontinuities in the depth profile, which introduce noise at the scale of the grid and distort the mean circulation ([Pacanowski & Gnanadesikan, 1998](#); [Adcroft et al., 1997](#)). [Adcroft et al. \(1997\)](#) show that increasing spatial resolution can reduce the noise in simulated currents by minimising the jumps in the stepped profile. However, achieving the recommended resolution that matches the aspect ratio of the stepped topography to the actual slope is not always feasible in OGCMs.

To better represent the actual topography in z -coordinate, [Adcroft et al. \(1997\)](#) introduced the 'partial cells' method, where the bottom surface of the deepest wet cells is modified to align with the actual seafloor depth (Figure 2, left). This approach departs from the historical 'full cells' technique ([Bryan & Cox, 1967](#)), which simply masks cells below the target bathymetry. The truncation of the bottom cells in the 'partial cells' method enables a more accurate and computationally efficient representation of the actual slope compared to the 'full cells' method, leading to improved simulated currents ([Pacanowski & Gnanadesikan, 1998](#); [Adcroft et al., 1997](#)). Though partial cells do allow a more faithful representation of topography, they cannot eliminate most issues of stepped topography and generate additional spurious effects.

The partial cell approach generates a misalignment of the cell centers at the boundary, and thereby introduces interpolation errors in the computation of the horizontal pressure gradient. These errors alter the solution from the beginning of the simulation and can induce significant flow in the bottom cells that propagates throughout the water column ([Gallus & Klemp, 2000](#); [Pacanowski & Gnanadesikan, 1998](#); [Adcroft et al., 1997](#)). These errors persist even when increasing spatial resolution but can be significantly reduced by assuming a linear equation of state for seawater ([Pacanowski & Gnanadesikan, 1998](#)). However, such an assumption is not applicable in climate models where non-linearities in the equation of state play a crucial role in setting global ocean stratification ([Roquet, 2013](#)). Likewise, this aspect is also problematic when modelling under ice shelf seas, where non-linearities affect the ascending cold plumes along the shelf ([Losch, 2008](#)).

Hence, stepped topographies have significant implications for the general circulation of the ocean. Although increasing spatial resolution can address some of the adverse effects of stepped topographies, the associated computational cost (with its monetary and carbon footprint implications) is often deterrent. In this context, we formulate the overarching question: **Are there computationally efficient ways to reduce the adverse effects of stepped topographies in OGCMs?**

2 State of the art

Alternative traditional approaches

There are a number of recent attempts to overcome the problems of staircase topography in geopotential coordinate models. In order to examine the impact of a stepped representation of topography on boundary currents, we will discuss various approaches to represent topography in circulation models. Specifically, we will compare the 'partial cells' approach (Adcroft et al., 1997) commonly used in z -coordinate models with the 'shaved cells' technique (Adcroft et al., 1997) and the s coordinate or terrain-following approach (Bleck & Smith, 1990; Haidvogel et al., 1992).

The major drawback of stepped topographies lies in the artificial discontinuities introduced along both the horizontal and vertical directions, which alter the representation of bottom currents. An alternative approach, known as the 'shaved cells' method (Adcroft et al., 1997), addresses this issue by trimming the bottom wet cells that intersect the slope, resulting in a piecewise linear representation of the slopes. This refinement slightly reduces but does not eliminate the spurious mixing during overflow events (Q. Wang et al., 2008), while significantly reducing noise in the computed fields (Pacanowski & Gnanadesikan, 1998; Adcroft et al., 1997). This effect can be attributed to the continuous depth variation across horizontal levels and smoother bottom currents (left and middle panels in Figure 5). In contrast, the s -coordinate representation, or terrain-following representation, achieves a continuous representation of the seafloor by applying a vertical coordinate transformation. This transformation results in bottom currents that exhibit minimal fluctuations at the grid scale (right panel in Figure 5). The resultant smooth representation of topography induces a smoother velocity field, which helps reducing spurious mixing at the bottom.

However, these advantages come at a cost. The use of the 'shaved cells' method in OGCMs is often impractical due to the severe constraint it imposes on the time step. The trimming of bottom cells creates a situation where a cell with a small volume has a large exchange face, which jeopardises the numerical stability of the model (Adcroft et al., 1997). On the other hand, terrain-following coordinates are often disregarded for climate applications due to the

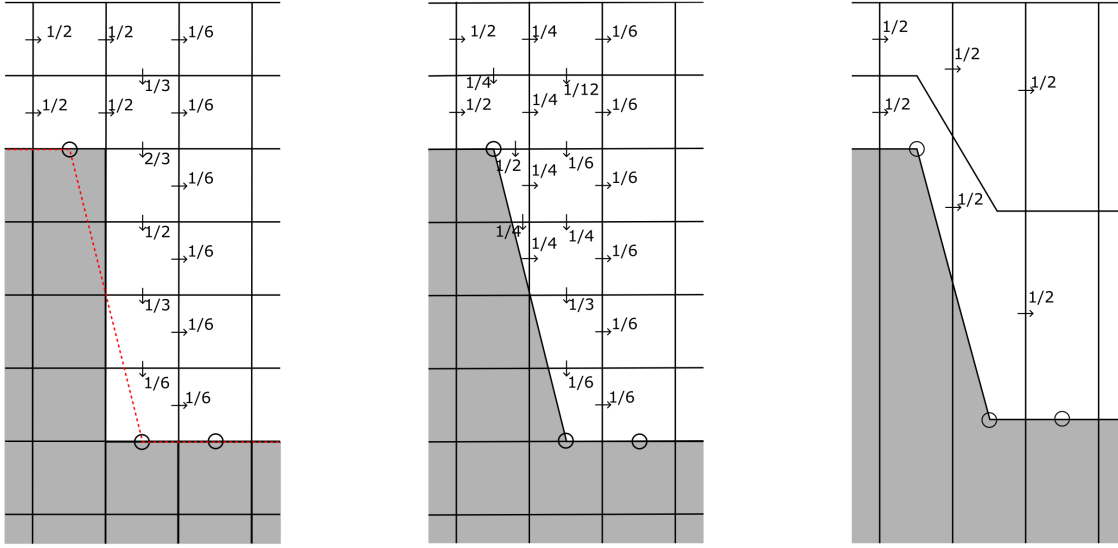


Figure 5: Idealisation of a barotropic flow across a slope (inspired from [Adcroft et al. \(1997\)](#)). The total transport of the column is unity and assumed to be uniformly distributed across the vertical levels with a vertical and horizontal grid spacing of unity. The land is masked in grey and the Cartesian grid is in solid black lines. The real slope (red dotted line connecting the black circles) is defined at T-cells and its discretisation is shown in z -coordinate with full cells (or equivalently partial cells) at the left and shaved cells at the middle. The right subplot shows the slope represented with a two-level s -coordinate system.

misalignment of tilted levels with geopotential surfaces which leads to significant errors in the calculation of the horizontal pressure gradient (HPG) throughout the ocean interior, resulting in non-physical residual currents ([Lemarié et al., 2012](#)). The 'shaved cell' representation also suffers from this limitation but only in its bottom levels.

It is commonly recommended that the bottom slope seen by an s -coordinate model does not exceed a certain factor r , typically around 0.2. r is a proxy for the magnitude of HPG errors; it is defined as $\Delta H / \bar{H}$, where ΔH and \bar{H} represent the local grid-scale difference and average seafloor depth, respectively. The usual strategy is to limit the maximum slope handled by the coordinate at a given resolution, by smoothing and coarsening the original bathymetry as needed to maintain r sufficiently small. However, this procedure significantly restricts the use of a generalized s -coordinate in realistic OGCMs, particularly in regions where solving currents interacting with steep topographic slopes is crucial, such as in the western boundary current separation problem ([Schoonover et al., 2016](#)). To address this issue, some OGCMs, like the GFDL model ([Adcroft et al., 2019](#)), uses a 'z-on-top-of-s' coordinate ([Madec & Imbard, 1996](#)) to minimise HPG errors while still representing the bathymetry using a terrain-following approach. However, the presence of large steps concurs with that of steep slopes, so that this approach remains imperfect. Are there ways to retrieve the benefits of shaved cells or terrain-following approaches without the above-mentioned drawbacks?

Insights on the lateral viscous boundary conditions

Previous studies have pointed out the drawbacks of a poor approximation of the boundary condition on the simulated currents. [Verron and Blayo \(1996\)](#) highlight the negative impact of a crude implementation of the viscous boundary condition at the boundary. Likewise, [Kazantsev \(2015\)](#) shows in a configuration similar to AM98 that optimised boundary conditions with a 4D-Var data assimilation technique compensate the errors induced by the staircase-like approximation of the coastline. However, their findings are restricted to this idealised configuration and cannot be generalised to all OGCMs.

Similarly, several studies have observed a deceleration of Kelvin waves propagating along a staircase-like 'straight' coastline ([Pedersen, 1986](#); [Schwab & Beletsky, 1998](#); [Greenberg et al., 2007](#)). [Griffiths \(2013\)](#) argued that the retardation effects of an indented coastline could be handled by implementing the right impermeability condition corresponding to the real coastline. However their findings apply only to traveling Kelvin waves, and it remains unclear how the long-standing issue of spurious form drag should be addressed in OGCMs.

Improving the resolution of boundary currents

The potential of improving discrete advection schemes to mitigate the spurious effects of staircase coastlines has been explored. [Cox \(1979\)](#) initially discussed this issue while studying the Somali current, noting a slight weakening of the alongshore flow when the mesh was rotated at a 45° angle from the straight shoreline. This difference was attributed to truncation errors in the advection schemes. Several investigations in similar configurations as AM98 showed that the response of the flow to staircase-like coastlines depends on the advection and diffusion schemes ([Dupont et al., 2003](#)). Notably in ([Barnier et al., 2006](#); [Le Sommer et al., 2009](#)), advection schemes like the energy-enstrophy conserving (EEN) scheme ([Burridge & Haseler, 1977](#)) with partial steps have shown promise in enhancing topostrophy and reducing solution noise at the bottom compared to the simpler enstrophy conserving (ENS) scheme ([Sadourny, 1975](#)).

Increasing the spatial resolution has been suggested as a means to resolve geostrophic eddies and the bottom Ekman layer more effectively ([Reckinger et al., 2015](#); [Colombo et al., 2020](#)). However, excessive mixing is observed even in a simple 2D vertical-horizontal plane where eddies and Coriolis effects are absent ([Ilıcak et al., 2012](#)), highlighting the interplay of bottom currents with artificial steps. Determining the optimal resolution is challenging, as viscosity is often reduced proportionately with the increase in resolution to capture finer scales during overflows. Studies have demonstrated that increased lateral viscosity can lead to a reduction in numerical mixing ([Riemenschneider & Legg, 2007](#); [Legg et al., 2008](#); [Ilıcak et al., 2012](#)). In fact, it

is widely recognised that smoother currents at the grid scale result in less mixing in the advective tracer field. Can a careful choice of the advection formulation in OGCMs reduce adverse effects of topographic steps?

Other issues arise with the downslope flow of dense waters, which tend to be diluted too fast into the ambient environment. This dilution phenomenon is particularly prominent in coarse resolution models with horizontal resolutions on the order of 10-100 km, where water masses can enter cells that are too wide to effectively conserve their properties, and where large steps can favour deep convective mixing of overflowing waters (Campin & Goosse, 1999). In fact, this dilution problem can be mitigated by reducing the size of the cells, as smaller cells and steps are better able to preserve the density characteristics of the water masses, thereby reducing the overall dilution of dense waters.

Various bottom boundary layer schemes have been developed to reduce spurious mixing in z -coordinate models as dense plumes descend the slope (Campin & Goosse, 1999; Beckmann & Döscher, 1997; Killworth & Edwards, 1999; S. M. Griffies et al., 2000). These parameterisation methods have proven useful not only to palliate the side effects of stepped topographies but also for representing non-hydrostatic phenomena occurring during overflows (Legg et al., 2006; N. Z. a. S. Griffies, 2012; Snow et al., 2015). However, the wide range of available parameterisations and their application dependencies make it difficult to determine the most suitable approach (Snow et al., 2015). The limited testing and comparison of overflow parameterisations within realistic bathymetry models underscore the need for a deeper understanding of the source of spurious mixing of stepped topographies.

The deficiencies in the representation of overflows are thought to stem from the stepped representation of bottom topography in z -coordinate models, which induces artificial mixing when a gravity current overflows a step (Winton et al., 1998). One approach to address this issue is to reduce the size of the mesh, resulting in smaller steps and jumps (Colombo et al., 2020). The use of the 'shaved cells' approach instead of the traditional 'partial cells' method allows for a piecewise linear representation of the slope, similarly to a terrain-following coordinate. However, studies have shown that the shaved cells representation can mitigate, but not completely eliminate, the spurious mixing (Q. Wang et al., 2008). This suggests that other factors, in addition to the presence of topographic steps, play a role spurious mixing within overflows. What are these factors?

Practical solutions are currently lacking to improve the representation of topography in z -coordinate OGCMs. As a result, we are interested in exploring a new approach for representing topography, namely the Brinkman volume penalisation method.

Toward a new approach: the Brinkman volume penalisation method

The Brinkman volume penalisation (BVP) technique is a powerful method that enables the simulation of the blocking and viscous effects of a solid body on fluid flow. One of its unique features is the replacement of the solid domain with a permeable porous medium. The motion in the porous region is governed by the Brinkman equation where some permeability (which involves friction) is included to account for the resistance of the porous medium to fluid through-flow. [Caltagirone \(1994\)](#) shows in the case of very weakly permeable (highly frictional) medium that the drag and lift exerted by the porous body is the same as if it were solid. In addition, the complete incompressible Navier-Stokes/Brinkman equations have been shown to be well posed ([Angot, 1999](#); [Angot et al., 1999](#)). Recently, [Debreu et al. \(2020, 2022\)](#) showed the potential of the method to represent topography in ocean models by combining the BVP to an s coordinate, which allows to capture the steep topographic slopes that would otherwise violate the r factor requirement. Furthermore, [Kevlahan et al. \(2015\)](#) reproduced a similar basin configuration as AM98 on a hexagonal-triangular C grid and showed that their Brinkman penalisation method was not sensitive to the orientation of solid boundaries with respect to the physical shoreline, thereby showing the potential of the BVP method to address the lateral staircase problem in ocean circulation models.

The BVP method shares some similarities with immersed-boundary methods (IMB) in the treatment of the forcing term (e.g., permeability) in the equations ([Mittal & Iaccarino, 2005](#)). The treatment resembles the 'Direct Forcing' technique, which enforces zero velocities in the penalised region (to enforce no-slip conditions). Additionally, [Bensiali, Chiavassa, and Lian-drat \(2015\)](#) demonstrate the versatility of the penalisation method by showing that the BVP can handle Robin boundary conditions (partial slip) in addition to the traditional Dirichlet (no-slip) and Neumann (free-slip) conditions. However, the introduction of the penalty parameter called porosity sets the BVP method apart from other IMB methods, allowing for finer control of the effective volume of the water column ([Mittal & Iaccarino, 2005](#); [Lundquist et al., 2010](#)).

Furthermore, one possibility of the BVP method is the spreading of the penalised region, whose benefit is often overlooked in previous studies ([Debreu et al., 2022, 2020](#); [Kevlahan et al., 2015](#); [Reckinger et al., 2012](#)). Spreading the interface is often justified to preserve the numerical stability of the method ([Kevlahan et al., 2015](#); [Reckinger et al., 2012](#)) but also encouraged as it dampens the impacts of topographic steps ([Debreu et al., 2022](#)). The numerical stability of the BVP method will be addressed in this thesis.

In the traditional approach, the no-flow condition of the topography is typically enforced on the cells adjacent to the boundary. However, the BVP method takes a different approach by incorporating the blocking effect of the topography within a few cells near the land borders, using both penalty parameters (i.e. porosity and permeability). This spread interface allows for

a more distributed topographic constraint on the bottom currents, extending throughout the penalised region. This could allow to better resolve bottom currents with discrete schemes, and yield reductions in spurious mixing. This anticipation is a primary motivation for developing the BVP method in this thesis.

Key questions

These recent results call for clarification of the response of bottom currents to stepped topography in OGCMs. Is there a way to elucidate the physical impact of an isolated step or a collection of steps along a coastline? Can we leverage the advantages of the BVP method to mitigate adverse effects of stepped topographies? These and earlier questions may be summarised as follows:

- **Are there computationally efficient ways to reduce adverse effects of stepped topographies in OGCMs?**
- **Can Brinkman Volume Penalisation reduce the sensitivity of circulation to topographic steps?**
- **Is Brinkman Volume Penalisation a viable option in climate-scale ocean models?**

The following chapter revisits the well-known staircase problem originally presented by [Adcroft and Marshall \(1998\)](#) and the isolated step configuration of [Deremble et al. \(2016\)](#) to unveil numerical promises and pitfalls of lateral boundary representations. Chapter II focuses on deriving the numerical stability of the Brinkman volume penalisation method and assessing the impact of the penalty parameters on stability. Subsequently, we investigate in Chapter III the potential advantages of spreading the penalised interface within an idealised overflow test case inspired by [Ilıcak et al. \(2012\)](#). In Chapter IV, we explore some uses of the BVP method in realistic configurations. We discuss the implications arising from a preliminary simulation using a penalised ORCA1 configuration ([Madec & NEMO System Team, 2022](#)). Finally, we provide a summary of the key findings and offer perspectives for future research (Chapter V).

Addressing the Lateral Form Drag of Piecewise Constant Coastlines

Preamble

Using an idealised square basin configuration and various orientations of the numerical mesh, [Adcroft and Marshall \(1998\)](#) (hereafter AM98) showed that artificial indentation of a shoreline consistently causes a spurious form drag that slows down coastal currents, despite using a free-slip condition. Several studies addressed this question by investigating the sensitivity to other numerical formulations ([Adcroft & Marshall, 1998](#); [Dupont et al., 2003](#); [Dupont & Straub, 2004](#); [Greenberg et al., 2007](#)), which consistently showed a slowdown of currents depending on the number of steps. However, these studies also indicated that the staircase issue may persist even at higher resolutions, because coastal steps increase in number as they become smaller ([Adcroft & Marshall, 1998](#); [Dupont et al., 2003](#)). It remains unclear how the long-standing issue of spurious form drag should be addressed in OGCMs.

Realistic representation of boundary currents along a staircase-like coastline is challenging because coastal steps may have spurious as well as real effects on the flow. We know the expected effect of an isolated step: when a current passes near a step, filaments of opposite vorticity are generated at the tip, inducing a current retroflexion ([Deremble et al., 2016](#)). Hence, it remains unclear whether grid-scale indentation of the boundary contributes to realistic dissipation and retroflexion of boundary currents, resulting in an apparent roughness of the topographic contour, or whether it should really mimic a smooth boundary.

Following the work of [Kevlahan et al. \(2015\)](#), our initial intention was to apply the Brinkman Volume Penalisation method to address the 'staircase problem' in Cartesian grids. The concept seemed promising, as it involved controlling the roughness of the coastline by adjusting the permeability parameter of the porous medium and thereby regulating the 'form drag' exerted on the flow. However, we find that when smoothing the coastline using penalisation, a steering effect similar to an actual topographic slope is introduced, altering the nature of the problem (see Chapter IV). Consequently, it appears that using penalisation to address the 'staircase problem' is not an appropriate solution.

One strategy could be to avoid the generation of artificial indentations along the shoreline by implementing lateral shaved cells ([Adcroft et al., 1997](#)). For a mesh oriented at 45° , a straight coastline coincides with the F nodes of the C-grid, and the volume of the intersecting cells should be precisely halved. This representation is made possible with the Brinkman Volume Penalisation method by making half cells porous. In this case, porosity impacts only the volume of the cell while the face porosity at the velocity nodes U and V are unchanged, thereby avoiding the generation of topographic waves, as shown in Chapter IV. Considering half cells requires dividing the reference time step by a factor of two and leads to modification of the kinetic energy gradient for consistency with the continuity equation, as explained by [Marchand \(2014\)](#). However, simulated solutions on a 45° turned mesh are not modified with this treatment of the coastline (not shown), echoing the study of [Marchand \(2014\)](#). These exploratory results gradually led us to confront the subtleties associated with the 'staircase problem', which ultimately led to the publication of the subsequent paper.



RESEARCH ARTICLE

10.1029/2022MS003594

Key Points:

- The impact of coastal indentation on circulation within an idealized square basin is studied systematically for various numerical choices
- Solutions are insensitive to coastal indentation with rot-div formulation of the diffusive tensor and sufficiently fine spatial resolution
- Indented coastlines become slippery when a true mirror boundary condition is imposed on the flow for all numerical formulations

Correspondence to:

A.-A. Nasser,
antoine-alexis.nasser@inria.fr

Citation:

Nasser, A.-A., Madec, G., de Lavergne, C., Debreu, L., Lemarié, F., & Blayo, E. (2023). Sliding or stumbling on the staircase: Numerics of ocean circulation along piecewise-constant coastlines. *Journal of Advances in Modeling Earth Systems*, 15, e2022MS003594. <https://doi.org/10.1029/2022MS003594>

Received 24 DEC 2022
Accepted 15 APR 2023

Sliding or Stumbling on the Staircase: Numerics of Ocean Circulation Along Piecewise-Constant Coastlines

Antoine-Alexis Nasser^{1,2} , Gurvan Madec^{1,2} , Casimir de Lavergne² , Laurent Debreu¹, Florian Lemarié¹ , and Eric Blayo¹

¹Univ. Grenoble Alpes, Inria, CNRS, Grenoble INP, LJK, Grenoble, France, ²LOCEAN Laboratory, Sorbonne University-CNRS-IRD-MHNM, Paris, France

Abstract Coastlines in most ocean general circulation models are piecewise constant. Accurate representation of boundary currents along staircase-like coastlines is a long-standing issue in ocean modeling. Pioneering work by Adcroft and Marshall (1998, <https://doi.org/10.3402/tellusa.v50i1.14514>) revealed that artificial indentation of model coastlines, obtained by rotating the numerical mesh within an idealized square basin, generates a *spurious form drag* that slows down the circulation. Here, we revisit this problem and show how this spurious drag may be eliminated. First, we find that *physical* convergence to spatial resolution (i.e., the main characteristics of the flow are insensitive to the increase of the mesh resolution) allows simulations to become independent of the mesh orientation. An advection scheme with a wider stencil also reduces sensitivity to mesh orientation from coarser resolution. Second, we show that indented coastlines behave as straight and slippery shores when a true mirror boundary condition on the flow is imposed. This finding applies to both symmetric and rotational-divergence formulations of the stress tensor, and to both flux and vector-invariant forms of the equations. Finally, we demonstrate that the detachment of a vortex flowing past an outgoing corner of the coastline is missed with a free-slip (zero vorticity) condition at the corner. These results provide guidance for a better numerical treatment of coastlines (and isobaths) in ocean general circulation models.

Plain Language Summary Most ocean general circulation models represent coastlines as piecewise constant, which does not accurately reflect the true boundary. This approximation is necessitated by the size and square shape of model grid cells, together with finite computational resources, making it difficult to finely represent the boundary. A long-standing issue in ocean modeling is accurately representing boundary currents along these staircase-like coastlines. In particular, Adcroft and Marshall (1998, <https://doi.org/10.3402/tellusa.v50i1.14514>) discovered that artificial indentation of the model coastlines generates a “spurious form drag” that slows down the circulation. Our study revisits this long-standing issue and shows how this spurious drag may be eliminated. First, we demonstrate that having a sufficiently fine spatial resolution to resolve the physical processes allows the model to be insensitive to coastal indentation. We also show that indented coastlines become slippery, as if they were smooth and straight shores, when a true mirror boundary condition on the flow is imposed. Finally, we show how to faithfully simulate the retroflexion of a current past a cape. In summary, these results provide guidance for a better numerical representation of marine land-forms in numerical ocean models.

1. Introduction

Drawing the separation between land and ocean grid cells is a pre-requisite to building any ocean model configuration. This task requires non-trivial coarse-graining of the target (observed or idealized) bathymetry. Consider the example of the coastline in an ocean general circulation model (OGCM) with a structured numerical mesh (Figure 1). The real coastline typically needs to be approximated by a piecewise constant boundary. This approximation involves the removal of sub-grid-scale features of the real coast, the sharpening of real bends into corners, and the creation of artificial steps due to misalignment between the real coastline and the numerical mesh (Figure 1). This transformation of the real coastline carries important consequences for the simulated boundary currents, and therefore for the simulated large-scale circulation (Ezer, 2016). These consequences depend not only on the design of the model coastline, but also on other numerical choices such as lateral boundary conditions (Adcroft & Marshall, 1998; Dengg, 1993; Shchepetkin & O'Brien, 1996). Little guidance currently exists to make the most appropriate numerical choices for the chosen application, and it is often unclear to what extent the model boundary behaves as the originally intended coastline or isobath.

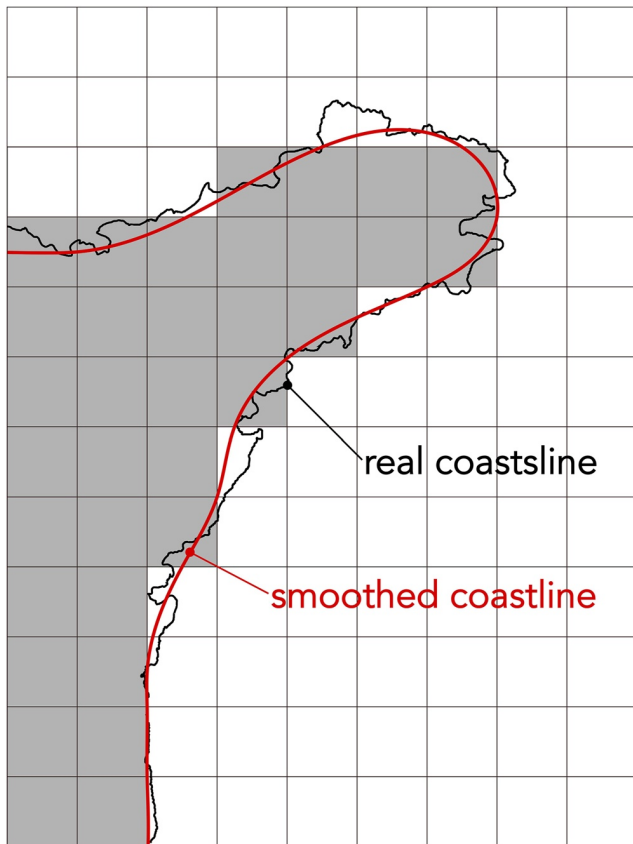


Figure 1. Schematic illustrating the coarse-graining of a coastline on a structured mesh. The real coastline (thin brown line) presents an infinite number of details that are too small, relative to the size of grid cells (thin black), to be represented by the numerical model. It must be averaged over at least two grid points to avoid noise generation, resulting in a smooth coastline (red curve). Then the land mask (gray cells) is defined from the projection of the smooth coastline onto the grid, creating artificial abrupt changes in coastline direction.

The choice of lateral boundary condition remains a thorny issue in this regard. It is clear that the “no-slip” condition is the physically founded condition when representing interactions of a fluid with solid boundaries (Richardson, 1973). However it is far from obvious how this fundamental constraint should be translated in OGCMs (Deremble et al., 2011), whose typical spatial resolution (order 10–100 km in the horizontal) does not permit to resolve the viscous boundary layer. In fact, the small aspect ratio of the ocean implies that the viscous boundary layer sees a gently sloping seafloor rather than vertical sidewalls, suggesting that the lateral boundary condition is a numerical requirement lacking physical underpinning. For example, in z-coordinate OGCMs, the sloping seafloor is numerically transformed into a staircase boundary that alternates flat bottom and vertical walls. In this case, combined use of a bottom drag and a no-slip condition at the side-wall may potentially overestimate the frictional boundary effects. In practice, slippery or mixed lateral boundary conditions, such as “free-slip” or “partial slip,” are often preferred in coarse OGCMs (Penduff et al., 2007). Deremble et al. (2011) provide some theoretical support for this approach by showing that a free-slip condition yields better agreement with classical turbulence theory than does a no-slip condition. However, they also caution that lateral viscous conditions do not capture all the unresolved physics of the turbulent boundary layer. In general it is not known how to best define boundary conditions along the staircase-like frontiers of OGCMs.

The problem of defining suitable boundary conditions is made even more complex by the (unintended) impacts on the simulated circulation of artificial steps in the lateral boundary. Using an idealized square basin configuration and various orientations of the numerical mesh, Adcroft and Marshall (1998) (hereafter AM98) first pointed out that artificial indentation of a shoreline systematically causes a *spurious form drag* that slows down the coastal flow. AM98 showed that this drag depends on the numerical formulation of diffusive stresses but always exists, including when a “free slip” boundary condition is implemented. Subsequent investigations within similar configurations showed that the response of the flow to staircase-like coastlines depends on the advection and diffusion schemes (Dupont et al., 2003). These studies also suggested that the spurious drag may persist at higher resolution because coastal steps increase in number as they become smaller (Adcroft & Marshall, 1998; Dupont et al., 2003). Griffiths (2013) argued that the adverse

effects of an indented coastline could be handled by implementing the right impermeability condition corresponding to the real coastline. However their findings apply only to traveling Kelvin waves, and it remains unclear how the long-standing issue of spurious form drag should be addressed in OGCMs.

The response to an isolated, large-scale bend in the coastline also deserves attention because real swerves of the shoreline can have pronounced impacts on boundary currents (Magaldi et al., 2008; Warner & MacCready, 2009), and because such swerves may be sharpened in their discrete model representation. Deremble et al. (2016) showed that an outgoing corner in the coastline induces retroflexion of a coastal stream. Their findings echo those of Dupont and Straub (2004), who varied the curvature of a wavy wall configuration and found that opposite vorticity filaments were created at the coastal tips and caused detachment of the flow. In both studies, only some numerical formulations enable to capture the expected physical behavior. The reasons for this strong sensitivity to numerical formulations are not fully elucidated.

Here, we address these questions using idealized model configurations. We first reproduce the configuration of AM98 (Section 2) and demonstrate that the circulation is insensitive to the mesh orientation—and related coastline indentation—provided that the model is *physically* converged to spatial resolution (Section 3). Next, we expose how a *true* mirror boundary condition on the flow renders the indented coastline as slippery as a straight, free-slip frontier (Section 4). The numerical representation of an isolated, large-scale step in the coastline is

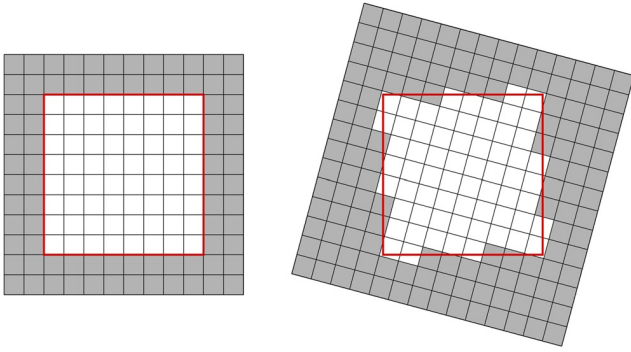


Figure 2. Effects of rotating the numerical mesh within an idealized square basin. The mesh is represented by the black lines. Land is shaded in gray, the oceanic domain in white. The red thick line represents the physical coastline. On the left, the grid is aligned with the basin. On the right, the mesh is rotated so that artificial steps appear in the model shoreline. This figure is adapted from AM98.

investigated in Section 5 using the configuration of Deremble et al. (2016). We summarize our findings and recommendations in Section 6.

2. Methods

2.1. Configuration

We consider the same problem as AM98: a shallow water model with reduced gravity is solved in a square basin of size $L = 2,000$ km. An anticyclonic wind stress $\boldsymbol{\tau} = (-\tau_0 \cos(\pi y/L), 0)$ is forcing the active layer. The coordinate system (x, y) has its origin in the lower left corner of the square basin. Equations in vector invariant form read

$$\partial_t h + \text{div}(\mathbf{h}\mathbf{u}) = 0 \quad (1)$$

$$\partial_t \mathbf{u} + \left(\frac{f + \zeta}{h} \right) \mathbf{k} \times \mathbf{h}\mathbf{u} + \nabla \cdot \frac{1}{2} (\mathbf{u}\mathbf{u}) = -g' \nabla h - r\mathbf{u} + \mathbf{D}_\nu + \frac{\boldsymbol{\tau}}{\rho_0 h}, \quad (2)$$

where h is the active layer thickness, $\mathbf{u} = (u, v)$ represents the horizontal velocity vector, $\zeta = \mathbf{k} \cdot (\nabla \times \mathbf{u})$ the relative vorticity, \mathbf{k} the vertical unit vector, f the Coriolis parameter, g' the reduced gravity, r the friction coefficient, \mathbf{D}_ν the diffusion term and ρ_0 the density.

Two formulations of the diffusion term (\mathbf{D}_ν where ν is the lateral viscosity) are considered, that will lead to different discretisations: the rotational-divergence (hereafter called “rot-div”) form (Madec et al., 1991) and the symmetric form (Griffies & Hallberg, 2000). The rot-div form is calculated as $\nabla(\nu \chi) - \frac{1}{h} \nabla \times (\nu h \zeta)$ where transport divergence χ is defined as $\chi = \frac{1}{h} (\partial_x(hu) + \partial_y(hv))$. The symmetric form is expressed instead as $\frac{1}{h} \nabla \cdot (\nu h \boldsymbol{\sigma}_{sym})$ (Gent, 1993) where

$$\boldsymbol{\sigma}_{sym} = \begin{pmatrix} D_T & D_S \\ D_S & -D_T \end{pmatrix}, \quad \begin{aligned} D_T &= \partial_x u - \partial_y v, \\ D_S &= \partial_x v + \partial_y u. \end{aligned} \quad (3)$$

A viscous boundary condition (see Section 2.3) is applied at the wall of the basin by enforcing the values of χ and ζ in the “rot-div” form and D_S and D_T in the symmetric form. In the discrete form, the same viscous boundary condition can thus be written differently depending on the formulation of \mathbf{D}_ν .

We will also perform simulations using the flux form of the shallow water equations. In this case, Equation 2 rewrites as

$$\partial_t(\mathbf{h}\mathbf{u}) + \nabla \cdot (\mathbf{h}\mathbf{u} \otimes \mathbf{u}) + f(\mathbf{k} \times \mathbf{h}\mathbf{u}) = -g' h \nabla h - r\mathbf{h}\mathbf{u} + h\mathbf{D}_\nu + \frac{\boldsymbol{\tau}}{\rho_0}. \quad (4)$$

2.2. Numerical Discretization

We use for the numerical simulations the shallow water option (SWE) introduced in the version 4.2 of the NEMO general circulation model (Madec & NEMO System Team, 2022). The initial state is at rest with $h_0 = 500$ m the uniform thickness of the active layer. Experiments are integrated over 25 years to achieve a steady state on h . All the simulations presented here use the Leap Frog Robert-Asselin time-stepping scheme (Leclair & Madec, 2009). In contrast, AM98 used the third order Adams-Bashforth (III) scheme. We do not expect the *spurious form drag* to be sensitive to the order of accuracy of the time-stepping scheme. We performed sensitivity tests with the third order Runge-Kutta method and found no noticeable differences in the equilibrium solutions (not shown).

Following AM98, we employ a Cartesian mesh with uniform resolution. Spatial resolution will be varied from $1/4^\circ$ to $1/48^\circ$. In the reference case, the mesh is aligned with the edges of the square basin, so that the model coastlines are perfectly straight (Figure 2, left). In the rotated cases, the mesh is oriented at some angle (up to 45°) with respect to the physical coastline, so that steps punctuate the model coastlines (Figure 2, right). Hence,

the comparison of aligned and misaligned cases allows us to assess potential drag effects of artificial coastal indentation. Both physics (e.g., wind stress, Coriolis parameter) and grid-cell size are kept unchanged when the mesh turns in relation to the physical basin, so that only the shape of the model coastline changes. Physical and numerical parameters are similar to AM98 and listed in Appendix A.

All the simulations solved in vector-invariant form and shown in this study use the potential-entrophy conserving vorticity scheme (called ENS) (Sadourny, 1975), except in Section 4.4 where we tested the scheme (called EEN) developed by Sadourny which conserves kinetic energy and—provided there is no divergence in the flow—potential entrophy (Burridge & Haseler, 1977). Tests showed that solutions using the kinetic energy conserving advection scheme (called ENE) (Sadourny, 1975) behave very similarly to the ones shown here with the ENS scheme. Note that AM98 used the “vorticity” scheme given by Bleck and Boudra (1986), which is similar to ENS except for the presence of the vertical scale factor h at the numerator and denominator in ENS (as required to effectively conserve a discrete expression of potential entrophy, Sadourny, 1975). Additional tests showed that “vorticity” and ENS schemes yield solutions that are slightly different but behave similarly in the presence of staircase-like coastlines. The expression of the various discretization schemes is given in Appendix B.

This configuration assumes an idealistic topography made of vertical walls and a flat bottom. However, the effective topography can be distorted by the traditional estimation of the thickness h at U, V, and F boundary nodes. In the open ocean on a C-grid, h is naturally defined at the center of each cell and calculated as a two-point (or four-point) average at velocity (or vorticity) nodes, for discrete conservation of properties. At the boundary, using the same definition and averaging with masked h can be equivalent to imposing sub-grid-scale topography, and can reinforce topography. Tests under ENS, ENE, and EEN advection schemes showed that simulations are sensitive to the treatment of h at the boundary (not shown), especially with EEN. We chose to calculate boundary h as the masked average of the surrounding masked heights, in order to actually represent vertical walls.

2.3. Boundary Condition

The system of Equations 1 and 2 or Equations 1–4 requires two horizontal boundary conditions to be well posed. The standard conditions on a solid wall consist of the impermeability condition $\mathbf{u} \cdot \mathbf{n} = 0$, with \mathbf{n} the coast-normal unit vector, and of a slipperiness condition that is a simplified representation of the effects of a viscous boundary layer.

AM98 considered two types of slipperiness condition (hereafter called *viscous boundary condition*): no-slip and free-slip. No-slip requires the tangential speed to be zero at the boundary which is $\mathbf{u} \cdot \mathbf{t} = 0$, with \mathbf{t} the coast-tangential unit vector. Combined with the impermeability condition ($\mathbf{u} \cdot \mathbf{n} = 0$), no-slip thus entails $\mathbf{u} = 0$ at the border. By contrast, free-slip is the absence of shearing and hence dissipation at the coast. It is defined as the absence of coast-normal shear at the border $\partial \mathbf{u} / \partial \mathbf{n} = 0$ and can be interpreted as a mirror condition across the border, where virtual flow within land mirrors the oceanic flow.

It is possible to deduce from the viscous boundary condition the value of the vorticity at the boundary. In their Section 2, Verron and Blayo (1996) write the vorticity ζ_c at an impermeable boundary regular enough to define in the local frame the vectors (\mathbf{n}, \mathbf{t}) , where \mathbf{n} is directed outward the basin:

$$\zeta_c = \left(\kappa \mathbf{u} - \frac{\partial \mathbf{u}}{\partial \mathbf{n}} \right) \cdot \mathbf{t}, \quad (5)$$

with κ the local curvature of the coastline (note that \mathbf{u} is a vector and $\partial \mathbf{u} / \partial \mathbf{n} = \nabla \mathbf{u} \cdot \mathbf{n}$ with $\nabla \mathbf{u}$ the 2×2 Jacobian matrix of \mathbf{u}). When the coastline is straight (κ tends to 0), the free-slip boundary condition reduces to $\zeta_c = 0$, while the no-slip boundary condition computes $\zeta_c = -(\partial \mathbf{u} / \partial \mathbf{n}) \cdot \mathbf{t}$ using $\mathbf{u} \cdot \mathbf{t} = 0$. When dealing with a numerical model, depending on the numerical grid and discretization schemes, the evaluation of a quantity on a grid-point near the boundary may require the use of another quantity at the boundary. It is for instance the case of ζ_c in the non-linear term in Equation 2, and the case of the rot-div formulation of the diffusive term. The boundary conditions therefore provide this information.

3. The Need for Physical Convergence

3.1. Influence of Resolution

The numerical parameters chosen by AM98 are those of an eddy-permitting OGCM: horizontal resolution is $1/4^\circ$, corresponding to a grid spacing $\Delta x = \Delta y = 25$ km. At this resolution, neither the internal radius of deformation R nor the boundary layers are properly resolved throughout the basin (Hallberg, 2013). Indeed, in the initial state,

the deformation radius is about 35 km at the northern boundary, so that $\Delta x \sim R$. It is therefore expected that increasing spatial resolution while keeping the same values for physical parameters (i.e., viscosity ν and friction r) will give solutions that differ from the reference solution of AM98.

Figure 3 shows the steady solution using the vector-invariant form of equations with the ENS advection scheme, the rot-div stress tensor and the free-slip boundary condition. From top to bottom, spatial resolution increases successively from $1/4^\circ$ to $1/8^\circ$, $1/16^\circ$ and $1/32^\circ$. The mesh is either aligned with the coastline (left column) or rotated by 45° (right column). The 45° angle creates an artificially indented coastline, as illustrated in Figure 2. Shading and isolines depict the layer thickness h . In all cases, we obtain an anticyclonic (clockwise) circulation composed of two connected cells: a relatively weak Sverdrup interior intensified at the western boundary in the southern 1,500 km of the domain, and an inertial recirculation sub-gyre confined to the northernmost 500 km. We find that some high resolution simulations vacillate in the eastern part of the recirculation cell; that is, the simulated flow displays an oscillatory behavior in this region over a timescale of about 18 months. Such vacillation is thought to occur in a very restrained parameter range (Holland & Haidvogel, 1981). To ensure consistent comparisons, all shown free-slip solutions are averaged over the final 5 years.

Panels (a) and (b), corresponding to a resolution of $1/4^\circ$, reproduce the results of AM98. At this resolution, the inertial recirculation cell extends all the way to the eastern boundary when the mesh is aligned with the physical coastline, whereas it occupies only the western half of the basin when the mesh is rotated by 45° . Hence, the free-slip circulation seems to dwindle as the mesh turns. However, the latter statement is no longer true with a fine spatial resolution. At $1/32^\circ$, the two solutions are virtually identical (Figures 3g and 3h). As apparent in the evolution of the shape and maximum of the northern recirculation, both aligned (Figures 3a, 3c, 3e, and 3g) and turned (Figures 3b, 3d, 3f, and 3h) solutions appear to tend toward the same state. Besides, solutions at $1/16^\circ$ look very similar to the ones obtained at $1/32^\circ$ meaning that the solutions are *physically* converged from $1/16^\circ$ (i.e., the main characteristics of the flow are almost insensitive to the increase of the mesh resolution).

The inertial recirculation sub-gyre is the most sensitive feature to resolution and mesh orientation. Hence, we choose to quantify the model sensitivity to the rotation and resolution of the grid using two diagnostics: the zonal extension of the inertial cell, and its overall intensity (calculated as the maximum of the active layer thickness within this cell). Figure 4 compares these diagnostics at different orientations of the mesh as a function of resolution. The extension (Figure 4a) and intensity (Figure 4b) of the rotated (dark blue dotted line) and aligned (red dotted line) solutions are very similar at $1/16^\circ$ and continue to get closer at the finest resolutions. Both characteristics rapidly tend toward those of the $1/48^\circ$ solution.

Figures 3 and 4 thus demonstrate that (a) the reference aligned solution should be the one obtained at $1/16^\circ$ resolution (Figure 3e - now taken as the reference) instead of $1/4^\circ$ (Figure 3a); and (b) the simulated circulation is insensitive to staircase-like coastlines provided that the model is physically converged to spatial resolution.

3.2. Preserving $1/4^\circ$ Staircase Steps

When increasing spatial resolution, the size of the coastal steps decreases as their number increases along the coastline. Is the insensitivity to mesh orientation at high resolution due to the smaller step size? To answer this question, we performed $1/16^\circ$ simulations with exaggerated coastal indentation (identical to its shape at $1/4^\circ$ resolution). In this way, we maintain the broken aspect of the shoreline unchanged while reducing the grid spacing. We find that the final free-slip solution (Figure 5a) is insensitive to the larger steps: it is almost identical to the reference aligned solution (Figure 3e). Hence, physical convergence allows the simulated circulation to be insensitive to mesh orientation and coastal indentation, irrespective of the size of coastal indents.

3.3. Condition for Physical Convergence

The zonal development of the northern recirculation cell results from a non-linear interaction between the sub-gyre and its mirror recirculation induced by the free-slip boundary condition (e.g., Figure 1 of Cessi (1991)). The northern region is also where the deformation radius is the smallest. This radius is about 35 km at the northern boundary in the initial state and it decreases over time because the westerly wind stress causes upwelling along the northern coast (thus shrinking h). Therefore, the deformation radius near the northern boundary is never properly resolved on a $1/4^\circ$ mesh. To assess whether resolution of the deformation radius along the northern

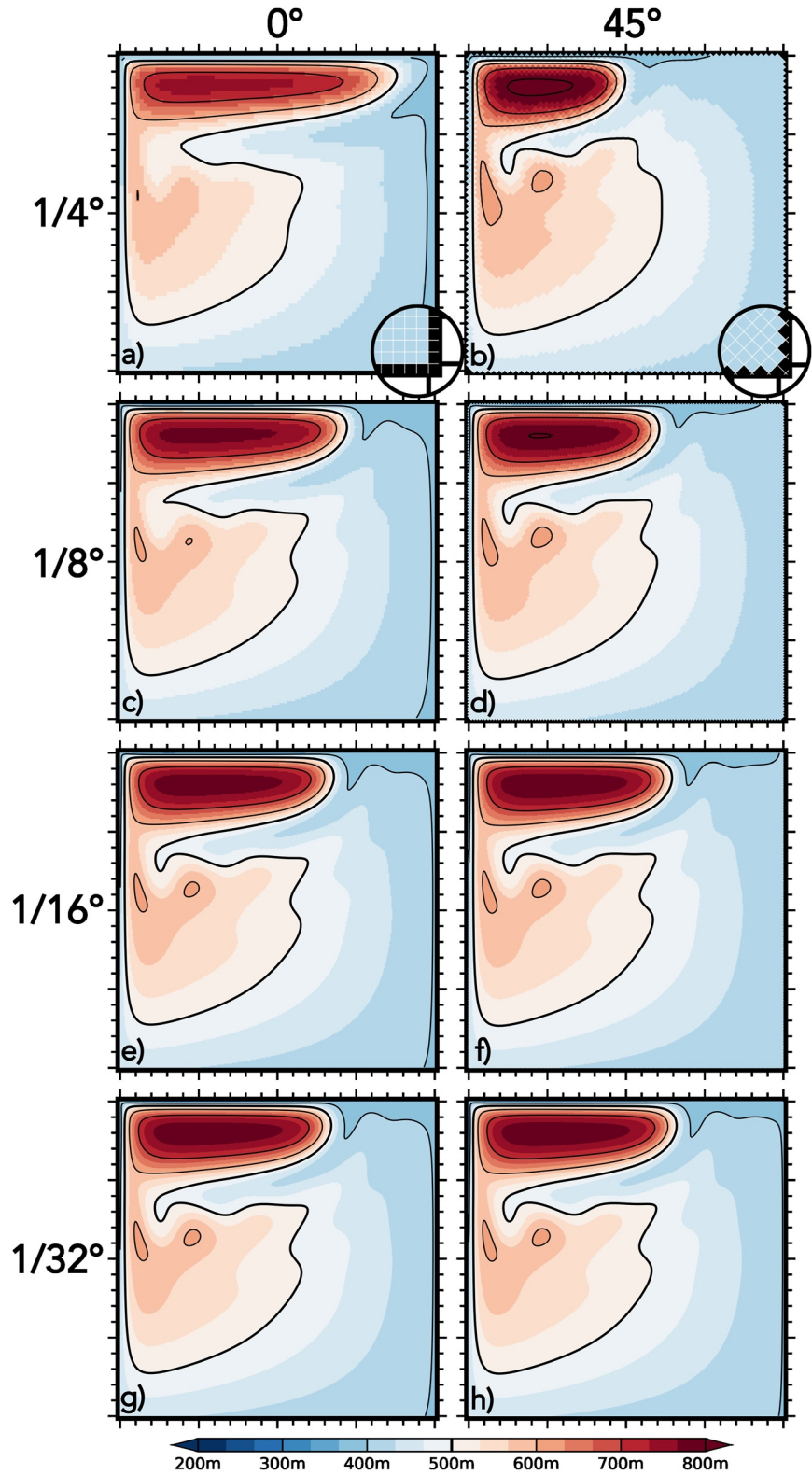


Figure 3. Free-slip solutions solved in vector-invariant form under ENS using the rot-div stress tensor. Shading and isolines (in black) depict the active layer thickness h (isoline 500 m is thickened). x and y main ticks are 500 km apart. In the left column (a, c, e, g), the mesh is aligned with the borders of the basin. In the right column (b, d, f, h), the mesh is turned at 45° relative to the borders, as illustrated in the bottom-right zooms. The spatial resolution increases from top to bottom: (a, b) $1/4^\circ$, (c, d) $1/8^\circ$, (e, f) $1/16^\circ$ and (g, h) $1/32^\circ$.

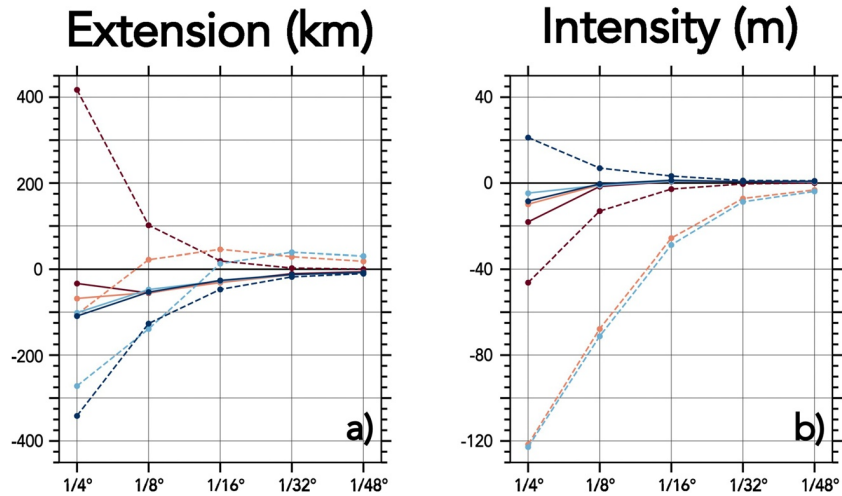


Figure 4. Extension and intensity of the free-slip solutions solved in vector-invariant form using the rot-div stress tensor. The extension of the inertial recirculation cell (a) is the zonal length (in km) measured between the two most distant points on the 500 m isoline of upper-layer h . Its intensity (b) is the maximum (in m) of the active layer thickness h . Both quantities are plotted as a function of mesh resolution, and are shown as a difference relative to values from the finest aligned solution ($1/48^\circ$) resolved under ENS (these values are 1,311 km and 794 m). Dotted lines (solid lines) depict solutions solved under ENS (EEN) scheme. The sequence of colors (red, orange, light blue and dark blue) marks the orientation of the mesh (aligned, 10° , 30° , and 45° , respectively).

frontier is key to obtain physical convergence, we performed experiments where the aligned, $1/4^\circ$ mesh is refined in a narrow northern band. Specifically, we reduce the meridional grid spacing from $1/4^\circ$ 300 km offshore to $1/16^\circ$ at the northernmost grid cells.

Figure 5b shows that refining the meridional grid spacing near the northern boundary contracts the inertial recirculation sub-gyre (compare with Figure 3a). Local grid refinement thus suffices to bring this recirculation cell closer to the physically converged solution (Figure 3e) than to the initial $1/4^\circ$ solution (Figure 3a). Analogous sensitivity tests with local mesh refinement close to the western, southern or eastern coast showed very little impact on the solution (not shown). Resolving the northern deformation radius, hence the mirror interaction at the north boundary, appears to be the key ingredient for physical convergence. We infer that a minimum of four grid points per deformation radius is necessary.

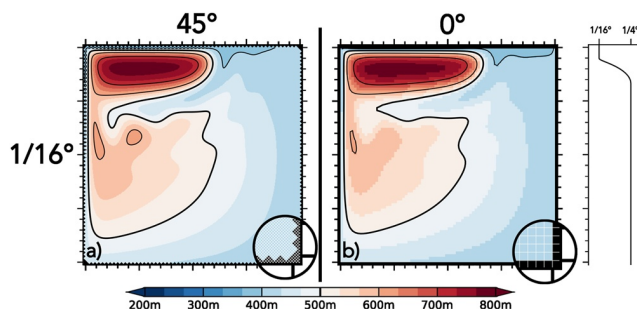


Figure 5. Free-slip solution solved in vector-invariant form under ENS using the rot-div stress tensor. Shading and isolines (in black) depict the active layer thickness h (isoline 500 m is thickened). x and y main ticks are 500 km apart. (a) The mesh is oriented at 45° and the spatial resolution $1/16^\circ$ but coastal steps remain of size corresponding to $1/4^\circ$ resolution. (b) The mesh is aligned and uniformly at $1/4^\circ$ except within 300 km of the north coast where the meridional spatial resolution is refined from $1/4^\circ$ to $1/16^\circ$ (as illustrated in the right-end panel).

3.4. No-Slip Boundary Condition

All experiments up to here have been conducted using the free-slip boundary condition. The no-slip boundary condition may be expected to generate weaker circulation cells and weaker sensitivity to mesh orientation (AM98). Figure 6 shows no-slip solutions using aligned (left) and 45° -rotated (right) meshes, at $1/4^\circ$ (top) and $1/16^\circ$ (bottom) resolution. Under no-slip, there is no large recirculation cell in the northern part of the domain and the zonal transport is two times weaker there. Instead, no-slip solutions converge in time toward an oscillating small gyre nestled in the north-west corner. At $1/4^\circ$ resolution, a 45° rotation of the mesh causes the small gyre to shift south by about 200 km (Figures 6a and 6b). At $1/16^\circ$ resolution, this sensitivity vanishes (Figures 6c and 6d). Hence, insensitivity to mesh orientation is again achieved provided that spatial resolution is sufficiently fine. The same conclusion holds when no-slip is applied in the symmetric stress tensor formulation (not shown).

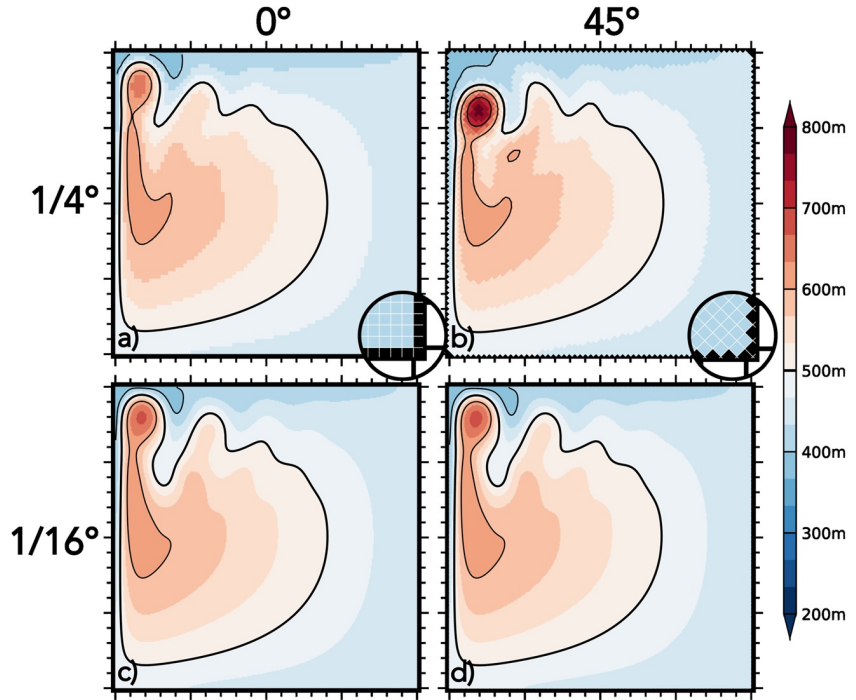


Figure 6. No-slip solutions solved in vector-invariant form under ENS with the rot-div stress tensor. Shading and isolines (in black) depict the active layer thickness h (isoline 500 m is thickened). x and y main ticks are 500 km apart. In the left column, the mesh is aligned with the physical coastline. In the right column, the mesh is 45°-turned. Spatial resolution is 1/4° in the top row and 1/16° in the bottom row. Because the final state steadily oscillates over periods of roughly 5 months (linked to the generation of Rossby waves), the shown solution is extracted by averaging over the last 10 years of the simulation.

4. True Mirror Boundary Condition Achieves Slipperiness

4.1. Symmetric Stress Tensor

A major caveat pointed out in AM98 is the extreme sensitivity to mesh orientation of free-slip solutions that resort to the symmetric viscous stress tensor. Figure 7 shows solutions using the free-slip boundary condition and the symmetric stress tensor. When the mesh is aligned with the physical coastline (Figures 7a and 7d), the model behavior is qualitatively similar to what was obtained using the rot-div stress tensor (Figures 3a and 3e). However, when the mesh is rotated by 45° (Figures 7b and 7e), both coarse and fine solutions change starkly and resemble no-slip solutions (Figure 6) as pointed out in AM98. Hence, the free-slip boundary condition combined with the symmetric stress tensor appears to act as no-slip when the mesh is oriented at 45°, which suggests that its implementation is not suitable. We next examine how to recover a true free-slip condition on the 45°-turned mesh using the symmetric tensor.

When the mesh is not aligned with the physical coastline, the original straight boundaries become broken or indented in the model. To faithfully represent boundary flows, boundary conditions should be written with respect to the original, physical land-ocean frontier. For example, at 45°, the physical shoreline goes through T and F nodes (Figure 8). A free-slip condition is a mirror condition at the coast (e.g., Shchepetkin & O'Brien, 1996). Therefore, we should set virtual flows on “ghost nodes” (AM98), within land grid cells, that are symmetric to the ocean flows with respect to the physical shoreline. These virtual velocities are only used to evaluate the lateral friction term along the border. The example of a western coastline is illustrated in Figure 8. In this case, the mirror condition writes

$$\tilde{u}_{i,j+1} = v_{i+1,j} \quad (6)$$

$$\tilde{v}_{i,j} = u_{i,j}, \quad (7)$$

where the tilde is used to denote inland virtual velocities. It is the same condition as proposed by Griffiths (2013) in the context of Kelvin waves. Both anti-diagonal (D_s or ζ) and diagonal (D_T or χ) rates of deformation, defined

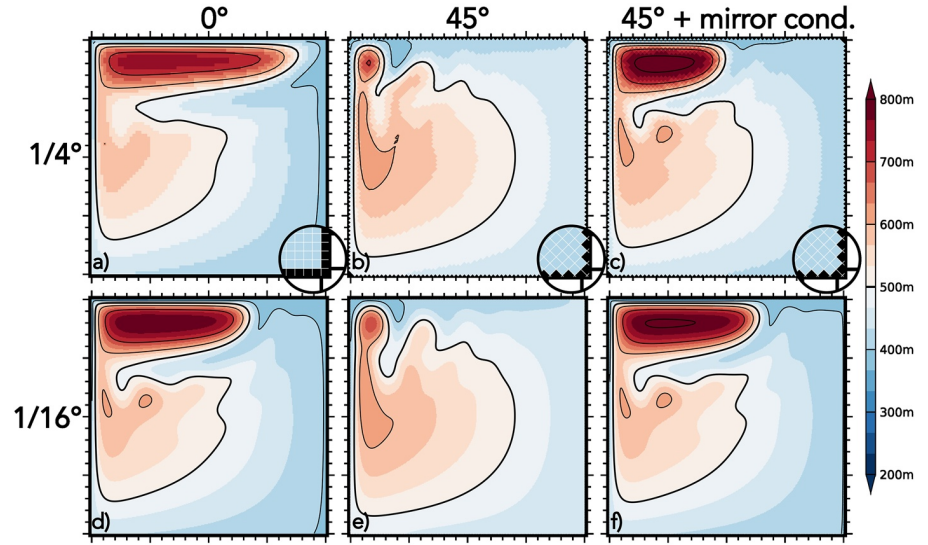


Figure 7. Free-slip solutions solved in vector-invariant form under ENS using the symmetric stress tensor. Shading and isolines (in black) depict the active layer thickness h (isoline 500 m is thickened). x and y main ticks are 500 km apart. Spatial resolution is $1/4^\circ$ in the top row and $1/16^\circ$ in the bottom row. In the left column, the mesh is aligned with the physical coastline. In the middle and right columns, the mesh is 45° -turned. The first two columns use the traditional free-slip implementation in the symmetric tensor ($D_s = 0$), whereas the third column uses the mirror condition proposed in Equations 6 and 7.

at vorticity and tracer points respectively, are then deduced from this mirror condition. In particular, for a uniform grid spacing $\Delta x (= \Delta y)$, we have

$$(D_s)_{i,j} = \frac{1}{\Delta y}(\tilde{u}_{i,j+1} - u_{i,j}) + \frac{1}{\Delta x}(v_{i+1,j} - \tilde{v}_{i,j}) = \frac{2}{\Delta x}(v_{i+1,j} - u_{i,j}). \quad (8)$$

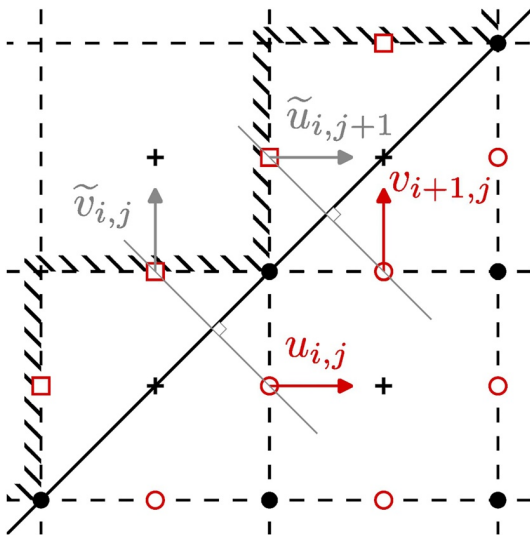


Figure 8. Schematic presenting a mirror condition on the western coastline. Land grid cells are located west of the black hatching. The original, physical coastline, goes through the diagonals of the cells and is drawn in solid black. Red circles locate velocity points (F nodes) and black crosses height points (T nodes), as is standard for a C-grid. Red squares mark boundary nodes or “ghost nodes” where virtual velocities are defined. Example oceanic velocities are shown by red arrows, mirrored by the virtual velocities shown with gray arrows.

Hence, D_s is not zero at the tips of the coastal steps, but instead doubled compared to the value obtained with zero virtual inland velocities. This is contrary to the traditional implementation of free-slip in the symmetric tensor, which sets $D_s = 0$ at the boundary. $D_s = 0$ is the correct condition when the numerical and physical shorelines perfectly coincide but fails when they are misaligned. Note that zero vorticity condition is ensured at the boundary F nodes with the mirror condition (Equations 6 and 7).

The no-slip condition can be defined following the same rationale, by setting inland virtual velocities as the opposite to their oceanic mirrors:

$$\tilde{u}_{i,j+1} = -v_{i+1,j} \quad (9)$$

$$\tilde{v}_{i,j} = -u_{i,j}. \quad (10)$$

The proposed free-slip and no-slip conditions for a 45° -turned mesh and either stress tensor are summarized in Table 1. Their implementation consists in multiplying the factors defined in Table 1 with the rates of deformation estimated in the trivial case of zero (masked) velocities at the boundary and inland. Note that we could have considered that the physical shoreline goes through (U, V) nodes, as AM98, instead of (T, F) nodes. In this case, the mirror condition requires a slightly more complex interpolation of the virtual velocities.

We implemented the proposed free-slip condition in the symmetric stress tensor and assessed the impact on the equilibrium solution with a 45° -turned mesh (Figures 7c and 7f). In contrast to previous results which relied on

Table 1
Proposed Viscous Boundary Conditions for a Uniform and 45°-Turned Mesh

	Free-slip	No-slip
$\sigma_{\zeta,D}$	$\zeta \times 0$	$\zeta \times 2$
	$\chi \times 2$	$\chi \times 0$
σ_{sym}	$D_S \times 2$	$D_S \times 0$
	$D_T \times 0$	$D_T \times 2$

Note. The table gives the modifications of quantities used in either tensor to be implemented at the coast, relative to the trivial case of zero virtual velocities. The top row describes quantities of the rot-div tensor while the bottom row describes quantities of the symmetric tensor, as defined in Section 2.1.

the standard free-slip boundary condition (Figures 7b and 7e), a true free-slip circulation is simulated with a northern recirculation cell that extends roughly to the middle of the basin. The solutions in Figures 7c and 7f are very similar to those previously obtained with the rot-div tensor (Figures 3b and 3f). Our simulations thus confirm that the traditional way of applying free-slip in the symmetric tensor ($D_S = 0$) is not suitable when the mesh is misaligned with the coastline.

We stress that setting only D_S at the tips of steps is insufficient to obtain a true free-slip solution (not shown). Boundary conditions on both D_S and D_T are necessary to make the indented coastline slippery using the symmetric tensor. In contrast, canceling only ζ in the rot-div tensor proved to be enough to achieve slipperiness; doubling χ only brought minor changes. Since the condition $\zeta = 0$ at the coast was already implemented in the experiments described in Section 3, a correct free-slip behavior was simulated.

4.2. Flux-Form Equations

All numerical experiments documented above were solved in vector-invariant form (Equation 2). How slippery are staircase-like coastlines in a model solved in flux form (Equation 4)? Figure 9 shows the steady flux-form solutions on aligned (Figures 9a and 9d) and 45°-turned (Figures 9b, 9c, 9e, and 9f) meshes at 1/4° (top row) and 1/16° (bottom row) resolution, using the rot-div stress tensor. Figures 9a and 9d reveals the same contraction of the northern recirculation cell with increasing resolution as found previously (Figures 3a and 3e) on the aligned mesh. However, when the mesh is turned and the coastline becomes indented, solutions become akin to no-slip: a small gyre is nestled in the northwest corner in an oscillatory steady state (Figures 9b and 9e).

By construction, there is no viscous boundary condition applied in flux-form advection, only the impermeability condition holds. The viscous boundary condition is free-slip and implemented in the rot-div stress tensor. Under such parameters, a coastal step tends to generate filaments of opposite vorticity that cause the coastal current to retroreflect (Deremble et al., 2016; see also Section 5). Therefore, solutions solved in flux-form are expected to be sensitive to the presence of steps, as retroflection dynamics hinder along-boundary flow.

To remedy this sensitivity to mesh orientation, we implemented the same mirror condition (Equations 6 and 7) but in the advective trend, by enforcing velocities at the coast to satisfy this condition. The result is shown in

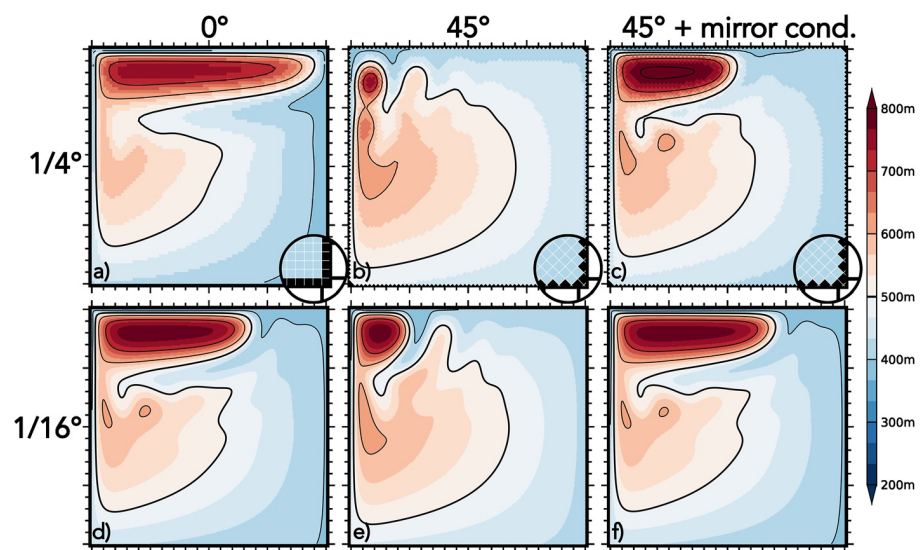


Figure 9. Free-slip solutions solved in flux form using the rot-div stress tensor. Shading and isolines (in black) depict the active layer thickness h (isoline 500 m is thickened). x and y main ticks are 500 km apart. Spatial resolution is 1/4° (top row) and 1/16° (lower row). In the first column (a, d), the mesh is aligned so the coastline is straight. Second and third columns (b, c, e, f) have the mesh rotated at 45°. In the third column, a mirror condition is enforced in the advective trend.

Figures 9c and 9f for the 45°-turned mesh. We obtain a sizable inertial recirculation cell in the northern part of the basin, with zonal extensions close to the previous solutions (Figures 3b, 3d, 3f, and 3h and Figures 7c and 7f). Hence, enforcing the free-slip condition in both the diffusive and advective terms makes staircase-like coastlines slippery, including with flux-form equations.

4.3. Intermediate Angles

At 1/4° resolution, the fully indented coastline (Figure 3b) leads to a solution closer to the converged solution (Figures 3e–3h) than does the straight coastline (Figure 3a). At intermediate orientations of the mesh (strictly between 0° and 45°), the coastline counts fewer outgoing angles than at 45°, and a solution midway between the aligned and 45°-turned cases might be expected. In reality, intermediate angles generate solutions that depart much more from the converged solution (Figure 10). Figure 10 uses the exact same numerical choices as Figure 3 except for the mesh orientation, which is either 10° (left column) or 30° (right column). At these orientations, the inertial recirculation cell expands toward the east between 1/4° and 1/16°, then contracts with resolution (Figure 10). Solutions (not shown) performed on 1/48° mesh are not significantly different from the ones obtained on 1/32° mesh (Figures 10g and 10h) meaning that physical convergence is reached near 1/32°. The curves plotted in Figure 4 for 10° (orange dotted line) and 30° (light blue dotted line) orientations confirm and quantify these results. Interestingly, the 1/48° solutions at intermediate angles depart from the aligned solution (Figure 4): their recirculation cells are wider by about 30 km, and weaker by about 5 m. It is puzzling that different converged solutions seem to exist for different orientations; one might have expected that the same solution be reached across all orientations at very fine resolution.

Why do solutions at intermediate angles differ from their aligned and 45°-turned counterparts? Once the model is converged, dynamics inside the domain must be well captured independently of the orientation of the grid, so that differences are expected to lie at the borders. If the mesh is aligned (Figure 11, left) or turned at 45° (Figure 11, right), the physical coastline coincides with the F nodes of the C-grid and the free-slip condition $\zeta = 0$ exactly matches that of a straight coastline. At intermediate angles however, this condition is inaccurate because the free-slip boundary resulting in the model (red dotted line) is not straight but corrugated (Figure 11, middle). Imposing $\zeta = 0$ on the tips does make artificial steps slippery yet does not achieve the true free-slip condition of a straight coastline. We expect that defining the free-slip condition with respect to a straight boundary would yield the same solutions and convergence rate as with the aligned mesh.

In other words, to accurately represent the free-slip condition, virtual inland velocities should be interpolated as the mirrors of the ocean flows with respect to the straight shoreline. Such a strategy would presumably allow to retrieve a true free-slip behavior also with advection in flux form, and with the symmetric stress tensor, for any orientation of the mesh. We have not endeavored such an interpolation at intermediate angles, for it is tedious and would not generalize to arbitrary (curved) physical shorelines. Instead, we suggest using more general techniques such as immersed boundary methods (Causon et al., 2000; Ketefian & Jacobson, 2011; Kirkpatrick et al., 2003).

4.4. Benefit of Wide Stencils

Strictly speaking, the mirror condition should apply in each term of the equations. For example, on the 45° oriented mesh within oceanic cells along the border, this would double the kinetic energy and $\partial_t h$ in Equations 1 and 2 respectively, while the vertical scale factor h and the Coriolis term at the outgoing vorticity points would be mirrored with respect to the cell diagonals. However, our implementation of these conditions did not bring noticeable changes on the 45°-turned solution (not shown), which is already very close to the reference. This result indicates that the sensitivity of circulation within this configuration is controlled primarily by the formulation of advective and diffusive terms, in accord with Dupont et al. (2003).

Motivated by the sensitivity of solutions to the discrete formulation of advection, we investigated the impacts of mesh orientation and coastline indentation using a different advection scheme (EEN). Results are shown in Figure 12 under the free-slip boundary condition. The mesh is progressively turned from left to right (0°, 10°, 30°, and 45°) and spatial resolution increases from 1/4° to 1/8°. First, we find that the aligned and intermediate solutions are physically converged at 1/8° resolution (1/16° not shown), contrary to solutions that resorted to ENS or ENE. Second, all solutions are very similar across mesh orientations, even at 1/4° resolution, with a recirculation cell that extends halfway through the basin. These results are quantified in Figure 4 which shows that EEN-based solutions (in solid lines) are virtually identical as early as 1/8°, and that they converge together to the same state as ENS-based solutions as resolution increases to 1/48°.

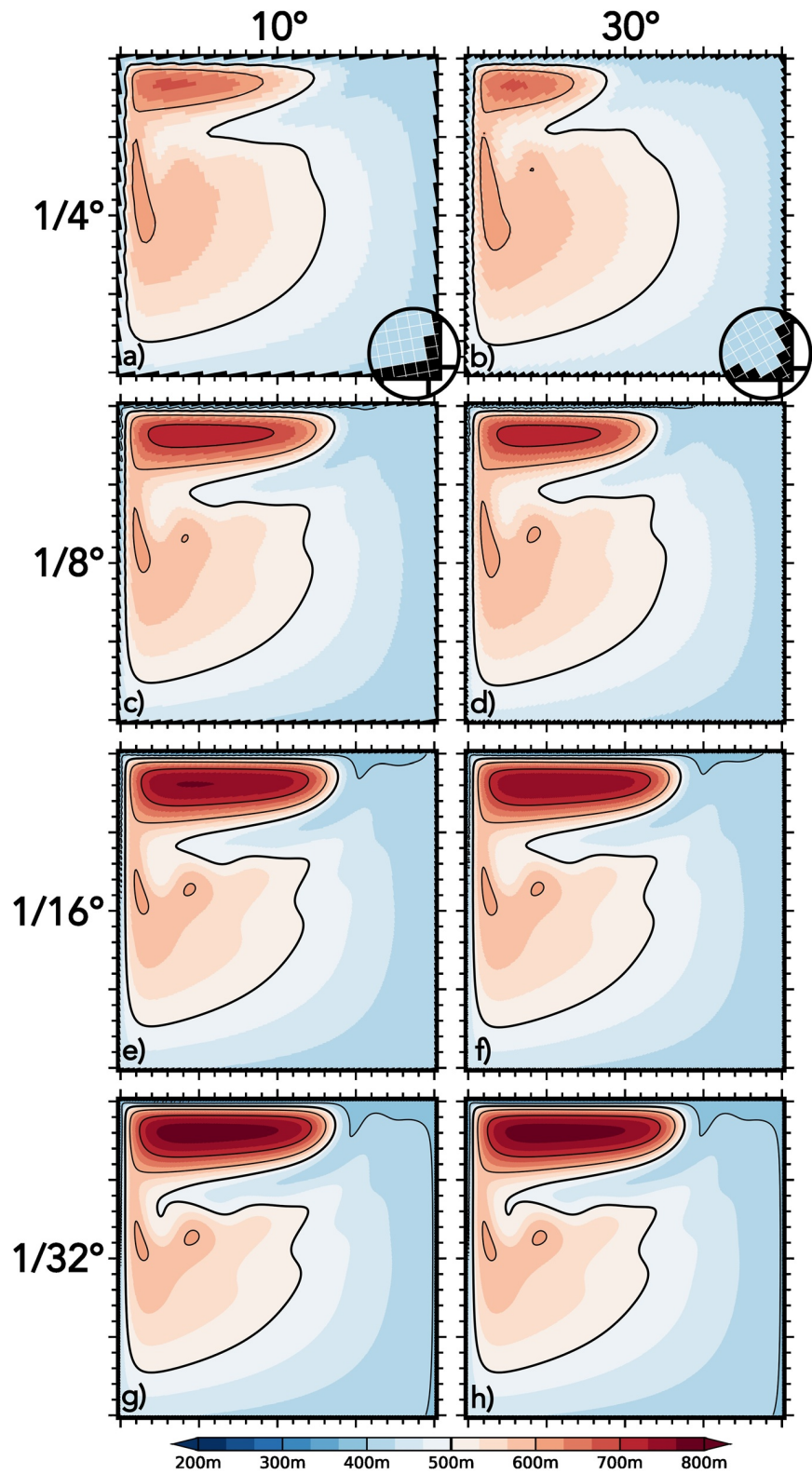


Figure 10. Free-slip solutions solved in vector-invariant form under ENS using the rot-div stress tensor. Shading and isolines (in black) depict the active layer thickness h (isoline 500 m is thickened). x and y main ticks are 500 km apart. The mesh orientation is 10° (left) and 30° (right). Spatial resolution increases from top to bottom: $1/4^\circ$, $1/8^\circ$, $1/16^\circ$, and $1/32^\circ$.

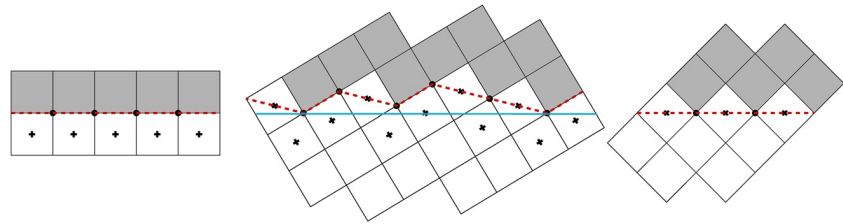


Figure 11. Representation on a C-grid of a straight shoreline with the piecewise constant approximation. The black disks are the vorticity (F) nodes and the crosses are the height (T) points. The numerical frontier (red dotted line) connects the vorticity nodes that influence the dynamics. In the aligned case (left) the numerical frontier occupies cell faces and joins F nodes so it coincides with a straight coastline. In a similar way, the numerical frontier in the 45°-turned case (right) goes through cell diagonals, hence intersecting F and T nodes. In the intermediate case (middle), the closest vorticity points to the targeted straight coastline (in blue) are not aligned, resulting in a slithering numerical frontier.

Vorticity schemes previously used in this study have a 7-point wide stencil, whereas the EEN scheme has a 17-point wide stencil (see Figure B1). We infer that the larger stencil of the EEN scheme effectively smoothens the discontinuity of the coast, making dynamics much less sensitive to the misalignment of the grid with the physical shorelines. These results advocate for the use of schemes having relatively wide stencils, possibly high-order schemes, to minimize spurious effects of staircase-like coastlines.

5. From Straight to Swerving Coastlines

5.1. Dynamics Along a Cornered Coastline

In the previous sections, we explored ways to eliminate spurious effects of artificial steps in model coastlines. However, coastal steps are not always artificial and their effects not necessarily spurious, since real coastlines contain sharp turns that exceed the grid scale and impact boundary currents. For example, a protruding corner in the coastline can cause boundary currents to retroreflect (Dengg, 1993), impacting the larger scale circulation (Ansorge & Lutjeharms, 2005; Weeks et al., 2010). Which boundary conditions are most appropriate to model this physical response to a coastal step?

To address this question, we reproduce the configuration of Deremble et al. (2016). The domain is a square basin of 500 km in length, cropped by a 100 km \times 250 km land mass at the southwest end, as illustrated by the gray shading in Figure 13. The equations solved are those given in Section 2.1, except that the model is barotropic and excludes wind forcing, bottom friction and the Coriolis effect (parameters are given in Appendix A). The simulation starts with a vortex of negative relative vorticity, standing near the eastern side of the land mass (Figure 13a). The vortex is then advected up to the corner due to non-linear interaction with the straight coastline. When the

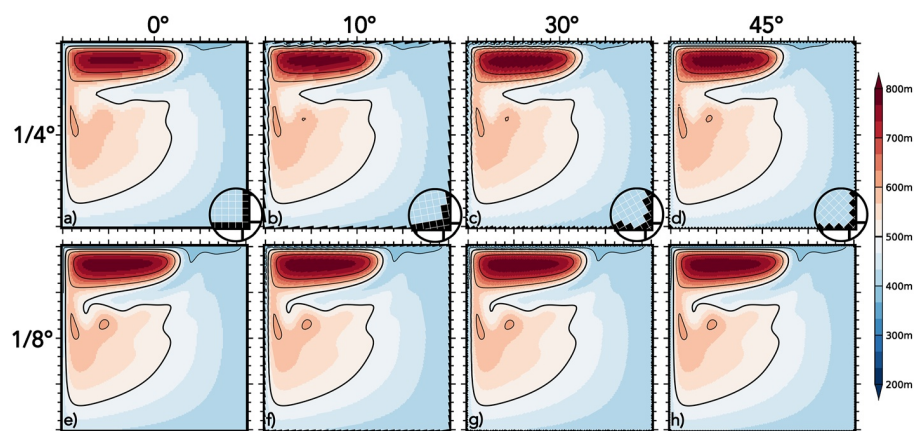


Figure 12. Free-slip solutions solved in vector-invariant form with the EEN advection scheme and the rot-div stress tensor. Shading and isolines (in black) depict the active layer thickness h (isoline 500 m is thickened). x and y main ticks are 500 km apart. From left to right, the mesh is progressively rotated, at 0°, 10°, 30°, and 45° with respect to the physical coastline. Spatial resolution increases from 1/4° (top) to 1/8° (bottom).

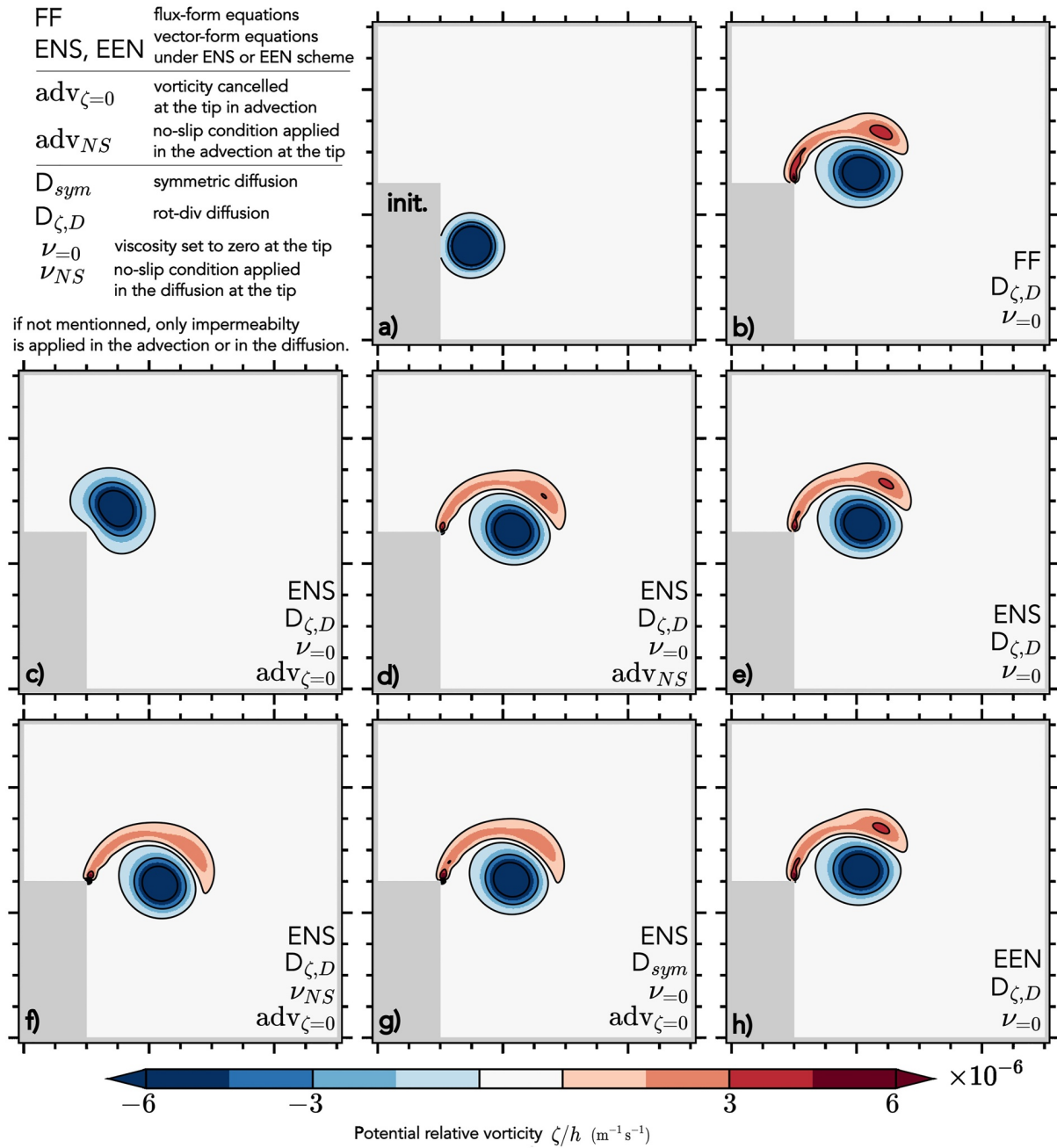


Figure 13. Potential relative vorticity field illustrating the interaction between a cyclonic vortex and a cornered coastline. Panel (a) shows the initial state, (b–h) are snapshots of the potential relative vorticity field after 45 days. Isolines are equivalent to streamlines in this configuration. On all walls, the free-slip boundary condition is applied in advection (vector-invariant form equations only) and in diffusion on both sides of the land mass—except at the tip where different treatments are assessed. Each of these treatments is specified in the bottom right corner of each panel, following notations defined at the top left of the figure.

vortex begins to overtake the corner, filaments of positive vorticity are generated at the tip, forcing the retroflection of the flow as explained by Deremble et al. (2016). Figure 13b shows the vortex detaching from the coast along a filament of opposite relative vorticity that stretches northeastward from the tip.

5.2. Lateral Boundary Conditions

On a large-scale isolated step, the definitions of the boundary conditions given in Section 2.3 are less straightforward as it is no longer possible to define the local vectors (\mathbf{n} , \mathbf{t}) at the singularity. A no-slip condition ($\mathbf{u} = 0$)

could potentially hold by continuous extension from the adjacent walls to the tip. However, the definition of the free-slip viscous boundary condition becomes unclear as the normal derivative of the flow is unknown at the tip. Furthermore, by bending a regular coastline toward the limiting case of a protruding corner (κ tends to infinity), the vorticity in Equation 5 becomes infinite, suggesting that a singularity in the coastline acts as a source of vorticity in the flow (Deremble et al., 2016).

Dengg (1993) argued that the retroflexion of a boundary current at a cape is better captured in numerical simulations when a no-slip viscous condition is used instead of free-slip. However, Deremble et al. (2016) described analytically the detachment or retroflexion of a vortex under the assumption of no dissipation, with only advection as the driver. They showed that such retroflexion requires only impermeability conditions along both side of the walls in the advective trend.

Here we extend this result to several numerical formulations of advection, showing that retroflexion is faithfully represented when viscosity ν is set to zero at the F-node of the singularity (Figures 13b, 13e, and 13h). With flux-form equations, there is no required viscous boundary condition in advection, so that only impermeability is imposed and retroflexion is simulated (Figure 13b). With vector-invariant equations, retroflexion is also captured under either ENS (Figure 13e), ENE (not shown) or EEN (Figure 13h) advection schemes when using the impermeability condition to estimate vorticity at the tip. However, if relative vorticity is enforced to vanish at the tip ($\zeta_c = 0$), the retroflexion is no longer simulated (Figure 13c). The enforcement of zero vorticity is equivalent to applying a free-slip viscous condition; this result thus matches previous reports that free-slip can suppress retroflexion (Dengg, 1993; Deremble et al., 2016; Dupont & Straub, 2004). If instead a no-slip condition is applied at the tip, vorticity filaments change intensity but are still represented (compare Figure 13d with Figures 13b, 13e, and 13h).

When neutralizing the retroflexion effect in the advection term (by imposing $\zeta_c = 0$ at the tip in the advective trends), it is still possible to recover the filament generation through the viscous dissipation. Indeed, with a non-zero viscosity ν set at the singularity, retroflexion is simulated by applying the no-slip viscous boundary condition in the diffusive term (Figure 13f). However the filament of positive relative vorticity is different in shape and intensity (compare Figure 13f with Figures 13b, 13e, and 13h), its characteristics become more sensitive to the chosen value of viscosity ν (not shown), and its physical interpretation as the detachment of the viscous boundary layer (Deremble et al., 2016) is less straightforward.

The rot-div stress tensor is used for diffusion in the solutions discussed above (Figures 13b–13f and 13h). In Figure 13g, we show a solution that uses the symmetric stress tensor combined with the viscosity ν set to zero at the outgoing corner. The solution is quite similar to that obtained using the no-slip viscous condition in the rot-div stress tensor (Figure 13f). This result concurs with those of Section 4 and emphasizes the problematic behavior of the traditional implementation of slipperiness in the symmetric tensor. These findings also explain why Dupont and Straub (2004) and Deremble et al. (2016) obtained unexpected behaviors at coastal tips when using the combination of symmetric tensor and free-slip viscous boundary condition: in effect, this combination produces no-slip on steps.

To summarize, our experiments demonstrate that the detachment of a vortex can be represented in the absence of dissipation by estimating the vorticity at the tip using either impermeable or no-slip conditions. By applying a zero vorticity condition at a coast's singularity, the generation of filaments of opposite vorticity and the retroflexion of a current are instead prevented, as explained by Equation 5 and illustrated in Figure 13c. We disentangled the effect of the viscous boundary condition at the singularity under various formulations for advection (vector-invariant and flux-form equations) and diffusion (rot-div and symmetric stress tensors). The results highlight the inadequacy of the usual formulation of free-slip (zero vorticity) to simulate the lateral interaction of a boundary current with a cape, and potentially analogous flow-topography interactions along curved coastlines, as suggested by previous work (Dupont & Straub, 2004).

5.3. Implications for Staircase-Like Coastlines

Staircase-like coastlines studied in Sections 3 and 4 using the AM98 configuration can be viewed as a series of small isolated steps. Each step may be expected to have a dynamical effect on the local circulation as described in Section 5.2, and the ensemble of steps may have a cumulative impact on the basin-scale gyres. For example, the behavior of solutions using only the impermeability condition, as it is the case in flux-form equations on the

45°-rotated mesh (Figures 9b and 9e), can be understood by noting that each step works to retroreflect the boundary flow and ultimately distort the gyre circulation. Indeed, in these simulations the viscous boundary condition is free-slip and is applied only in the diffusive term. Therefore, the lack of a zonally extended inertial recirculation (Figures 9b and 9e) likely stems from the retroreflection—induced by the advection term—of the boundary current on the indented coastline. Interestingly, increasing spatial resolution (while keeping viscosity ν and friction r unchanged) allows the inertial recirculation gyre to grow eastward (compare Figure 9e with Figure 9b). An additional simulation (not shown) at a finer resolution of $1/32^\circ$ confirms this tendency: the inertial recirculation cell then occupies over half of the basin. We interpret this behavior as the consequence of the reduction of the scale of steps ($1/32^\circ$) relative to the width of the boundary currents ($\sim 1/4^\circ$): the production of vorticity filaments, which feeds upon the discontinuity in the flow field across the tips of steps (Deremble et al., 2016), is damped if steps are too small to generate sizable discontinuities.

6. Conclusions

We revisited the “staircase problem” highlighted by Adcroft and Marshall (1998), who exposed the existence of a spurious form drag when smooth coastlines are numerically transformed into steps. We reproduced their configuration, which consists of a square closed basin under shallow water dynamics and cyclonic wind forcing, simulated on a Cartesian mesh with varying orientation. We tested various mesh resolutions with many combinations of advection formulations (flux or vector-invariant forms of equations with potential-*enstrophy* (ENS), energy (ENE) or energy and potential-*enstrophy* (EEN) conserving schemes developed by Sadourny) and two commonly used viscous stress tensors (rot-div and symmetric formulations).

We first show that the free-slip non-rotated solution is not physically converged at $1/4^\circ$ resolution, under ENS or ENE with the rot-div stress tensor, but only from $1/16^\circ$ with the same viscosity and friction parameters as AM98. By *physical convergence* we mean the insensitivity of the main characteristics of the flow to further increase of the mesh resolution. Such convergence requires to resolve the inertial dynamics induced by the free-slip (i.e., mirror) boundary condition along the northern coast by having at least four grid points per internal radius of deformation, which is close to 30 km in this region.

In addition, we find that the 45°-rotated free-slip solution is also physically converged from $1/16^\circ$ resolution and surprisingly looks almost identical to the aligned $1/16^\circ$ solution, contrary to AM98. The reason is that the free-slip boundary condition (zero vorticity) applied at the tips of coastal indents created by the 45°-rotated mesh exactly stands for a straight shoreline passing through T and F nodes of a C-grid. At intermediate angles of mesh orientation (strictly between 0° and 45°), physically converged solutions are only achieved near $1/32^\circ$ resolution and depart from the non- or 45°-rotated $1/16^\circ$ solution. We suggest that the different sensitivity and delayed convergence at intermediate angles stem from inaccurate declaration of the free-slip boundary condition as the resulting numerical frontier is corrugated, not straight.

The above-mentioned results hold in vector-invariant form with the ENS or ENE scheme combined with the rot-div stress tensor. When switching to the symmetric stress tensor or to flux-form advection, rotated solutions no longer converge toward the reference (aligned) solution and instead resemble no-slip solutions. In both cases, applying a *true* mirror boundary condition with respect to the physical coastline on the 45°-rotated mesh allows to retrieve solutions close to the reference at $1/16^\circ$ resolution. These results pinpoint the spurious behavior of the traditional implementation of “free-slip” in the symmetric viscous tensor, which works as intended only if the mesh is aligned with the border.

Importantly, using an advection scheme with a larger stencil (EEN in vector-invariant form) makes the free-slip solutions virtually identical from $1/8^\circ$ for any orientation of the mesh. We infer that larger stencils allow advection schemes and the simulated circulation to become much less sensitive to broken coastlines, providing a practical avenue to mitigate spurious effects of piecewise-constant land-ocean frontiers.

In addition to exposing ways to eliminate spurious effects of artificial coastal steps, we explored the numerical treatment of a single sharp turn in the physical coastline, using the configuration of Deremble et al. (2016). One expected impact of a large protruding corner in the coastline is the generation of vorticity filaments that force the boundary current to retroreflect (Deremble et al., 2016). We show that the retroreflection is faithfully captured by advection if expressed in flux form, which disallows the use of a viscous condition, or in

vector-invariant form, provided an impermeability or no-slip condition is applied at the maxima of curvature. In contrast, using a free-slip (zero vorticity) viscous boundary condition at the tip suppresses the retroflection entirely.

We conclude that staircase-like coastlines can behave like straight and slippery coastlines provided that coastal dynamics are physically resolved and that an accurate mirror boundary condition is used. Naturally, in realistic OGCM configurations, it is not always feasible nor desirable to increase resolution whilst keeping viscosity unchanged to achieve physical convergence. To minimize spurious effects of artificial steps in OGCM boundaries, we thus recommend the use of advection schemes with large stencils (such as the energy-entropy conserving (EEN) scheme), combined with free-slip (zero vorticity) boundary conditions and the rot-div viscous stress tensor. If flux-form equations or the symmetric stress tensor are chosen, free-slip along staircase-like coastlines is best implemented with general techniques such as immersed boundary methods. However, when coastal steps represent sharp turns in the real coastline that cause boundary currents to retroflect, perfect slipperiness is no longer desirable as it may suppress retroflection. In this case, application of impermeability or no-slip conditions can better represent physical flow-topography interactions than a free-slip (zero vorticity) boundary condition. Consequently, the best choice of boundary condition may depend on the degree to which the considered boundary steps reflect numerical artifacts versus real topographic features. In realistic configurations, it is thus expected that ideal boundary conditions should vary with location.

Appendix A: Numerical Parameters

In the AM98 configuration, the initial state is at rest with the thickness of the active layer uniformly equal to $h_0 = 500$ m. Density is $\rho_0 = 1,000$ kg m⁻³ and reduced gravity $g' = 0.02$ m s⁻². The Coriolis parameter evolves on a beta-plane $f(y) = f_0 + \beta y$ where $f_0 = 0.5 \times 10^{-4}$ s⁻¹ and $\beta = 2 \times 10^{-11}$ m s⁻¹ so that the internal radius of deformation $R = \sqrt{g'h_0/f}$ is about 45 km at the mid-basin. Zonal wind stress is $\tau = -\tau_0 \cos(\pi y/L)$ with $\tau_0 = 0.2$ N m⁻². Uniform friction parameters are considered with $r = 10^{-7}$ s⁻¹ the bottom linear friction and $\nu = 500$ m² s⁻¹ the lateral viscosity. Uniform mesh resolution ($\Delta x = \Delta y$) and associated time-step for the AM98 configuration are summarized in Table A1. The Asselin filter parameter of the Leap Frog Robert-Asselin time-stepping scheme is $\epsilon = 10^{-1}$. In vector-form, gradient of kinetic energy is discretized with a second order centered scheme. In flux form, advection is also discretized with a second order centered scheme while the Coriolis term is discretized with the ENS scheme.

In the single vortex configuration of Deremble et al. (2016), the initial conditions are a flat sea surface and a vortex of negative vorticity placed next to the wall. In the relative frame of reference centered on the vortex, the initial horizontal speeds are given by the azimuthal profile v_θ (Lamb-Oseen vortex):

$$v_\theta(r) = \frac{\Gamma}{2\pi r} \left(1 - \exp\left(-\frac{r^2}{2r_0^2}\right) \right), \quad (\text{A1})$$

with the pseudoradius $r_0 = 20$ km and the strength of the vortex $\Gamma = -5 \times 10^4$ m² s⁻¹. The model is barotropic with gravity $g = 9.81$ m s⁻² and the basin is 1 m deep. There is no wind forcing nor bottom friction. Coriolis effects are not considered ($f = 0$ throughout the basin). Small lateral dissipation is added to ensure numerical stability: viscosity $\nu = 20$ m² s⁻¹. Simulations are ran over 45 days with an uniform spatial resolution of $\Delta x = \Delta y = 1.25$ km and a time-step of 90 s.

Table A1
Grid-Size and Time-Step Used in Discretization for AM98's Configuration

Resolution	1/4°	1/8°	1/16°	1/32°	1/48°
Grid-spacing	25 km	12.5 km	6.25 km	3.125 km	~2.1 km
Time-step	30 min	15 min	7.5 min	3 min	1.5 min

Appendix B: Formulation of the Discrete Vorticity Schemes Used in Vector-Invariant Form Simulations

The discrete vorticity schemes considered in this study are defined on the Arakawa C-grid. The grid is staggered so that total vorticity $\zeta_{i,j} + f_{i,j}$, horizontal velocities ($u_{i,j}$; $v_{i,j}$) and height $h_{i,j}$ variables are arranged as shown in Figure B1a. The total potential vorticity $q = \frac{(\zeta + f)}{h_f}$ is needed for vector-invariant form advection so layer thickness at F-nodes h_f is deduced from the height h nodes: $h_f = \frac{\bar{h}^{i,j}}{2}$; while vorticity is diagnosed as follows:

$$\zeta_{i,j} = \frac{1}{e_1 e_2 f} (\delta_i [e_{2v} v] - \delta_j [e_{1u} u]), \quad (\text{B1})$$

where $(^{-i}, ^{-j})$ and (δ_i, δ_j) are the averaging and differencing operators at the mid point, for example, $\bar{h}^i = \frac{1}{2}(h_{i,j} + h_{i+1,j})$ and $\delta_i v = v_{i+1,j} - v_{i,j}$. The horizontal scale factors e_{1u} , e_{1v} , e_{2u} , and e_{2v} are derived analytically at each node from the latitudinal (longitudinal) coordinate; on a uniform regular mesh, they are all equal to $\Delta x = \Delta y$.

Figure B1b–B1d represents the discretization at $u_{i,j}$ nodes (blue disks) and illustrates the size of the stencil for each scheme. First, the potential enstrophy conserving scheme (Figure B1b) (Sadourny, 1975) provides a global conservation of global enstrophy $\int h_f q^2$ for non-divergent flow. For x and y components of the vorticity term, it writes as:

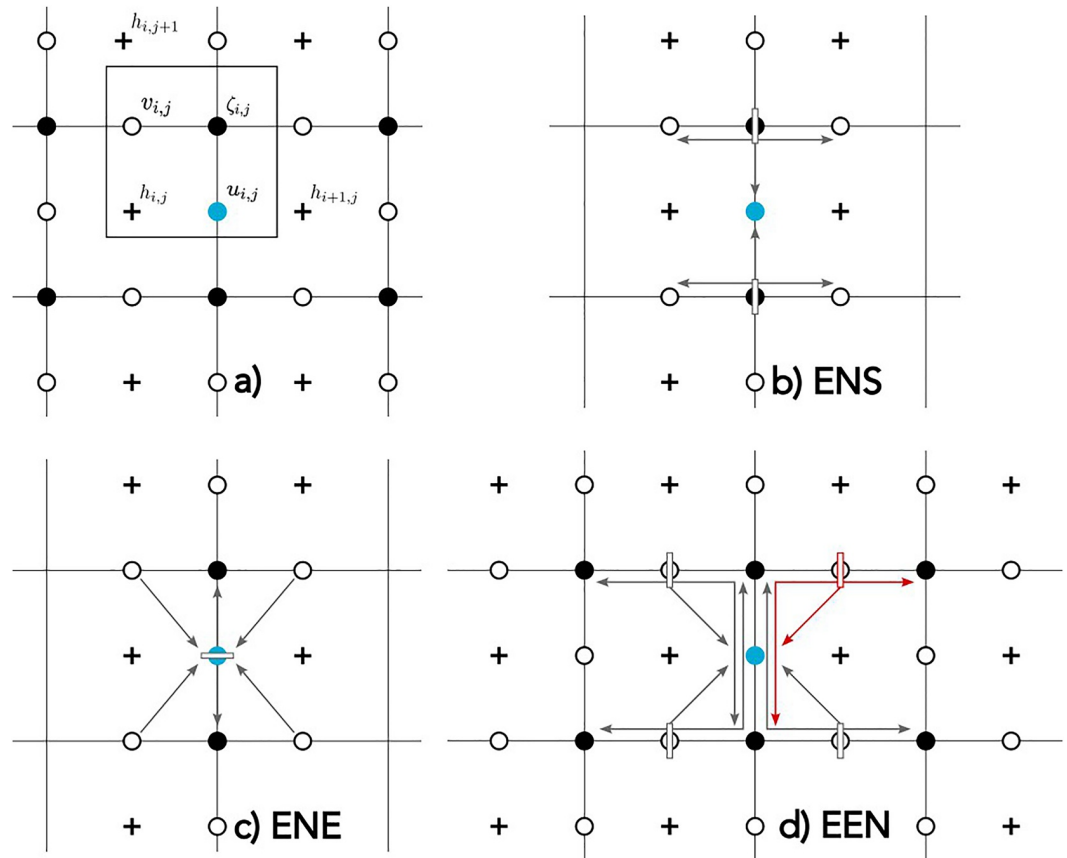


Figure B1. Discrete vorticity schemes on the Arakawa C-grid. (a) Location and indexing of height h nodes (black crosses), horizontal velocity u and v nodes (black circles) and vorticity ζ nodes (black disks) on a single cell. Panels (b–d) illustrate respectively the ENS, ENE, and EEN discretization of vorticity in vector-invariant form. Single arrows (in gray) add themselves; double arrows represent two-point averaging; right-angle cornered arrows symbolize triads Q_m^j ; and rectangles (gray edged) is the factoring of the averaged quantities with the local variables.

$$+ \frac{1}{e_{1u}} \bar{q}^j \bar{V}^{i,j} \quad (\text{B2})$$

$$- \frac{1}{e_{2v}} \bar{q}^i \bar{U}^{i,j}, \quad (\text{B3})$$

where (U ; V) are the transports across cell faces, for example, $V = e_{1v} h_v v$. Then, the kinetic energy conserving (ENE) vorticity scheme (Figure B1c) (Sadourny, 1975) is defined as:

$$+ \frac{1}{e_{1u}} q \bar{V}^j \quad (\text{B4})$$

$$- \frac{1}{e_{2v}} q \bar{U}^j. \quad (\text{B5})$$

Finally, the EEN scheme developed by Sadourny (Burridge & Haseler, 1977) is a member of the family of vorticity schemes derived by Arakawa and Lamb (1981) that conserves kinetic energy and, provided there is no divergence in the flow, potential enstrophy. This scheme relies upon averaging triads of vorticity ${}^i Q_m^l$ that ultimately widen the stencil up to 17 velocity nodes; instead of 7 in the ENS or ENE schemes as they use a much cheaper two-point averaging. A triad ${}^i Q_m^l$ is defined as:

$${}^i Q_m^l = \frac{1}{12} \left(q_{j-1/2+m}^{i-1/2-l} + q_{j-1/2+l}^{i-1/2+m} + q_{j-1/2-m}^{i-1/2+l} \right), \quad (\text{B6})$$

with $(l, m) \in I^2$ where $I = (1/2; -1/2)$. Each triad combines with the adjacent transport V_j^i , for example, V_j^{i+1} multiplies with ${}^{i+1} Q_{1/2}^{-1/2}$ (in red in Figure B1d). Expressions for EEN scheme summarize as

$$+ \frac{1}{e_{1u}} \sum_{l,m \in I^2} {}^{i+1/2-l} Q_m^l V_{j-1/2+m}^{i+1/2-l} \quad (\text{B7})$$

$$- \frac{1}{e_{2v}} \sum_{l,m \in I^2} {}^i Q_m^l U_{j+1/2-m}^{i-1/2+l}. \quad (\text{B8})$$

Data Availability Statement

NEMO code is available at <https://forge.nemo-ocean.eu/nemo/nemo>. The described version is 4.2. The configurations are available at <https://doi.org/10.5281/zenodo.7480139> and the plotting scripts are available at <https://doi.org/10.5281/zenodo.7480159>.

Acknowledgments

We thank Sibylle Techene for her technical support and for performing extra simulations with the third order Runge-Kutta time-stepping scheme. We also thank David Marshall and two anonymous reviewers for comments that helped improving the manuscript. This work was granted access to the HPC resources of IDRIS under the allocation 2021-A0100107451 made by GENCI. This study was carried out as part of the project 18CP03 (Analyse numérique pour la modélisation de la dynamique océanique à fines échelles) under the auspices of French Ministry of Defense/DGA, by Shom and l'INRIA.

References

- Adcroft, A., & Marshall, D. (1998). How slippery are piecewise-constant coastlines in numerical ocean models? *Tellus A: Dynamic Meteorology and Oceanography*, 50(1), 95–108. <https://doi.org/10.3402/tellusa.v50i1.14514>
- Anson, I. J., & Lutjeharms, J. R. E. (2005). Direct observations of eddy turbulence at a ridge in the Southern Ocean. *Geophysical Research Letters*, 32(14), 123–127. <https://doi.org/10.1029/2005GL022588>
- Arakawa, A., & Lamb, V. R. (1981). A potential enstrophy and energy conserving scheme for the shallow water equations. *Monthly Weather Review*, 109(1), 18–36. [https://doi.org/10.1175/1520-0493\(1981\)109<0018:APEAEC>2.0.CO;2](https://doi.org/10.1175/1520-0493(1981)109<0018:APEAEC>2.0.CO;2)
- Bleck, R., & Boudra, D. (1986). Wind-driven spin-up in eddy-resolving ocean models formulated in isopycnic and isobaric coordinates. *Journal of Geophysical Research*, 91(C6), 7611–7621. <https://doi.org/10.1029/JC091iC06p07611>
- Burridge, D., & Haseler, J. (1977). A model for medium range weather forecasting. In *Tech. Rep. No.4, ECMWF*.
- Causon, D. M., Ingram, D. M., Mingham, C. G., Yang, G., & Pearson, R. V. (2000). Calculation of shallow water flows using a Cartesian cut cell approach. *Advances in Water Resources*, 23(5), 545–562. [https://doi.org/10.1016/S0309-1708\(99\)00036-6](https://doi.org/10.1016/S0309-1708(99)00036-6)
- Cessi, P. (1991). Laminar separation of colliding western boundary currents. *Journal of Marine Research*, 49(4), 697–717. <https://doi.org/10.1357/002224091784995738>
- Dengg, J. (1993). The problem of Gulf Stream separation: A barotropic approach. *Journal of Physical Oceanography*, 23(10), 2182–2200. [https://doi.org/10.1175/1520-0485\(1993\)023<2182:TPOGSS>2.0.CO;2](https://doi.org/10.1175/1520-0485(1993)023<2182:TPOGSS>2.0.CO;2)
- Deremble, B., Dewar, W. K., & Chassignet, E. P. (2016). Vorticity dynamics near sharp topographic features. *Journal of Marine Research*, 74(6), 249–276. <https://doi.org/10.1357/002224016821744142>
- Deremble, B., Hogg, A. M., Berloff, P., & Dewar, W. K. (2011). On the application of no-slip lateral boundary conditions to ‘coarsely’ resolved ocean models. *Ocean Modelling*, 39(3), 411–415. <https://doi.org/10.1016/j.ocemod.2011.05.002>

- Dupont, F., & Straub, D. N. (2004). Effect of a wavy wall on the single gyre Munk problem. *Tellus A: Dynamic Meteorology and Oceanography*, 56(4), 387–399. <https://doi.org/10.3402/tellusa.v56i4.14422>
- Dupont, F., Straub, D. N., & Lin, C. A. (2003). Influence of a step-like coastline on the basin scale vorticity budget of mid-latitude gyre models. *Tellus A: Dynamic Meteorology and Oceanography*, 55(3), 255–272. <https://doi.org/10.3402/tellusa.v55i3.12094>
- Ezer, T. (2016). Revisiting the problem of the Gulf Stream separation: On the representation of topography in ocean models with different types of vertical grids. *Ocean Modelling*, 104, 15–27. <https://doi.org/10.1016/j.ocemod.2016.05.008>
- Gent, P. R. (1993). The energetically consistent shallow-water equations. *Journal of the Atmospheric Sciences*, 50(9), 1323–1325. [https://doi.org/10.1175/1520-0469\(1993\)050<1323:TECSWE>2.0.CO;2](https://doi.org/10.1175/1520-0469(1993)050<1323:TECSWE>2.0.CO;2)
- Griffies, S. M., & Hallberg, R. W. (2000). Biharmonic friction with a Smagorinsky-like viscosity for use in large-scale eddy-permitting ocean models. *Monthly Weather Review*, 128(8), 12–2946. [https://doi.org/10.1175/1520-0493\(2000\)128<2935:bfwasl>2.0.co;2](https://doi.org/10.1175/1520-0493(2000)128<2935:bfwasl>2.0.co;2)
- Griffiths, S. D. (2013). Kelvin wave propagation along straight boundaries in C-grid finite-difference models. *Journal of Computational Physics*, 255, 639–659. <https://doi.org/10.1016/j.jcp.2013.08.040>
- Hallberg, R. (2013). Using a resolution function to regulate parameterizations of oceanic mesoscale eddy effects. *Ocean Modelling*, 72, 92–103. <https://doi.org/10.1016/j.ocemod.2013.08.007>
- Holland, W. R., & Haidvogel, D. B. (1981). On the vacillation of an unstable Baroclinic wave field in an eddy-resolving model of the oceanic general circulation. *Journal of Physical Oceanography*, 11(4), 557–568. [https://doi.org/10.1175/1520-0485\(1981\)011<0557:OTVOAU>2.0.CO;2](https://doi.org/10.1175/1520-0485(1981)011<0557:OTVOAU>2.0.CO;2)
- Ketefian, G. S., & Jacobson, M. Z. (2011). A mass, energy, vorticity, and potential enstrophy conserving lateral boundary scheme for the shallow water equations using piecewise linear boundary approximations. *Journal of Computational Physics*, 230(8), 2751–2793. <https://doi.org/10.1016/j.jcp.2010.11.008>
- Kirkpatrick, M. P., Armfield, S. W., & Kent, J. H. (2003). A representation of curved boundaries for the solution of the Navier–Stokes equations on a staggered three-dimensional Cartesian grid. *Journal of Computational Physics*, 184(1), 1–36. [https://doi.org/10.1016/S0021-9991\(02\)00013-X](https://doi.org/10.1016/S0021-9991(02)00013-X)
- Leclair, M., & Madec, G. (2009). A conservative leapfrog time stepping method. *Ocean Modelling*, 30(2), 88–94. <https://doi.org/10.1016/j.ocemod.2009.06.006>
- Madec, G., & NEMO System Team. (2022). NEMO ocean engine. *Zenodo*. <https://doi.org/10.5281/zenodo.6334656>
- Madec, G., Delecluse, P., Crepon, M., & Chartier, M. (1991). A three-dimensional numerical study of deep-water formation in the north-western Mediterranean Sea. *Journal of Physical Oceanography*, 21(9), 1349–1371. [https://doi.org/10.1175/1520-0485\(1991\)021<1349:ATDNSO>2.0.CO;2](https://doi.org/10.1175/1520-0485(1991)021<1349:ATDNSO>2.0.CO;2)
- Magaldi, M. G., Özgökmen, T. M., Griffa, A., Chassignet, E. P., Iskandarani, M., & Peters, H. (2008). Turbulent flow regimes behind a coastal cape in a stratified and rotating environment. *Ocean Modelling*, 25(1), 65–82. <https://doi.org/10.1016/j.ocemod.2008.06.006>
- Penduff, T., Le Sommer, J., Barnier, B., Treguier, A.-M., Molines, J.-M., & Madec, G. (2007). Influence of numerical schemes on current-topography interactions in 1/4° global ocean simulations. *Ocean Science*, 3(4), 509–524. <https://doi.org/10.5194/os-3-509-2007>
- Richardson, S. (1973). On the no-slip boundary condition. *Journal of Fluid Mechanics*, 59(4), 707–719. <https://doi.org/10.1017/S0022112073001801>
- Sadourny, R. (1975). The dynamics of finite-difference models of the shallow-water equations. *Journal of the Atmospheric Sciences*, 32(4), 680–689. [https://doi.org/10.1175/1520-0469\(1975\)032<0680:TDOFDM>2.0.CO;2](https://doi.org/10.1175/1520-0469(1975)032<0680:TDOFDM>2.0.CO;2)
- Shchepetkin, A. F., & O'Brien, J. J. (1996). A physically consistent formulation of lateral friction in shallow-water equation ocean models. *Monthly Weather Review*, 124(6), 1285–1300. [https://doi.org/10.1175/1520-0493\(1996\)124<1285:APCFOL>2.0.CO;2](https://doi.org/10.1175/1520-0493(1996)124<1285:APCFOL>2.0.CO;2)
- Verron, J., & Blayo, E. (1996). The no-slip condition and separation of Western boundary currents. *Journal of Physical Oceanography*, 26(9), 1938–1951. [https://doi.org/10.1175/1520-0485\(1996\)026<1938:TNSCAS>2.0.CO;2](https://doi.org/10.1175/1520-0485(1996)026<1938:TNSCAS>2.0.CO;2)
- Warner, S. J., & MacCready, P. (2009). Dissecting the pressure field in tidal flow past a headland: When is form drag “real”. *Journal of Physical Oceanography*, 39(11), 2971–2984. <https://doi.org/10.1175/2009JPO4173.1>
- Weeks, S. J., Bakun, A., Steinberg, C. R., Brinkman, R., & Hoegh-Guldberg, O. (2010). The Capricorn Eddy: A prominent driver of the ecology and future of the southern Great Barrier Reef. *Coral Reefs*, 29(4), 975–985. <https://doi.org/10.1007/s00338-010-0644-z>

Advection Stability Condition of the Brinkman Volume Penalisation Method

Introduction

Picking the optimal time step when running an ocean model or a climate model is a delicate task. This is partly because constraints on the time step arise from various modelled processes and numerical choices, with potential spatial and temporal dependence, and potential dependence on the exact configuration used. In general, the maximum time step that preserves stability is sought, in order to minimize computational cost. This is why, when introducing new numerical methods, it is desirable to understand the implications on the maximum time step allowed. Here, we investigate stability constraints imposed by a new promising method to represent the land-ocean frontier: the Brinkman Volume Penalisation (BVP) method ([Kevlahan et al., 2015](#)). This method has gained recent interest in the ocean modelling community because of its ability to refine the representation of topography via the introduction of porous (half-land, half-ocean) cells.

[Lemarié et al. \(2012\)](#) analysed three physical processes susceptible to limit the time-step in an ocean climate model: inertial oscillations, internal gravity waves and three-dimensional advection. They show that advection causes the most severe constraint on the time step in a few hot spots of the global ocean. [Kevlahan et al. \(2015\)](#) presented an energetically consistent formulation of BVP that does not tighten the Courant-Friedrichs-Lewy (CFL) constraint related to inertia-gravity waves. However, constraints imposed by advection have not been studied in previous oceanic applications of BVP ([Debreu et al., 2022, 2020](#); [Kevlahan et al., 2015](#)).

In this chapter, we investigate the relationship between the damping effect introduced by the penalisation method and the numerical stability of advection in the context of the BVP method. The chapter begins with a concise overview of the BVP method (Section 1), followed by an examination of the CFL constraints imposed by advection when using the BVP method. We study the direct impact of spreading the penalised region on the model's stability (Section 2). To further enhance our understanding of stability, we assess the Lipschitz condition, which plays a role in the representation of vertical advection (Appendix A). Subsequently, we establish the

minimal criteria that friction within porous cells must meet to ensure the numerical stability of the model in the presence of variable porosity (Section 3). In Section 4, we present a summary of our findings and provide recommendations.

1 The Brinkman Volume Penalisation method

1.1 Retrospective

In the original formulation of [Angot \(1999\)](#); [Angot et al. \(1999\)](#), the blocking effect of the penalised medium was recovered mainly by considering the friction exerted on the flow. [Liu and Vasilyev \(2007\)](#) point out that this formulation is inadequate for representing the perfect reflection of a wave on a solid wall as the reflected wave is damped while a transmitted wave is tolerated. In the framework of compressible flows, these authors formulate a continuity equation that accounts for a porous region so that the jump in porosity acts as a high-impedance medium, causing an incoming wave to totally reflect. This correction is beneficial for general ocean applications where the propagation of gravity waves is a key process for accurate simulations. [Reckinger et al. \(2012\)](#) then developed this treatment for incompressible flows in a rotating shallow water configuration.

However, [Kevlahan et al. \(2015\)](#) pinpointed an inconsistency in the formulation of [Reckinger et al. \(2012\)](#): mass travels at a higher speed than momentum, which prevents energy conservation and affects the numerical stability of the model. [Kevlahan et al. \(2015\)](#) thus present a new conservative formulation of penalisation for incompressible rotating shallow water equations that allows the reflection of gravity waves without the need to use a smaller timestep. Ultimately, this formulation precisely consists of the incompressible shallow water equations governing the physical flow through a porous medium.

In [Debreu et al. \(2020\)](#), the BVP method of [Kevlahan et al. \(2015\)](#) is extended to the three dimensional primitive equations of ocean models, and used to recover sharp bathymetric features in terrain following coordinates while avoiding the pressure gradient errors associated with steep slopes. The same authors thereafter improved their discrete formulation to account for the barotropic–baroclinic mode splitting with a penalised topography ([Debreu et al., 2022](#)). They also reduced the additional computational time to nearly zero, thus showing the potential of the BVP method for long integrations of global ocean models. In this chapter we adopt the formulation of penalised continuous equations presented by [Debreu et al. \(2022\)](#).

1.2 Effective volume and permeable medium

Throughout this chapter, we denote the three-dimensional position vector as $\mathbf{x} = (x, y, z)$, where x and y represent the two horizontal spatial directions, and z is the vertical coordinate aligned with gravity. In the context of the BVP method, we introduce two key parameters: the porosity ϕ and the friction σ .

Porosity ϕ indicates how much liquid is held in a porous cell and is defined as the fraction of liquid volume to the geometric volume of the cell. In practice, the use of the penalisation is confined near the boundaries where the substitution of the solid body by a porous medium primarily changes the effective volume transported through the domain. In other words, the porosity is analogous to an indicator function of land in such manner that it equals 1 far in the interior ocean and 0 in the solid body. In the vicinity of the boundary, its value is comprised between 1 and 0 and varies smoothly, creating a continuum between the porous land and the ocean interior.

The blocking effect of land induces a natural resistance to the flow, commonly referred to as drag. In the BVP framework, this drag is represented by the friction parameter σ , incorporated into the dynamic equation through an additional term $-\sigma \mathbf{u}$, where \mathbf{u} represents the two-dimensional horizontal velocity vector. Physically, this friction can be expressed as a Darcy's law with $\sigma = \mu \phi(\mathbf{x}) / K(\mathbf{u}, \mathbf{x})$, where μ is the dynamic viscosity, and K is the permeability, indicating the ease of flow through the porous medium. This implies that the friction parameter σ is proportional to the porosity ϕ and inversely proportional to the permeability K of the medium. Permeability is generally low in the porous medium ($\phi < 1$), effectively dampening all velocity fluctuations and approximating a viscous 'no-slip' condition ($\mathbf{u} = 0$) in the solid body (Kevlahan et al., 2015). While the combination of high friction with a linear formulation typically results in the enforcement of a 'no-slip' (Dirichlet) boundary condition (Angot, 1999; Angot et al., 1999; Kevlahan et al., 2015), other studies have presented alternative boundary conditions, such as 'free-slip' (Neumann) or 'partial-slip' (Robin), using different formulations of drag in the dynamical equations (Reckinger et al., 2012; Bensiali et al., 2015). However, for the purposes of this thesis, the porosity ϕ and the friction σ are assumed to be independent, along with a simple linear friction term of the form $-\sigma \mathbf{u}$.

In essence, the application of the BVP method involves combining a very low porosity $\phi \ll 1$ with a high friction σ in the porous region, effectively mimicking a solid domain and approximating the behavior of a rigid boundary. It is important to note that the magnitude of the friction parameter σ does not directly represent the physical dissipation exerted by the topography or the porous medium, but rather serves as an arbitrary quantity that allows for control over the accuracy of the desired boundary condition, as explained by Vasilyev and Kevlahan (2002). This characteristic sets the BVP method apart from other penalisation techniques.

Following (Debreu et al., 2022, 2020), the penalised primitive equations read in the absence of forcing and diffusion:

$$\partial_t(\tilde{h}u) + \partial_x(\tilde{h}u^2) + \partial_y(\tilde{h}vu) + h\partial_z(\phi wu) = \frac{\tilde{h}}{\rho_0} \partial_x P|_z - \sigma \tilde{h}u \quad (\text{II.1a})$$

$$\partial_t(\tilde{h}v) + \partial_x(\tilde{h}uv) + \partial_y(\tilde{h}v^2) + h\partial_z(\phi wv) = \frac{\tilde{h}}{\rho_0} \partial_y P|_z - \sigma \tilde{h}v \quad (\text{II.1b})$$

$$\partial_t \tilde{h} + \partial_x(\tilde{h}u) + \partial_y(\tilde{h}v) + h\partial_z(\phi w) = 0 \quad (\text{II.1c})$$

$$\partial_z P = -\rho g \quad (\text{II.1d})$$

with (u, v, w) the three dimensional velocity vector where w is the velocity across model levels, $h = \partial z / \partial k$ represents the layer thickness where k is the index of the vertical coordinate, $\tilde{h} = \phi h$ the penalised layer thickness, P the hydrostatic pressure, ρ the density and ρ_0 a reference density.

It is straightforward to see that the penalised primitive equations converge to the classical equations without penalisation in the interior ocean. However, in the proximity of the boundary, the flow dynamics are significantly influenced by the Brinkman Volume Penalisation method, which introduces reduced transport and deceleration, effectively approximating the impact of topography on the system.

At a discrete level, the accuracy and numerical stability of the Brinkman Volume Penalisation method relies on setting finely the penalty parameters. In the subsequent analysis, we explore the stability constraints that arise from advection when implementing the BVP method. Our objective is to determine a practical range of application that maintains the numerical stability of the method.

2 Courant number stability analysis

Satisfying the CFL condition is the first requirement when running a numerical model to avoid numerical instabilities. This condition requires the advective Courant number to remain inferior to a threshold, which depends on the chosen time-space discretisation (Lemarié et al., 2015). In practice, this entails choosing an adequate time step and grid cell size given the physical velocity solved. As shown in section 1.2, introduction of a porosity parameter changes the effective volume carried by the advective fluxes. Sharp variations in this parameter can induce strong grid-scale variations in the penalised fluxes that impact the Courant number of advection, and that may thus jeopardise numerical stability.

Table II.1: Location of grid-nodes for a single cell. Indices (i, j, k) are co-aligned along (x, y, z) directions.

T	i	j	k
U	$i + 1/2$	j	k
V	i	$j + 1/2$	k
W	i	j	$k + 1/2$
F	$i + 1/2$	$j + 1/2$	k

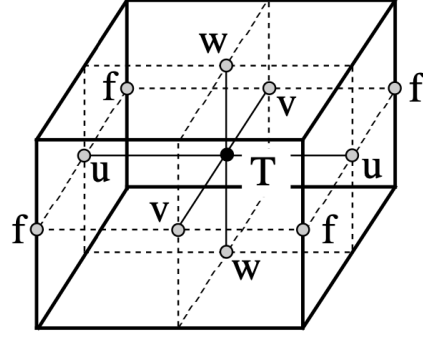


Figure II.1: The Arakawa C grid. Location of T nodes (black circle) and (u,v,w,f) nodes (grey circles) on a single unit cell. This figure is derived from (Madec & NEMO System Team, 2022).

Here, we establish the classical CFL condition for advection in the penalised regions. We focus the stability analysis primarily on the porosity effects, since we anticipate that the friction term has a stabilising effect by slowing the motion in the penalised region. The purpose of this section is to describe the impact of a varying porosity on the CFL stability condition. The effects of smoothing the porosity field will be discussed in regard to the numerical stability of the method.

2.1 Advection stability conditions of the penalisation

The standard approach for an analysis of advective stability is to write the Courant numbers in a finite-volume sense to be consistent with the discretisation schemes used in numerical models. In many OGCMs such as the NEMO model (Madec & NEMO System Team, 2022), the physical variables are arranged on the Arakawa “C” grid (Arakawa & Lamb, 1977) with tracers T in the center of the cells, horizontal velocities (u, v) at the lateral faces (centered in the vertical), vertical velocity w centered at the bottom and top faces of the box and vorticity F placed at the corners (centered in the vertical), as arranged in Figure II.1. Location of grid-points are written as a function of integer or integer and a half value of the column (Table II.1). Space factors Δx , Δy or Δz define the distance between two nodes in the (x, y, z) directions respectively. Following these notations, the effective (‘penalised’) volume of the discretised cell $\tilde{V}_{i,j,k} = \phi(\mathbf{x}_{i,j,k})(\Delta x \Delta y \Delta z)_{i,j,k}$. Similarly, the discrete effective volume flux $(\tilde{U}, \tilde{V}, \tilde{W})$ are defined in each direction as

$$\tilde{U}_{i+1/2,j,k} = \phi(\mathbf{x}_{i+1/2,j,k})U_{i+1/2,j,k} = \phi(\mathbf{x}_{i+1/2,j,k})(\Delta y \Delta z)_{i+1/2,j,k} u_{i+1/2,j,k} \quad (\text{II.2a})$$

$$\tilde{V}_{i,j+1/2,k} = \phi(\mathbf{x}_{i,j+1/2,k})V_{i,j+1/2,k} = \phi(\mathbf{x}_{i,j+1/2,k})(\Delta x \Delta z)_{i,j+1/2,k} v_{i,j+1/2,k} \quad (\text{II.2b})$$

$$\tilde{W}_{i,j,k+1/2} = \phi(\mathbf{x}_{i,j,k+1/2})W_{i,j,k+1/2} = \phi(\mathbf{x}_{i,j,k+1/2})(\Delta x \Delta y)_{i,j,k+1/2} w_{i,j,k+1/2} \quad (\text{II.2c})$$

Consider the purely advective equation in the absence of forcing and dissipation along with the incompressibility equation written in the conservative way on a fixed-time coordinate.

$$\partial_t(\tilde{h}q) + \partial_x(\tilde{h}uq) + \partial_y(\tilde{h}vq) + h\partial_z(\phi wq) = 0 \quad (\text{II.3a})$$

$$\partial_x(\tilde{h}u) + \partial_y(\tilde{h}v) + h\partial_z(\phi w) = 0 \quad (\text{II.3b})$$

q can represent either a tracer or horizontal momentum (when a flux form of the nonlinear term is used).

Following (Shchepetkin, 2015), the Courant numbers for forward in time, upstream finite-volume discretisation of tracer advection, $\tilde{\alpha}_x$ in the x-horizontal direction and $\tilde{\alpha}_y$ in the y-horizontal direction, are given by

$$(\tilde{\alpha}_x)_{i,j,k} = \frac{\Delta t}{\tilde{V}_{i,j,k}} [\max(\tilde{U}_{i+1/2,j,k}, 0) - \min(\tilde{U}_{i-1/2,j,k}, 0)] \quad (\text{II.4a})$$

$$(\tilde{\alpha}_y)_{i,j,k} = \frac{\Delta t}{\tilde{V}_{i,j,k}} [\max(\tilde{V}_{i,j+1/2,k}, 0) - \min(\tilde{V}_{i,j-1/2,k}, 0)] \quad (\text{II.4b})$$

and the vertical one by

$$(\tilde{\alpha}_z)_{i,j,k} = \frac{\Delta t}{\tilde{V}_{i,j,k}} [\max(\tilde{W}_{i,j,k-1/2}, 0) - \min(\tilde{W}_{i,j,k+1/2}, 0)] \quad (\text{II.5a})$$

These numbers are positive definite and they can be easily interpreted as the fractions of the volume flowing out through each direction to the total volume of the cell, during one time step Δt . The CFL stability condition due to three dimensional advection reads

$$\tilde{\alpha}_x + \tilde{\alpha}_y + \beta \tilde{\alpha}_z \leq \alpha_t^* \quad (\text{II.6})$$

with α_t^* the advective CFL criterion for tracer advection, and β a coefficient arising from the fact that different advection schemes with different stability criteria may be used in the horizontal and vertical advection (Lemarié et al., 2015). It is straightforward to see that adhering to the CFL condition necessitates maintaining the proportion of the volume replaced during one time step below α_t^* to prevent numerical model failure. As an example, $[\tilde{\alpha}_x + \tilde{\alpha}_y + \tilde{\alpha}_z] > 1$ corresponds to the situation when a forward-in-time, first-order upstream scheme loses its positive-definiteness property and becomes numerically unstable. The consideration of other time-space discretisation schemes would affect the values of α_t^* and β but not the definition of the Courant numbers, which makes the chosen approach versatile as shown in Lemarié et al. (2012).

Similar Courant numbers can be defined for the advection of momentum in both horizontal directions. Taking the example of the x (zonal) direction, it suffices to replace q by u in the advection equation and to consider the zonally averaged fluxes over the U node, to be consistent with the discretisation schemes used in numerical models. The fraction of momentum replaced during one time step in each direction is thus given by

$$(\tilde{\alpha}_{ux})_{i+1/2,j,k} = \frac{\Delta t}{\tilde{\mathcal{V}}_{i+1/2,j,k}} [\max(\overline{\tilde{U}}_{i+1,j,k}, 0) - \min(\overline{\tilde{U}}_{i,j,k}, 0)] \quad (\text{II.7a})$$

$$(\tilde{\alpha}_{uy})_{i+1/2,j,k} = \frac{\Delta t}{\tilde{\mathcal{V}}_{i+1/2,j,k}} [\max(\overline{\tilde{V}}_{i+1/2,j+1/2,k}, 0) - \min(\overline{\tilde{V}}_{i+1/2,j-1/2,k}, 0)] \quad (\text{II.7b})$$

$$(\tilde{\alpha}_{uz})_{i+1/2,j,k} = \frac{\Delta t}{\tilde{\mathcal{V}}_{i+1/2,j,k}} [\max(\overline{\tilde{W}}_{i+1/2,j,k+1/2}, 0) - \min(\overline{\tilde{W}}_{i+1/2,j,k-1/2}, 0)] \quad (\text{II.7c})$$

The overbar denotes an average over the x -direction at the center $i + 1/2$ of the cell $\tilde{\mathcal{V}}_{i+1/2,j,k}$, e.g. for a variable ψ , $\overline{\psi} = \frac{1}{2}(\psi_{i-1/2} + \psi_{i+1/2})$. The CFL stability condition for u-momentum advection then reads

$$\tilde{\alpha}_{ux} + \tilde{\alpha}_{uy} + \beta \tilde{\alpha}_{uz} \leq \alpha_u^* \quad (\text{II.8})$$

where α_u^* is the advective CFL stability criterion for momentum advection.

Small vertical Courant numbers are almost guaranteed when the adaptive, Courant number-dependent treatment of vertical velocity (Shchepetkin, 2015) is used in the simulations. The latter treatment extends the range of stability of vertical advection by solving implicitly a fraction of the vertical velocities which, if explicitly integrated with the same time step, would generate excessive vertical Courant numbers. Since the method employs a first-order upstream approach for spatial derivatives, it introduces more diffusion compared to traditional spatial schemes for vertical advection. To minimise the additional diffusion associated with this approach, the method is wisely designed to activate only when and where necessary (hence its application is restricted in both space and time). Given that the proportion of the vertical velocity solved implicitly is determined in regard to the evaluation of the three-dimensional CFL condition, our focus also lies in maintaining low horizontal Courant numbers in order to avoid introducing artificial diffusion in the penalised region.

However, the method proposed by (Shchepetkin, 2015) involves inverting a system of equations, which could potentially be singular. This aspect is overlooked in their study, and we question whether the BVP method could lead to a non-invertible system? To explore this scenario, we establish in Appendix A the so-called Lipschitz condition resorting to the BVP method that vertical advection needs to adhere to prevent numerical failure. Nonetheless, sensitivity tests

show that numerical instabilities are likely to arise from breaking the CFL number due to excessive horizontal velocities rather than from breaking the Lipschitz condition (not shown), thereby justifying our study.

2.2 Numerical constraint induced by a sharp interface

Significant differences in face areas and capacities within the mesh can jeopardize the numerical stability of the model. The introduction of porosity, along with penalisation, leads to numerical stability challenges in some specific areas of the domain. These 'hot spots' arise at the sharp transition region where the ocean interfaces with the penalised (i.e., land) region.

Let us consider a numerical cell intersected by different topographic slopes, as depicted in Figure II.2. When the slope cuts the cell in half (Figure II.2a), the liquid portion of the cell accounts for half of the total volume, leading to a cell porosity, or volume porosity, $\phi_t = 0.5$. Adjacent to the ocean region (depicted in white), with a porosity of $\phi_t = 1$, the two domains are connected through the shared face of the cell. It is common practice (discussed in next section) to define the face porosities ϕ_u by averaging the porosity values ϕ_t of the two adjacent cells, resulting in $\phi_u = \overline{\phi_t}$, which gives $\phi_u = 0.75$ in the case of Figure II.2a.

As the slope becomes steeper (Figure II.2b), the capacity of the cell ϕ_t becomes more compact, while the surface area ϕ_u reduces more gradually. In the extreme case of a vertical wall (Figure II.2c), the cell is almost empty (ϕ_t close to zero), while ϕ_u approaches half the face area. This situation creates a critical stability issue when the volume leaving the cell greatly exceeds its capacity.

Consider the extreme scenario depicted in Figure II.2c, where transport is directed toward the ocean region. The effective volume flowing through the eastern face of the first porous cell can be relatively large ($\phi_u \approx 0.5$) despite the small capacity of the cell ($\phi_t = 0.01$). Consequently, for a given time step and resolution, the maximum allowable speed in the Courant number equation (Eq. II.4a) is approximately 50 times smaller than in the absence of penalisation. A similar issue can arise in any direction, for both tracer and momentum advection.

In order to establish the connection between the Courant numbers and the porosity values ϕ , we rewrite the Courant number defined in equations Eq II.4a as follows:

$$(\tilde{\alpha}_x)_{i,j,k} = \frac{\Delta t}{(\phi_t \mathcal{V})_{i,j,k}} \left[\max((\phi_u U)_{i+1/2,j,k}, 0) - \min((\phi_u U)_{i-1/2,j,k}, 0) \right] \quad (\text{II.9a})$$

For a fixed time-space resolution, the Courant number $(\tilde{\alpha}_x)_{i,j,k}$ (Eq II.9a) primarily depends on the cell capacity ϕ_t and its surface areas $(\phi_u)_{i+1/2}$ and $(\phi_u)_{i-1/2}$. Assuming that the orientation of the currents varies across more than one cell, the most critical case for stability occurs where the ratio ϕ_u/ϕ_t is the largest. To assess the impact of volume penalisation on the horizontal CFL

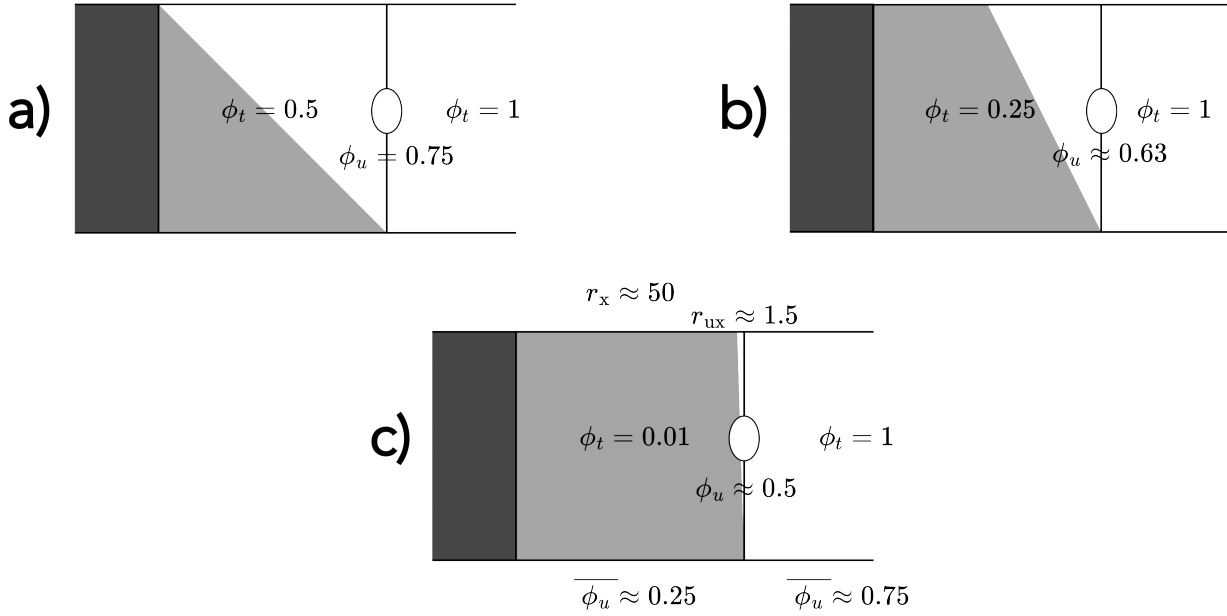


Figure II.2: Schematic illustration depicting the representation of a steep topographic slope intersecting a numerical cell. The cells are cut based on the steepness of the slope, with the ocean domain colored in white and the land (porous) region in grey. Cells that are fully land, indicating complete masking, are shaded in black. Each case shows the surface porosity values ϕ_u , which are defined as the average of the two adjacent volume porosities ϕ_t . Panel (a) and (b) depict slopes with aspect ratios of $\Delta z/\Delta x$ and $2\Delta z/\Delta x$ respectively. In panel (c), the extreme case of a vertical wall is presented, with a slope of aspect ratio $100\Delta z/\Delta x$, resulting in an almost empty cell. In this case, $\overline{\phi_u}$ is shown to demonstrate how the sensitivity factors r_x and r_{ux} are computed.

conditions, we introduce the factors r_x and r_{ux} , which quantify the change in the CFL condition resulting from the introduction of penalisation:

$$(r_x)_i = \frac{\max((\phi_u)_{i+1/2}, (\phi_u)_{i-1/2})}{(\phi_t)_i} \quad (\text{II.10a})$$

$$(r_{ux})_{i+1/2} = \frac{\max(\overline{(\phi_u)}^{i+1}, \overline{(\phi_u)}^i)}{(\phi_u)_{i+1/2}} \quad (\text{II.10b})$$

These factors provide insight into the grid-scale porosity variations and their influence on numerical stability. Specifically, when considering a sharp interface with a small volume porosity value ϕ_{\min} , the expressions for r_x and r_{ux} become:

$$(r_x)_i = \frac{1 + \phi_{\min}}{2\phi_{\min}} \quad (\text{II.11a})$$

$$(r_{ux})_{i+1/2} = \frac{3 + \phi_{\min}}{2(1 + \phi_{\min})} \quad (\text{II.11b})$$

For very small volumes ($\phi_{\min} \ll 1$) the influence of the penalisation on momentum advection is limited, as r_{ux} ranges between 1 and 3/2. On the contrary, mass advection is prone to greater constraints on the time-step as r_x becomes infinite as $r_x \sim 1/(2\phi_{\min})$ for small ϕ_{\min} . Indeed, fig-

ure II.2c displays the values of r_x and r_{ux} for the extreme case of a vertical wall ($\phi_{\min} = 0.01$), with $r_x \approx 50$ and $r_{ux} \approx 1.5$. This gap between these two numbers suggests that numerical instability is more likely to arise from mass advection rather than momentum advection.

2.3 Geometry realism and its impact on stability

The approach of using a simple two-point average for defining ϕ_u may not accurately represent the geometry depicted in Figure II.2. However, it offers the advantage of providing continuous variations in the height of the water column, which improves the model response to the topography. Upon examining the expressions of r_x and r_{ux} (Eq. II.10), it becomes apparent that there is potential to mitigate the numerical constraints of a sharp interface by modifying the definition of porosity fields on the faces and centers of the cells. Striking the right balance between the realism of the numerical topography and the additional constraint imposed on the model remains an open question. In conjunction with other existing methods in z -coordinate models, we mention different approaches that vary in their realism to investigate the potential applications of the Brinkman Volume Penalisation.

In the 'partial cell' approach (Adcroft et al., 1997), the volume of the last wet cell is modified to account for the actual height of the water column, resulting in a stepped representation of the topography that can lead to excessive spurious mixing in simulations. In the context of the Brinkman Volume Penalisation framework, this approach corresponds to defining $(\phi_u)_{i+1/2} = \min((\phi_t)_{i+1}, (\phi_t)_i)$, which avoids constraints on tracer advection ($r_x = 1$).

The 'thin wall' representation presented by (Bonaventura, 2000; Steppeler, 2002) assigns depths only to the faces of the bottom cells, leaving the centers of the bottom cells unchanged, which is equivalent to setting $\phi_t = 1$. This representation guarantees that r_x is less than unity, enhancing the stability for tracer advection. However, the abrupt changes in depths from the center to the faces of the cell raise concerns regarding the generation of noise in global ocean applications.

Another class of methods is the 'shaved cells' approach (Adcroft et al., 1997), where the volume and surface areas of the bottom cells are geometrically modified based on the position of the slope, resulting in a smooth representation of the bottom by avoiding the creation of artificial steps. For gentle slopes (less than the aspect ratio $\Delta z/\Delta x$), the approach simplifies to setting $\phi_u = \overline{\phi_t}$, as discussed earlier. In the general case, stability is more severely compromised for steeper slopes, as it can generate very small volumes adjacent to large face areas. The constraint exerted on the time step is $r_x \approx 1/\phi_{\min}$.

A more detailed modelling of the topography can be achieved with the 'porous barriers' method presented by Adcroft (2013). This approach introduces thin porous walls to capture fine-scale topographic obstacles. The presented method aligns well with the 'Depth Dependent

Porosity' penalisation method for urban flooding simulations, as presented in [Guinot, Delenne, Rousseau, and Boutron \(2018\)](#). However, direct implications for the stability of the model cannot be deduced from this configuration, except that it lies between the thin wall and shaved cells approximations.

Hence, one significant advantage of defining the face porosity as the two-point average of cell centers is that it ensures the continuity of depths at the velocity nodes with the depths of the water column. Additionally, this approach helps alleviate the numerical constraints by a factor of two compared to the shaved cell representation. With this definition, we now investigate the impact of spreading the penalised interface on the stability of the model.

2.4 Effects on the stability of spreading the interface

In previous studies, the penalised interface is spread across multiple cells to ensure the numerical stability of the model. This is typically achieved by employing a Shapiro filter on the sharp penalised interface ([Debreu et al., 2022, 2020](#)) or by using a hyperbolic tangent function to connect the ocean and land, with the width controlled by an arbitrary parameter ([Kevlahan et al., 2015; Reckinger et al., 2012; Liu & Vasilyev, 2007](#)). These methods offer the advantage of reducing the constraint on the time-step while preserving the physical height of the water column. However, there is currently limited guidance available on determining the appropriate level of filtering that effectively maintains the numerical stability of the method.

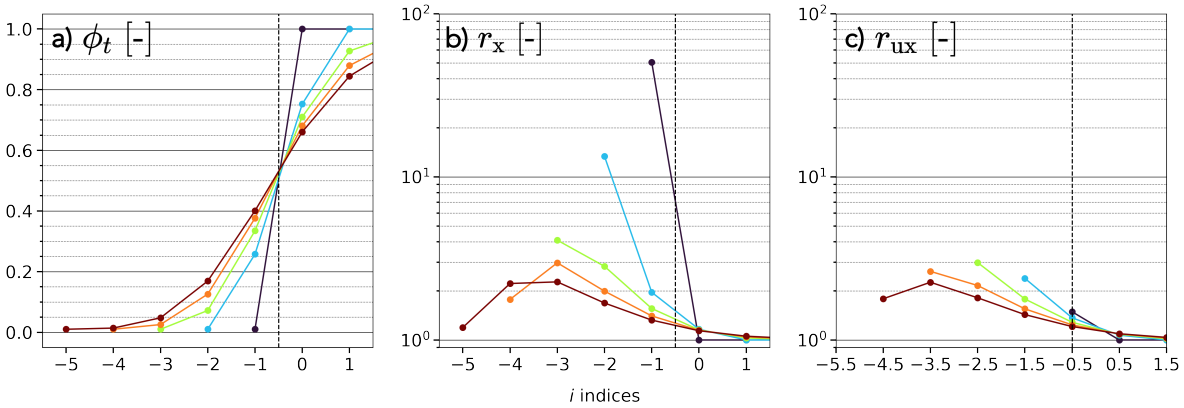


Figure II.3: Factors r_x and r_{ux} with various level of smoothing. Panel (a) shows the porosity field ϕ_t defined at the center of the cells (dots), and porosity ϕ_u defined at faces by averaging over the two adjacent cells (i.e. $\phi_u = \overline{\phi_t}$). The low porosity region has a porosity $\phi_{\min} = 0.01$. Colours indicate the number of passes of a Shapiro filter (1/4, 1/2, 1/4) ([Shapiro, 1970](#)) applied to the porosity field: zero (black), one (blue), two (green), three (orange) or four (red). Panels (b) and (c) show on a y -log scale the factors r_x and r_{ux} , respectively, of the smoothed porosity field.

Figure II.3 shows the effect on r_x and r_{ux} of smoothing the interface in a 1D configuration. We start from a porosity field at cell center ϕ_t defined by a step function (Figure II.3a in black), whose value is $\phi_{\min} = 0.01$ on the left of the interface (indicated by the vertical dotted line) and

1 on the right. T-node porosity (ϕ_t) is plotted at the center of the cells (dots), and velocity-node porosity (ϕ_u) is defined by averaging neighbouring ϕ_t values (hence ϕ_u lies on the lines connecting the dots). Colours, from blue to red, indicate the number of passes of a Shapiro filter applied to the porosity step function.

Let us consider first the constraint on the maximum time step allowed for mass advection (Figure II.3a,b). Before filtering (black curves), the configuration is identical to the case of the vertical wall shown in figure II.2c, resulting in r_x peaking at about 50 at the interface. As the degree of smoothing increases, the profile of the porosity curve possesses a progressively wider transition such that the profile of r_x flattens toward smaller values of the order of the unity. We found that applying two passes of filter (equivalent to having 6 points to solve the interface) suffices to divide by 10 the initial constraint on the time step (green curve in II.3b). Past two passes, the effect of smoothing on r_x is more subtle.

The constraints for the momentum advection react differently to the level of smoothing, as illustrated in Figure II.3c. The maximum value of the factor r_{ux} actually increases from 1.5 to about 3 up to two passes of filtering (green curve in Fig. II.3c), then gently decreases to around 2 (orange and red curves in Fig. II.3c). The latter observation suggests the need to explore alternative methods for spreading the porosity field. The increase of r_{ux} with a few passes of smoothing is unexpected. A plausible strategy to explore the problem further would be to find other methods for spreading the porosity field.

However, the comparison between Figure II.3b and Figure II.3c suggests that mass advection remains the limiting process for the numerical stability of the BVP method. This difference is expected due to the nature of the staggered grid. On a C-grid, the computation of volume fluxes for momentum advection is performed through a two-point average of the adjacent transports, which inherently smooths out velocity fluctuations. As a result, the CFL condition for momentum advection becomes less sensitive to grid-scale variations.

In summary, we show that the CFL constraint imposed by advection is most sensitive to mass advection when using the BVP method. When defining a sharp interface between the low porosity region (ϕ_{\min}) and the ocean interior, the maximum allowable time step must be reduced by a factor of approximately $(2\phi_{\min})^{-1}$. We demonstrate that spreading the interface through successive applications of a Shapiro filter helps to mitigate the constraint on the time step. In fact, two passes of filter achieve most of the mitigation by significantly reducing the impact of the initial porosity jump by a factor of ten. However, even with multiple filtering passes, the maximum allowable time step still needs to be reduced, leading us to consider the incorporation of some drag through penalty friction as a potential solution.

3 Adjusting penalty friction for numerical stability

As topography is spread across the porous region, the physical position of the boundary becomes less clear. Thus, it is an open question with the BVP method where to apply friction in order to choose the position of the blocking barrier. It is unclear whether gradually ramping up friction in the porous region (Debreu et al., 2020, 2022) or increasing it sharply landward of the target boundary (that is, the boundary in the absence of penalisation) (Kevlahan et al., 2015) produces more accurate solutions. Debreu et al. (2022) show that the numerical formulations for the discretisation of friction also have important consequences for the spatial extent of the velocity damping region and the actual extent of the no-slip region.

On the one hand, introducing drag in the porous medium has the potential advantage of damping velocity fluctuations where the numerical advection stability is at risk, thereby preventing the CFL condition to be violated. On the other hand, high levels of friction within the smoothed interface may potentially cause excessive drag of boundary currents. These considerations invite us to look for a minimum friction that guarantees the numerical stability of the model.

3.1 Temporal discretisation of friction

The numerical formulation for the permeability is a delicate problem with strong repercussions on the drag exerted on the simulated flows. The accuracy of the BVP method in the representation of topography is theoretically controlled by the intensity of the friction parameter σ applied in the porous region (Angot, 1999). However, the maximum value allowed in a numerical model is limited because of the stability restriction induced by the discretisation scheme chosen.

Considering only the x -direction, the one-dimensional penalised equation is

$$\partial_t(\tilde{h}u) = \text{RHS} - \sigma\tilde{h}u \quad (\text{II.12})$$

where the right-hand side term RHS gathers any contribution from the potential non-linear, forcing and dissipation terms. In Debreu et al. (2020); Kevlahan et al. (2015), the authors use an explicit method to integrate $-\sigma\tilde{h}u$, given by:

$$(\tilde{h}u)^{n+1} = (1 - \sigma\Delta t)(\tilde{h}u)^n + \Delta t \text{ RHS} \quad (\text{II.13})$$

where n represents the discretised time step. This method is relatively easy to implement, but it requires that the magnitude of σ remains smaller than $1/\Delta t$ for numerical stability. As we intend to develop our method without restriction on the amount of friction represented in the porous region, we look for other discretisation techniques. Following Rasmussen, Cottet, and

Walther (2011), Debreu et al. (2022) explored some potential formulations to implement σ in the dynamic equations and presented three methods based on a time splitting. Their approach consists in solving Eq. II.12 in two steps:

$$\partial_t(\tilde{h}u) = \text{RHS} \quad (\text{II.14a})$$

$$\partial_t(\tilde{h}u) = -\sigma\tilde{h}u \quad (\text{II.14b})$$

Solving II.14a gives an intermediate value $(\tilde{h}u)^{n+1,*} = (\tilde{h}u)^n + \Delta t \text{ RHS}$ for the second step. Debreu et al. (2022) compared explicit, implicit and exponential temporal integration methods for solving II.14b. The three formulations read, respectively for explicit, implicit and exponential integration:

$$(\tilde{h}u)^{n+1} = (1 - \sigma\Delta t)(\tilde{h}u)^{n+1,*} \quad (\text{II.15})$$

$$(\tilde{h}u)^{n+1} = \frac{(\tilde{h}u)^{n+1,*}}{1 + \sigma\Delta t} \quad (\text{II.16})$$

$$(\tilde{h}u)^{n+1} = \exp(-\sigma\Delta t)(\tilde{h}u)^{n+1,*} \quad (\text{II.17})$$

Debreu et al. (2022) then define the friction $\sigma(x)$ that is a simple function of $\phi(x)$. The comparison between equations II.15, II.16, and II.17 reveals that the level of friction introduced in the dynamic equations can vary depending on the integration method employed. Specifically, the authors demonstrate that an explicit method leads to velocity damping over a narrower region compared to an implicit method, resulting in a more slippery porous region.

Instead of precisely controlling the damping in the penalised region, our focus is to introduce the necessary friction that ensures numerical stability for a given porosity profile. Therefore, we prefer an implicit method, without loss of generality. It is important to note that the resulting drag in the interface region may be lower than the actual friction required to approximate a 'no-slip' condition. Furthermore, a plausible strategy to be explored would be to consider the penalty friction in the context of the bottom stress induced by physical bathymetry, as presented in Debreu et al. (2022).

We proceed by determining a value of σ that maintains the horizontal CFL condition in the porous medium. To assess the feasibility of our approach, we initially consider one-dimensional advection. However, the methodology can be extended to the three-dimensional case or restricted to the two horizontal directions, provided an adaptive, Courant number-dependent treatment of vertical velocity (Shchepetkin, 2015) is used during the simulation.

Our guiding principle is to set the friction parameter σ to positive non-zero values when the Courant number in equation II.4a exceeds a safety factor γ .

3.2 Minimal friction criteria

Criterion for tracer advection

The Courant number at iteration $n + 1$ and position x_i is

$$\tilde{\alpha}_x(\tilde{U}^{n+1}) = \frac{\Delta t}{(\phi_t \mathcal{V})_i} \left[\max((\phi_u U^{n+1})_{i+1/2}, 0) - \min((\phi_u U^{n+1})_{i-1/2}, 0) \right]. \quad (\text{II.18})$$

Using \tilde{U}^{n+1} expressed in Eq. (II.16), the Courant number involves the friction of the two adjacent faces of the cell

$$\tilde{\alpha}_x(\tilde{U}^{n+1}) = \frac{\Delta t}{(\phi_t \mathcal{V})_i} \left[\max\left(\left(\frac{\phi_u U^{n+1,*}}{1 + \sigma \Delta t}\right)_{i+1/2}, 0\right) - \min\left(\left(\frac{\phi_u U^{n+1,*}}{1 + \sigma \Delta t}\right)_{i-1/2}, 0\right) \right]. \quad (\text{II.19})$$

Using the fact that each term in the Courant number is positive definite, the number is bounded by

$$\tilde{\alpha}_x(\tilde{U}^{n+1}) \leq \max_{s \in \{i-1/2, i+1/2\}} \left(\frac{1}{1 + \sigma \Delta t} \right)_s \tilde{\alpha}_x(U^{n+1,*}) \quad (\text{II.20})$$

Note that the porosity factor r_x is implicitly taken into account in the right hand side of the inequality. Denoting $(\sigma_0^t)_i = \min(\sigma_{i-1/2}, \sigma_{i+1/2})$, we constraint the upper bound of $\tilde{\alpha}_x(\tilde{U}^{n+1})$ by γ , giving

$$\tilde{\alpha}_x(\tilde{U}^{n+1}) \leq \frac{\tilde{\alpha}_x(\tilde{U}^{n+1,*})}{1 + (\sigma_0^t)_i \Delta t} \leq \gamma \quad (\text{II.21})$$

Thus, the minimum of neighbour frictions must satisfy

$$(\sigma_0^t)_i \geq \frac{1}{\Delta t} \left(\frac{\tilde{\alpha}_x(\tilde{U}^{n+1,*})}{\gamma} - 1 \right) \quad (\text{II.22})$$

to preserve the CFL condition on tracer advection.

Criterion for momentum advection

Since we found that r_{ux} can increase with the degree of smoothing applied to the porosity field, we also establish a minimum criterion on momentum advection. By averaging the volume flux in the x direction, \tilde{U}^{n+1} expressed in II.16, we write the Courant number II.7a as a function of

the neighbouring frictions at the iteration $n + 1$ and position $x_{i+1/2}$:

$$\tilde{\alpha}_{\text{ux}}(\tilde{U}^{n+1}) = \frac{\Delta t}{(\phi_u \mathcal{V}_u)_{i+1/2}} \left[\max \left(\left(\frac{\phi_u U^{n+1,*}}{1 + \sigma \Delta t} \right)_{i+1}, 0 \right) - \min \left(\left(\frac{\phi_u U^{n+1,*}}{1 + \sigma \Delta t} \right)_i, 0 \right) \right] \quad (\text{II.23})$$

Calculations are analogous to the ones detailed above. By introducing $(\sigma_0^u)_{i+1/2} = \min((\sigma_0^t)_i, (\sigma_0^t)_{i+1}) = \min(\sigma_{i-1/2}, \sigma_{i+1/2}, \sigma_{i+3/2})$, we are thus able to express that the minimum of these three adjacent frictions must satisfy

$$(\sigma_0^u)_{i+1/2} \geq \frac{1}{\Delta t} \left(\frac{\tilde{\alpha}_{\text{ux}}(\tilde{U}^{n+1,*})}{\gamma} - 1 \right) \quad (\text{II.24})$$

Synthesis

To preserve the numerical stability for advection, satisfying both criteria [II.22](#) and [II.24](#) is necessary. At each time step, the Courant numbers are calculated with the $\tilde{U}^{n+1,*}$ field for tracer and momentum advection. Then, $\sigma_{i+1/2}$ is evaluated to satisfy both [II.22](#) at i and $i + 1$ nodes and [II.24](#) at $i - 1/2$, $i + 1/2$, and $i + 3/2$ nodes. Additionally, $\sigma_{i+1/2}$ must remain positive to prevent the introduction of anti-friction. An expression for $\sigma_{i+1/2}$ that satisfies all these requirements is

$$\sigma_{i+1/2} = \max((\sigma_0^u)_{i-1/2}, (\sigma_0^t)_i, (\sigma_0^u)_{i+1/2}, (\sigma_0^t)_{i+1}, (\sigma_0^u)_{i+3/2}, 0) \quad (\text{II.25})$$

With this approach, no tuning of the friction σ in the interface region is required, as its magnitude is governed by the porosity ϕ and velocity fluctuations. The introduction of the new parameter γ is not cumbersome as it simply sets the maximum Courant number allowed for a given numerical formulation. The safety factor should be set close the CFL number of a given space-time discretisation. Note that the three-dimensional CFL condition criteria of many space-time discretisation schemes used in ocean models are listed in Table 2 of ([Lemarié et al., 2015](#)).

A more simple approach could be to establish σ on r_x by considering the maximal transport U_{max} admissible without the penalisation. The drawback of this method is that drag may be dispensed too far in the transition region, resulting in a more frictionous bottom. In contrast, the presently suggested approach reduces overall friction in the simulation by adapting at each iteration the friction parameter, while ensuring stability.

Figure [II.3](#) showed that the maximum of r_x or r_{ux} shifts toward the interior of the ocean when more than two passes of Shapiro filter is applied on the porosity field. We caution that this may become problematic for our definition of σ in Eq. [II.25](#) as artificial friction could be

introduced well away from the target topography. A plausible strategy to be explored would be to find the optimal minimum friction that respects simultaneously criteria II.22 and II.24 while also decreasing monotonically away from the low porosity region.

4 Conclusion

We have conducted a thorough analysis of the numerical stability associated with the BVP method (Debreu et al., 2022) for tracer and momentum advection on a Cartesian C-grid. Our main objective was to investigate the constraints on the time-step imposed by the BVP method, focusing on three key parameters: height penalisation (ϕ_{\min}), friction, and the spreading of the penalised region.

Our findings indicate that using a sharp interface with penalisation defined on two grid points results in a time-step constraint proportional to $1/\phi_{\min}$. However, by smoothing the porosity field and spreading the penalised region, we were able to significantly mitigate this numerical constraint. It should be noted that conventional filtering methods, such as Shapiro or hyperbolic tangent, tend to exhibit progressive saturation. We observed that employing a penalised interface resolved across six grid cells provided the most significant benefit, reducing the time-step constraint by a factor of ten.

Furthermore, the incorporation of friction within the penalised region proved to be effective in reducing the numerical constraint by slowing down the currents. To estimate friction in the porous region, we introduced an adaptive method that ensures the numerical stability of the model. This adaptive approach should be considered when defining the viscous boundary condition for actual topography.

In conclusion, the introduction of a penalised medium introduces an additional constraint on the model time-step, which is influenced by the minimum porosity value. Exploring alternative spreading methods that effectively alleviate the numerical constraint holds potential for implementing more realistic conditions with the BVP in ocean climate models. Additionally, while the adaptive method presented in this study avoids the need to reduce the time-step, further evaluations are necessary to link friction and porosity conditions to the physical stress exerted by topography. Future work will address these aspects of the study.

Addressing the Staircase Effect in Overflows With the Brinkman Volume Penalisation Method

Introduction

In the lifecycle of a dense water mass, overflows often constitute a critical step that initiates the water mass's journey into the abyss. These overflows, or dense gravity currents, result when dense water formed behind confining topographic barriers, or on a continental shelf, escapes into the deep ocean over a sloped sea floor ([Legg et al., 2009](#)). During the descent, overflowing water masses undergo intense turbulent mixing until they reach a state of buoyant equilibrium with the surrounding waters. Overflows are key in the global ocean overturning circulation as they supply dense waters to the deep ocean. However, their representation in z -coordinate ocean general circulation models often falls short of reality.

Specifically, a recurring challenge faced by such models in simulating overflows is the excessive spurious mixing that occurs during the descent, leading to the loss of characteristic features in the final water mass. The origins of this spurious mixing are not completely understood, although it is known that the staircase-like nature of the bottom boundary leads to excessive dilution of dense waters as they undergo convective mixing at each step. Hence, the deficiencies in the representation of overflows are primarily attributed to the stepped representation of bottom topography in z -coordinate models, which forces artificial mixing when a gravity current overflows a step ([Winton et al., 1998](#)).

Adopting the shaved cells approach ([Adcroft et al., 1997](#)) instead of the traditional partial cells method can mitigate but not eliminate the spurious mixing. This suggests that the underlying causes may require deeper investigation, as illustrated by [Q. Wang et al. \(2008\)](#). Previous studies identified other factors affecting the spurious mixing, such as the vertical and horizontal spatial resolution ([Legg et al., 2006](#); [Colombo et al., 2020](#)) or the numerical formulations employed for solving the advection of the water mass ([Riemenschneider & Legg, 2007](#); [Ilıcak et al., 2012](#)). It appears that the only solution to reduce spurious mixing to a satisfactory level

in z -coordinate models is to substantially increase the spatial resolution of the mesh. This solution is incompatible with climate applications (which require long integration of basin-scale models) and current computing resources.

In this study, we explore the potential of the Brinkman Volume Penalisation (BVP) method (Debreu et al., 2022, 2020; Kevlahan et al., 2015) to overcome some of the spurious effects of staircase-like topography, while maintaining a fixed spatial resolution and time step. Our goal is to use BVP to effectively spread the land-ocean interface and improve the representation of bottom currents. In section 1, we reproduce the idealised configuration of an overflow presented by Ilıcak et al. (2012). Then, we propose and validate two modifications in the discrete momentum advection that contribute to reduce the spurious mixing in z -coordinate models (section 2). In section 3, we present a new representation of the topography using the BVP method, and assess its impact on dense water properties by comparison to traditional representations of bathymetry, such as partial cells (Adcroft et al., 1997) and terrain-following methods (section 3). We summarise our results and recommendations in section 4.

1 Model setup

1.1 Configuration

To investigate the spurious effects of staircase-like topography, we adopt the idealised overflow configuration introduced by Ilıcak et al. (2012). Our model domain is a two-dimensional (x, z) basin with a depth of 2000 m and a length of 200 km. Bathymetry is described by the analytical profile $b(x)$, which consists of a steep topographic slope connecting a 500 m deep continental shelf to the 2000 m deep abyssal plain. The profile is given by

$$b(x) = 500 + \frac{1500}{2} \left(1 + \tanh \frac{x-40}{7} \right) \quad (\text{III.1})$$

Figure III.1a provides a visual representation of the configuration, with the topographic variation depicted in grey shading. The initial state involves a cold water mass (10°C) at rest within the first 20 km of the continental shelf, indicated by the blue region in Figure III.1a. This water mass exists in a relatively lighter environment (20°C), represented by the red region in Figure III.1. The density anomaly is calculated using the linear equation of state, resulting in a value of 2 kg/m³.

To address the issue of spurious mixing during overflows, Ilıcak et al. (2012) exclude the use of horizontal and vertical diffusivity for tracer advection. However, the choice of excluding diffusion is debatable considering the prevalence of static instabilities in overflows and the absence of non-hydrostatic physics in the configuration. Isopycnal models naturally restore column stability, whereas height or terrain following models require specific treatments to avoid simulating non-physical vertical inversions in the density field. To circumvent this issue, we use a parameterisation of convection called 'enhanced vertical diffusion'. This parameterisation introduces a high vertical diffusivity of 10 m² s⁻¹ when the stratification is statically unstable (negative buoyancy frequency). The enhanced vertical diffusion affects only the tracer field and effectively reduces noise in the column, resulting in diminished spurious mixing.

The primitive equations in the (x, z) domain can be expressed as follows:

$$\partial_t(hu) + \partial_x(hu^2) + h\partial_z(wu) = \frac{h}{\rho_0} \partial_x P|_z + h\partial_z(k_z^m \partial_z u) \quad (\text{III.2a})$$

$$\partial_t(h\rho) + \partial_x(hu\rho) + h\partial_z(w\rho) = h\partial_z(k_z^t \partial_z \rho) \quad (\text{III.2b})$$

$$\partial_t h + \partial_x(hu) + h\partial_z w = 0 \quad (\text{III.2c})$$

$$\partial_z P = -\rho g \quad (\text{III.2d})$$

with (u, w) the velocity vector where w is the velocity across model levels, $h = \partial z / \partial k$ represents the layer thickness where k is the index of the vertical coordinate, P the pressure field, k_z^m the vertical viscosity, k_z^t the vertical diffusivity, g gravity and ρ_0 a reference density of 1026 kg m^{-3} .

1.2 Numerical formulations

We conducted numerical simulations using the overflow option (OVERFLOW) of NEMO v4.0 (Madec & NEMO System Team, 2022), which uses a C-grid.

Selecting an appropriate discrete formulation for tracer advection can be a challenging task, because it involves striking a balance between the advective component which can generate spurious grid-scale oscillations and the diffusive component which damps these oscillations whilst possibly generating numerical mixing. The diffusive component can either be inherent to the scheme itself (as in odd-centered schemes) or explicitly added (Lemarié et al., 2012). Ideally, diffusion within the tracer advection scheme should be strong enough to eliminate grid-scale accumulation of variance but weak enough to preserve characteristics of water masses. Here we turn to Flux Corrected Transport (FCT) schemes, which are non-linear, monotonic schemes that employ anti-diffusion and non-linear limiters to prevent oscillations (Zalesak, 1979; Lévy et al., 2001). More precisely, we employ the fourth order formulation of FCT using a centered and a compact scheme in the horizontal and vertical directions, respectively.

The discretisation of momentum advection is performed with a modified third order Upstream scheme (Madec & NEMO System Team, 2022) in the horizontal directions and a second order centered scheme in the vertical direction.

To reduce computational cost and enable the use of larger time steps, we activate the Courant-number-dependent treatment of vertical velocity proposed by Shchepetkin (2015). This approach implies to solve both momentum and tracers with implicit time integration and first order upstream scheme applied to the fraction of vertical advection that exceeds the Courant-Friedrichs-Lewy (CFL) condition. Since the method employs a first-order upstream approach for spatial derivatives, it introduces more diffusion compared to the fourth order compact interpolation used in the FCT scheme. To minimise the additional diffusion associated with this approach, the method is wisely designed to activate only when and where necessary (hence its application is restricted in both space and time).

Finally, the Leap Frog Robert-Asselin time stepping scheme (Leclair & Madec, 2009) is used with a time step (Δt) of 10 s. The horizontal mesh resolution is 1 km, while the vertical grid consists of 100 levels. The vertical viscosity k_z^m is prescribed as $10^{-4} \text{ m}^2 \text{ s}^{-1}$, and the vertical diffusivity k_z^t remains zero, except during the activation of enhanced vertical diffusion. A linear sea surface height treatment is assumed.

1.3 Flow characteristics

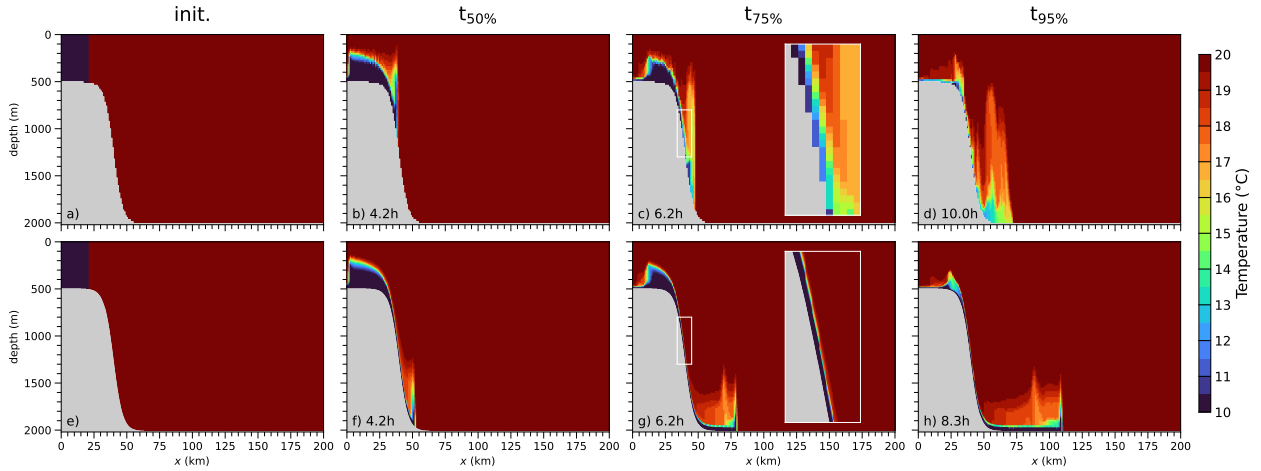


Figure III.1: Evolution of the temperature field during the overflow. The bathymetry, shaded in grey, is represented either with z -coordinate using partial steps (panels a-d) or with s -coordinate (panels e-h). Shading depicts the temperature. Panels a and b shows the initialisation. Other panels show snapshots of the solution, when 50% (b,f), 75% (c,g), and 95% (d,h) of the initial volume of dense waters has left the continental shelf ($x = 20$ km). The corresponding elapsed time $t_{50\%}$, $t_{75\%}$ or $t_{95\%}$ is indicated in the bottom left corner of each panel. Insets in panels c and g are zooms of the region outlined by a white rectangle.

Figure III.1 demonstrates the time evolution of the overflow. Bathymetry, shaded in grey, is represented either with depth (z) coordinate using partial steps (panels a-d) or with a terrain-following (s) coordinate (panels e-h). The partial cells representation creates artificial staircase like topography, as illustrated in the inset of panel c. Temperature is visualised using a color gradient, ranging from dark blue for cold (dense) waters at 10°C to dark red for warm (light) waters at 20°C. Bright shadings (between dark blue and dark red) indicate intermediate temperatures, hallmarking the occurrence of diapycnal mixing during the simulation. The initial state is depicted in the left-most panels (a, e). The temporal evolution of the simulated overflows is shown from left to right. To best illustrate the sensitivity to the chosen vertical coordinate, shown snapshots correspond to times when an equivalent volume of shelf waters has participated in the overflow. Specifically, panels (b, f), (c, g), and (d, h) correspond to the instants when 50%, 75%, and 95% of the initial volume of dense waters has exited the first 20 km of the continental margin, respectively. The elapsed time, denoted as $t_{50\%}$, $t_{75\%}$, or $t_{95\%}$, is indicated in the bottom left corner of each panel.

In all cases, the gravity current displays a distinctive frontal structure characterized by a leading edge or 'head' that advances along the slope, displacing lighter waters and forming a plume above. The head region is continuously fed by the trailing tail, which constitutes the main body of the flow. The density anomaly within the head region accelerates the front, while mixing processes work to slow down its progress by diluting dense waters.

The front in the s -coordinate simulation rapidly reaches the base of the slope at $t_{50\%}$ (panel f), accompanied by a well-confined bottom current (zoom in panel g). On the abyssal plain, the resulting water mass exhibits a distinct dense core at 10°C (dark blue), indicating minimal spurious mixing as compared to the z -coordinate simulation.

The z -coordinate overflow is considerably slower (compare panels b and f). This is because dense waters experience pronounced mixing along the steps, reducing the density anomaly that drives the gravity current. The along-slope temperature gradient in the inset of panel c illustrates the progressive loss of densest waters during the descent. When reaching the abyssal plain, the densest water is close to 14°C , forming the narrow patch of cyan color in panel d.

Figure III.1 thus demonstrates that artificial steps tend to impede overflows and to excessively mix the sinking bottom waters, consistent with previous findings (Ilıcak et al., 2012). In the following, we will explore numerical approaches susceptible to mitigate these spurious effects of staircase-like topography.

2 A modified momentum advection scheme to reduce numerical mixing

In order to minimise spurious mixing effects, it is crucial to ensure well-resolved advection speeds (Riemenschneider & Legg, 2007; Ilıcak et al., 2012). Keeping this objective in mind, we undertake a reassessment of the discrete formulation employed in NEMO for momentum advection.

2.1 A modified UBS scheme for momentum advection

Let us write the spatial discretisation of the flux-form advection of momentum in both horizontal and vertical directions,

$$\partial_t(hu)_{i+\frac{1}{2},k} = \frac{1}{\Delta x} (U_{i,k}u_{i,k} - U_{i+1,k}u_{i+1,k}) + \frac{1}{\Delta z} (W_{i+\frac{1}{2},k-\frac{1}{2}}u_{i+\frac{1}{2},k-\frac{1}{2}} - W_{i+\frac{1}{2},k+\frac{1}{2}}u_{i+\frac{1}{2},k+\frac{1}{2}}) \quad (\text{III.3})$$

with (U, W) the advective flux, (u, w) the momentum flux and (i, k) the discrete indexing of the mesh, k being oriented upward.

The Upstream Biased Scheme (UBS) for momentum advection in NEMO, presented in (Madec & NEMO System Team, 2022), differs from the standard third order Upstream scheme (hereafter UP3) in several aspects:

- i) The interpolation of u in the x direction is carried out using the three-point, upstream-biased, quadratic (parabolic) scheme, given by:

$$u_{i,k} = \frac{1}{2}(u_{i-\frac{1}{2},k} + u_{i+\frac{1}{2},k}) - \begin{cases} \frac{1}{6}u''_{i-\frac{1}{2},k}, & \text{if } U_{i,k} \geq 0 \\ \frac{1}{6}u''_{i+\frac{1}{2},k}, & \text{otherwise} \end{cases} \quad (\text{III.4})$$

Here $u''_{i-\frac{1}{2},k} = u_{i-\frac{3}{2},k} - 2u_{i-\frac{1}{2},k} + u_{i+\frac{1}{2},k}$. Due to Leap-Frog temporal integration, the first term in Equation III.4 represents the centered-in-time advective part, while the second term is forward in time, serving as the diffusive part. This arrangement ensures the preservation of stability in the space-time discretization.

- ii) Following the implementation in the CROCO model (Jullien et al., 2022), the horizontal advective flux U is computed using a fourth order centered interpolation (hereafter C4),

$$U_{i,k} = \frac{1}{4}(U_{i-\frac{1}{2},k} + U_{i+\frac{1}{2},k}) - \frac{1}{32}(U''_{i-\frac{1}{2},k} + U''_{i+\frac{1}{2},k}) \quad (\text{III.5})$$

- iii) A second order centered scheme (hereafter C2) is used in the vertical direction where both advective fluxes $W_{i+\frac{1}{2},k+\frac{1}{2}}$ and horizontal momentum are calculated with a second order interpolation scheme,

$$W_{i+\frac{1}{2},k+\frac{1}{2}} u_{i+\frac{1}{2},k+\frac{1}{2}} = \frac{1}{4}(W_{i,k+\frac{1}{2}} + W_{i+1,k+\frac{1}{2}})(u_{i+\frac{1}{2},k} + u_{i+\frac{1}{2},k+1}) \quad (\text{III.6})$$

Achieving consistency between advection and continuity

Maintaining consistency between momentum advection and the continuity equation is crucial for preserving essential quantities such as kinetic energy. However, there are concerns regarding the current formulation.

First, the interpolation scheme for momentum advection in the horizontal directions is fourth order, while the continuity equation is discretised with a second-order scheme. This inconsistency breaks energy conservation at the discrete level (not shown). To address this, a fourth-order interpolation scheme should be employed for continuity as well.

Second, the computation of advective fluxes for momentum relies on a C4 interpolation in the horizontal directions, whereas the vertical fluxes are interpolated using a C2 scheme. This disparity in interpolation schemes breaks momentum conservation, which can lead to spurious oscillations.

To overcome these issues, we propose a modified implementation of the momentum advection scheme. We suggest using a C2 interpolation for the horizontal advective fluxes to ensure consistency with the vertical fluxes and achieve more accurate momentum preservation. In the

x -direction, this formulation can be expressed as:

$$U_{i,k} = \frac{1}{2}(U_{i-\frac{1}{2},k} + U_{i+\frac{1}{2},k}) \quad (\text{III.7})$$

In this case, the divergence in Equation III.3 simplifies with our suggestion to a C2 interpolation in the x direction of the continuity equation, which holds true due to the incompressibility of the flow. Assuming a spatially uniform horizontal velocity field u with a value of unity, the momentum preservation (Equation III.3) can be expressed as:

$$\partial_t(hu)_{i+\frac{1}{2},k} = \frac{1}{2\Delta x} \left[(U_{i-\frac{1}{2},k} - U_{i+\frac{1}{2},k}) + (U_{i+\frac{1}{2},k} - U_{i+\frac{3}{2},k}) \right] \quad (\text{III.8a})$$

$$+ \frac{1}{2\Delta z} \left[(W_{i,k-\frac{1}{2}} - W_{i,k+\frac{1}{2}}) + (W_{i+1,k-\frac{1}{2}} - W_{i+1,k+\frac{1}{2}}) \right] \quad (\text{III.8b})$$

$$= 0 \quad (\text{III.8c})$$

Built-in diffusion for vertical momentum advection

A C2 approximation for an advected quantity is known to be susceptible to dispersive errors. If these errors are not properly addressed, they can lead to the emergence of non-physical solutions. This is the case in iii) for the vertical interpolation of horizontal momentum. While the addition of explicit vertical diffusion could potentially damp these oscillations, determining an appropriate level of diffusion is a challenging task. Indiscriminate diffusion may result in excessive damping in certain regions of the flow, thereby compromising the accuracy of the solution.

To address this issue, we propose a refinement in the vertical advection scheme by replacing the C2 vertical averaging of u with a formulation similar to a standard UP3 scheme. The UP3 scheme is specifically designed to exhibit dissipative leading-order errors and effectively damp dispersive (phase) errors. In other words, we suggest utilizing an UBS scheme in the vertical direction. This modification enables us to eliminate the explicit vertical diffusion in Equation III.3, and accordingly we set k_z^m to zero. By adopting this approach, we aim to improve the accuracy of the solution while mitigating the unwanted dispersive errors associated with the C2 scheme.

Similar to Equation III.4, we can express a three-point, upstream-biased, quadratic (parabolic) interpolation of u at the mid-points in the vertical direction:

$$u_{i+1/2,k+1/2} = \frac{1}{2}(u_{i+\frac{1}{2},k} + u_{i+\frac{1}{2},k+1}) - \begin{cases} \frac{1}{6}u''_{i+\frac{1}{2},k}, & \text{if } W_{i+\frac{1}{2},k+\frac{1}{2}} \geq 0 \\ \frac{1}{6}u''_{i+\frac{1}{2},k+1}, & \text{otherwise} \end{cases} \quad (\text{III.9})$$

where $u''_{i+\frac{1}{2},k+1} = u_{i+\frac{1}{2},k} - 2u_{i+\frac{1}{2},k+1} + u_{i+\frac{1}{2},k+2}$.

2.2 Sensitivity analysis

We aim to evaluate the numerical choices discussed above in both depth (z) and terrain-following (s) coordinate systems. The tested combinations of schemes are summarized in Table III.1. The 'Refz' and 'Refs' combinations serve as reference experiments, using the default momentum advection implementation in NEMO. The combination 'Cz/s' incorporates consistent interpolation of the horizontal advective fluxes as described in Eq. III.7, while 'Uz/s' employs the UBS method for vertical advection of horizontal momentum (Eq. III.9). The combination 'CUz/s' combines both modifications.

Figure III.2 presents the results for the z -coordinate system with partial bottom cells, while Figure III.3 displays the results for the s -coordinate system. To gauge spurious mixing associated with the different discretisation schemes, temperature and horizontal velocity fields are depicted in the final state of the overflow, corresponding to $t_{95\%}$.

Table III.1: Tested combinations of momentum advection formulations, in horizontal and vertical directions, for z -coordinate and s -coordinate systems. Topography represented in z -coordinate are treated with 'partial cells' (Adcroft et al., 1997).

Simulation	Horizontal dir.	Vertical dir.	Bottom representation
Refz/s	C4/UBS	C2/C2	z or s -coordinate
Cz/s	C2/UBS	C2/C2	z or s -coordinate
Uz/s	C4/UBS	C2/UBS	z or s -coordinate
CUz/s	C2/UBS	C2/UBS	z or s -coordinate
BVP(n)	C2/UBS	C2/UBS	z -coordinate with BVP method where n indicates the level of smoothing of the porosity field (see section 3).
CUz/s(n)	C2/UBS	C2/UBS	z or s -coordinate, using a smoothed topography where n indicates the level of smoothing of the slope.

Comparison between Figure III.2a, representing the default version of NEMO, and Figure III.2c, shows that a consistent computation of momentum fluxes reduces numerical diffusion of temperature in the z -coordinate system. In particular, bottom waters at the foot of the continental slope are colder by a few degrees in Figure III.2c relative to Figure III.2a.

Figure III.2f illustrates the zonal velocity field for the same experiment as shown in Figure III.2b, except that UBS is used instead of C2 for vertical advection. Dispersive errors are observed throughout the solution using C2, as shown by the grid-scale noise. Application of the UP3 scheme effectively eliminates these errors in the velocity field, meaning that the default levels of vertical viscosity were too little. This improvement is then reflected in the advected temperature field: bottom waters at the foot of the slope are noticeably denser with the UBS scheme (Figure III.2e) compared to the C2 scheme (Figure III.2a). This behaviour is expected since treating momentum advection with built-in diffusion results in a smoother velocity field,

III. ADDRESSING THE STAIRCASE EFFECT IN OVERFLOWS WITH THE BRINKMAN VOLUME PENALISATION METHOD

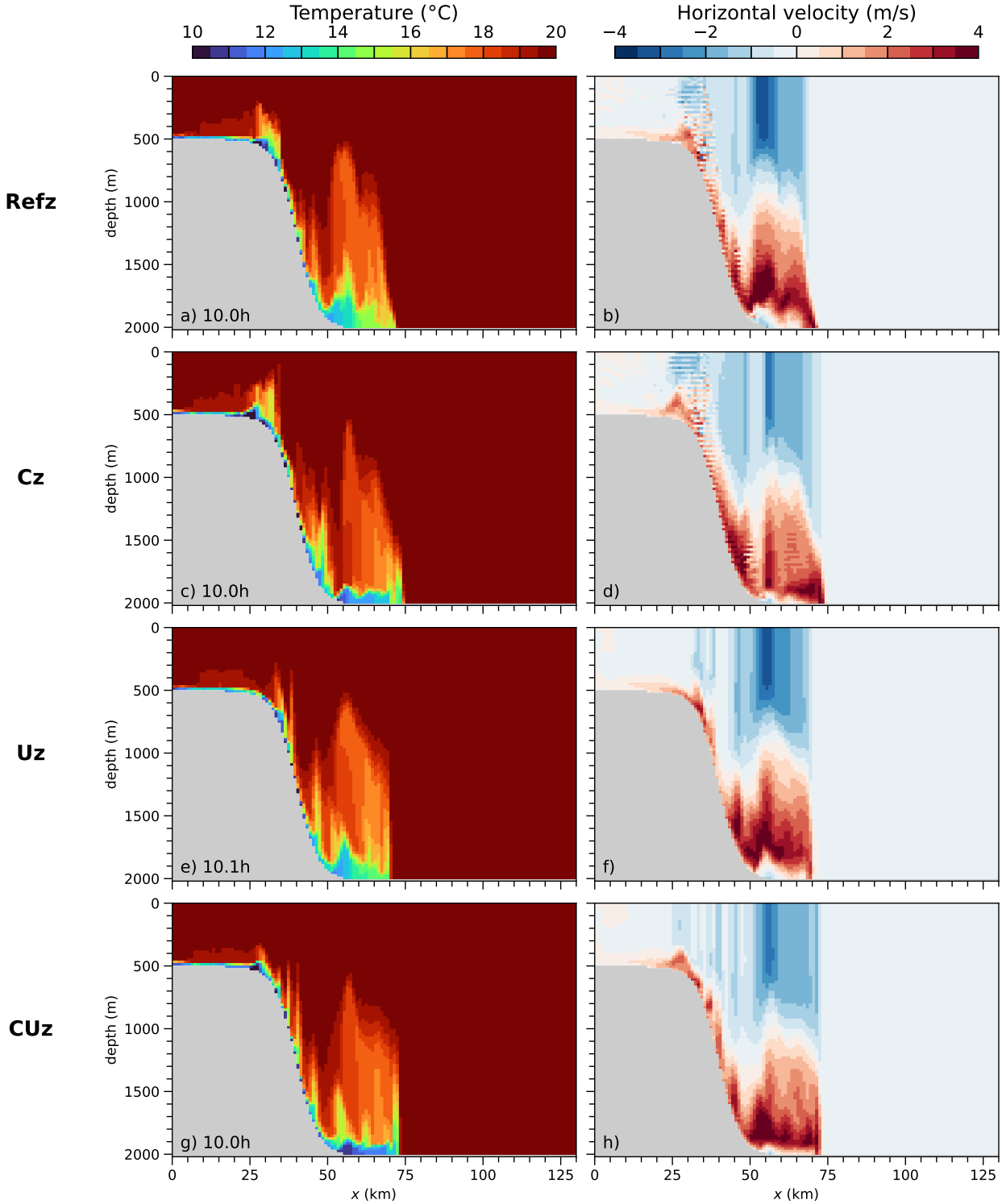


Figure III.2: Snapshots of the overflow simulations solved in z -coordinate with partial bottom cells, for the four combinations of advection schemes listed in Table III.1. Bathymetry is shaded in grey. Snapshots correspond to the time (indicated on each panel) at which 95% of the initial dense water volume has left the continental shelf. The left column displays the temperature field, while the right column shows the horizontal velocity field. Each row corresponds to a specific combination of horizontal and vertical advection schemes: a) and b) represent the reference experiment, Refz; c) and d) correspond to Cz; e) and f) depict Uz; and g) and h) illustrate CUz. It is worth noting the better preservation of cold water (dark blue colour in the left panels) and the reduction of noise in the velocity field achieved through the use of improved numerical schemes.

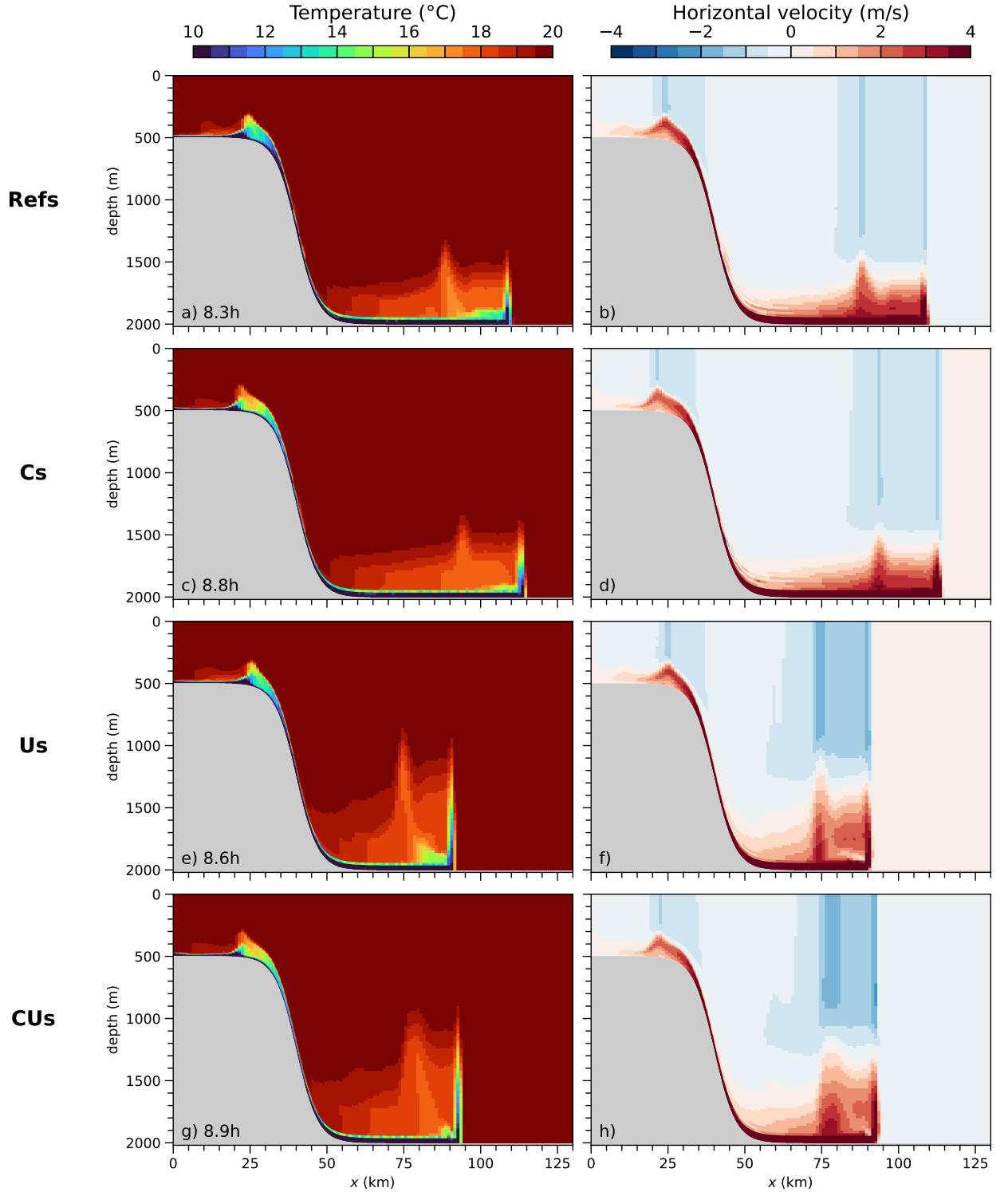


Figure III.3: Snapshots of the overflow simulations solved in s -coordinate, for the four combinations of advection schemes listed in Table III.1. Bathymetry is shaded in grey. The left column displays the temperature field, while the right column shows the horizontal velocity field. Snapshots correspond to the time (indicated on each panel) at which 95% of the initial dense water volume has left the continental shelf. Each row corresponds to a specific combination of horizontal and vertical advection schemes: a) and b) represent the reference experiment, Refs; c) and d) correspond to Cs; e) and f) depict Us; and g) and h) illustrate CUs. It is worth noting the slowdown of the sinking plume and the reduction of the noise in the velocity field achieved through the use of an UP3 scheme for the vertical advection.

leading in turn to less spurious mixing of the transported tracer. A consistent computation of momentum fluxes in the horizontal and vertical, using the C2/UBS formulation for both, proves to be the best combination (Figure III.2g,h). In particular, dense water mass characteristics are much better preserved during the downslope flow relative to the reference experiment.

Changes in the s -coordinate solutions are expected to be less pronounced due to smaller dia-surface velocities. The same modifications of momentum advection yield only small differences in mixing levels within the overflow (compare e.g. Figure III.3a with Figure III.3c). As anticipated, the low level of noise near the end of the slope is eliminated when switching to UP3 advection (compare Figure III.3f with Figure III.3b). Nonetheless, the sinking rate of the dense water mass is sensitive to the discrete formulation of vertical advection. With C2 advection, the front position is approximately $x = 110$ km at $t_{95\%}$ (Figure III.3a), while it is about 15 km upstream with the UBS scheme (Figure III.3e). This corresponds to a significant slowdown of approximately 0.7 m s^{-1} . The slower sinking rate is in better agreement with the overflow solutions obtained by Ilıcak et al. (2012) with 'ROMS', 'viscous MOM' and the layered model 'GOLD' (see their Figure 9).

2.3 A diagnostic of numerical mixing

To gain insights into the characteristics of the dense water reaching the foot of the slope, we perform a volumetric diagnosis to quantitatively evaluate the impact of different momentum advection discretisations on spurious mixing. Figure III.4 compares the temperature distributions of the water mass volume reaching the foot of the slope. More precisely, the volume passing through $x = 60$ km is accumulated over time for each temperature class until the total volume reaches 20 Gm^3 . Differences in the distributions reflect the reduction or enhancement of spurious mixing. To avoid potential interpolation errors, the thermal flux computed in the FCT44 scheme is divided by the mass transport U , after flux limiting, giving the effective advected temperature. The results are presented in Figure III.4, where the effective temperature is plotted on the x -axis, and the advected volume is displayed on the y -axis on a logarithmic scale.

The diagnostic presented in Figure III.4a aligns well with the results shown in Figure III.2. In z -coordinate, the volume distributions are primarily characterized by a broad peak centered around 18°C . This peak corresponds to the plume of mixed waters observed in the simulations over the head region. The volume in each temperature class decreases gently towards colder temperatures until it abruptly drops at a relatively cold temperature.

Beyond these common characteristics, reddening of the distribution due to modifications in the momentum advection is apparent. The modified UBS formulation brings a notable increase in volume of waters colder than 16°C , and a shift of the minimum temperature towards colder

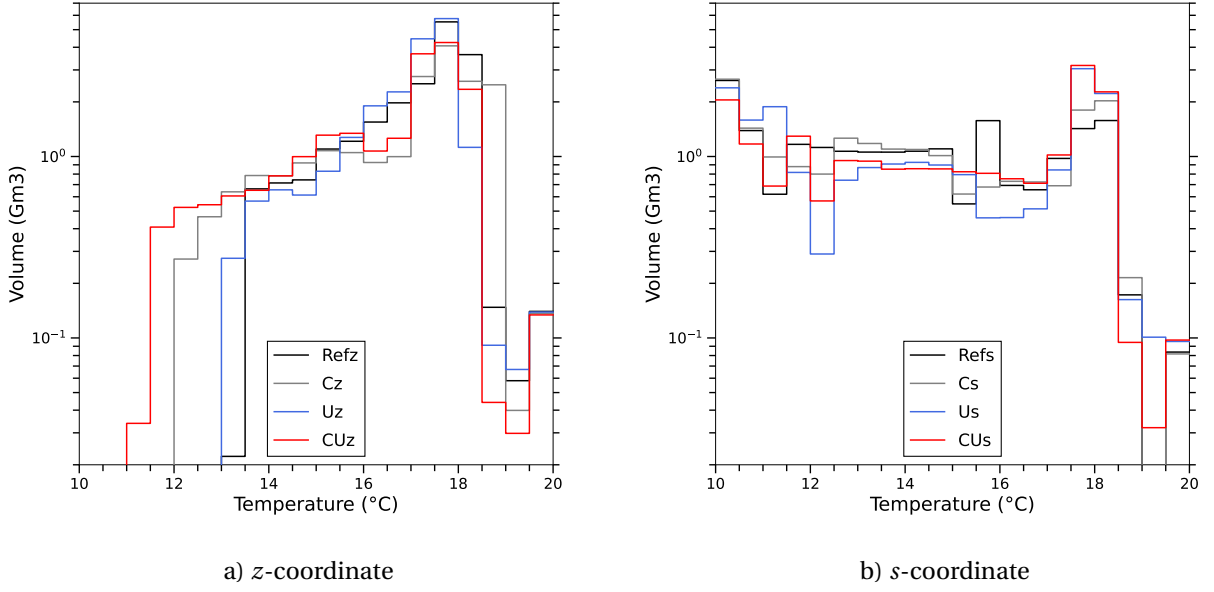


Figure III.4: Temperature distribution of waters reaching the foot of the slope, accumulated until a total volume of 20 Gm³ has crossed $x = 60$ km. Panel (a) shows the solutions using the *z*-coordinate, and panel (b) shows solutions using the *s*-coordinate. The colour sequence (black, grey, blue, and red) corresponds to the combinations ((Refz,Refs), (Cz,Cs), (Uz,Us), and (CUz,CUs), respectively) listed in Table III.1. The volume is presented on the y-axis using a logarithmic scale. Temperature bins have a width of 0.5°C. It takes approximately 11 hours of simulation to reach 20 Gm³ in *z*-coordinate, while it takes only about 7.5 hours in *s*-coordinate.

classes. In the default implementation ('Refz', in black), waters reaching the foot of the slope are always warmer than 13.5°C (cf. the small patch of cyan in Figure III.2a). By switching to the consistent formulation 'Cz' (in grey), volume shifts towards colder temperatures, and the minimum temperature decreases by 1.5°C. Although 'Uz' does not significantly reduce spurious mixing (compare blue and black), it is the combination of both modifications ('CUz', in red) that yields the most substantial improvement in preserving cold waters as they sink. The 'CUz' combination enables water as cold as 11.5°C to reach the foot of the slope.

The volume distributions obtained from the *s*-coordinate simulation (Figure III.4b) show distinct differences compared to those obtained with the *z*-coordinate. They exhibit a narrow peak centered around 18°C and relatively uniform volume in the colder temperature classes, with another peak near the initial temperature of dense waters (10°C). Upon comparing each combination in Figure III.4b, no substantial changes are observed in the properties of the waters flowing through $x = 60$ km. The total volume of waters colder than 16°C remains largely unchanged, indicating that the observed slowdown in the sinking rate in 'Us' should not be attributed to a more diluted water mass, but rather to the additional vertical diffusion introduced.

In summary, we have carefully examined the discrete formulation of momentum advection in the OVERFLOW configuration of NEMO. We propose a correction to the discrete formulation of the horizontal UP3 scheme, which resolves an inconsistency between advection and the continuity equation. Additionally, we introduce an UP3 scheme in the vertical direction, addressing the dispersive errors that occur with the C2 scheme given the low explicit vertical viscosity chosen by [Ilicak et al. \(2012\)](#). These choices significantly reduce the spurious mixing observed in simulated overflows in the z -coordinate system. The modified UBS scheme will be incorporated into the upcoming release of NEMO (version 5.0). In the following, momentum advection is discretised with consistent formulation with an UBS formulation in both horizontal and vertical directions.

3 Alleviating the staircase effect with Brinkman Volume Penalisation

The presence of artificial steps in the topography leads to strong vertical velocities and convective mixing as bottom currents sink along the staircase-like slope. This in turn induces large and often overestimated mixing of water mass properties. In order to reduce spurious mixing, we explore the potential of Brinkman Volume Penalisation, which may smooth out the slope discontinuities felt by the downslope flow. To evaluate the impact of this approach, we compare simulations employing the BVP method to those using traditional representations of topography, such as depth or terrain-following coordinates.

3.1 Penalised configuration

Following [Debreu et al. \(2020, 2022\)](#), the set of equations governing the penalised primitive equations can be expressed as follows:

$$\partial_t(\tilde{h}u) + \partial_x(\tilde{h}u^2) + h\partial_z(\phi wu) = \frac{\tilde{h}}{\rho_0} \partial_x P|_z - \sigma \tilde{h}u + h\partial_z(\phi k_z^m \partial_z u) \quad (\text{III.10a})$$

$$\partial_t(\tilde{h}\rho) + \partial_x(\tilde{h}u\rho) + h\partial_z(\phi w\rho) = h\partial_z(\phi k_z^t \partial_z \rho) \quad (\text{III.10b})$$

$$\partial_t \tilde{h} + \partial_x(\tilde{h}u) + h\partial_z(\phi w) = 0 \quad (\text{III.10c})$$

$$\partial_z P = -\rho g \quad (\text{III.10d})$$

with $\tilde{h} = \phi h$ the penalised layer thickness and σ the penalty friction exerted through the porous medium. Both mass and momentum contents are altered in the penalised case by the porosity ϕ . This modification affects effective volumes along with the effective transports. Similarly, vertical diffusion takes into account the modified surface areas. The porosity ϕ and friction σ constitute the key parameters in the BVP method.

In order to model a fluid with solid boundaries these variables often take the following discontinuous forms:

$$(\phi, \sigma) = \begin{cases} (\phi_{\min}, 1/\epsilon) & \text{in the penalised region} \\ (1, 0) & \text{in the ocean domain} \end{cases} \quad (\text{III.11})$$

where the parameters ϵ and ϕ_{\min} control the accuracy of the approximation. By setting $\epsilon \ll 1$ and $\phi_{\min} \ll 1$, the penalisation allows to retrieve the frictional and blocking effects of a topography, effectively simulating interactions of a fluid with solid boundaries. One advantageous possibility of the BVP method is to spread this discontinuous interface along the physical boundary. By allowing porosity values between ϕ_{\min} and 1, a smoother transition between land and ocean is achievable. In previous studies, the spreading of the interface has primarily been employed to ensure numerical stability in the model (Kevlahan et al., 2015; Debreu et al., 2020, 2022). The impacts and potential advantages of interface spreading on the behaviour of simulated bottom currents are not well understood. In this study, we aim to explore the effects of interface spreading in the context of overflow dynamics.

At the discrete level, each cell is assigned a porosity value based on whether it is located in the ocean interior or on land. However, some cells near the transition can be considered partly ocean and partly land, because the physical boundary cuts through these cells. To accurately capture the height of the water column, the porosity field then takes intermediate values that correspond to the volume fraction of the liquid part within the cell. In this particular configuration, the position of the physical boundary is determined by the analytical profile $b(x)$ defined in Equation III.1. To estimate the liquid part in the intersected cells, we simply utilise the integral of $b(x)$:

$$\int_{x_1}^{x_2} b(x) dx = \left[\left(500 + \frac{1500}{2} \right) x + 7 \frac{1500}{2} \log(\cosh \left(\frac{40 - x}{7} \right)) \right]_{x_1}^{x_2} \quad (\text{III.12})$$

The minimum porosity plays a crucial role in determining the accuracy of the simulated topography. In order to achieve a refined representation of the topography while mitigating the numerical constraint, we set the height parameter ϕ_{\min} to 10^{-2} . Following the approach described in (Debreu et al., 2020), we control the width of the interface by applying to the porosity field successive passes of a Shapiro filter (1/4, 1/2, 1/4) (Shapiro, 1970) in both the horizontal and vertical directions. Then, face porosities ϕ_u and ϕ_w are defined by averaging the porosities ϕ_t of the neighbouring porous cells, to provide a smooth representation of the slope.

The numerical stability of the BVP method can be compromised by abrupt changes in porosity within the interface region. While spreading enhances stability, some level of friction σ is still necessary in the penalised region to ensure overall stability of the simulation and obviate a drastic increase of temporal resolution. However, it is important to strike a balance and avoid excessive damping, as it can prevent bottom currents from flowing into the penalised region and negate the potential benefits of interface spreading.

To find this balance, we follow the method presented in Chapter II which provides guidance for applying penalty friction that preserves the numerical stability of the BVP method while allowing a certain degree of slipperiness. For each time step, the method introduces the necessary damping to prevent the horizontal Courant number from exceeding a safety factor γ . The value of γ must be chosen in keeping with the CFL condition of the discrete schemes used for advection of tracers and momentum. According to [Lemarié et al. \(2015\)](#), the CFL condition in a Leap-Frog environment is 0.522 for a fourth order centered FCT scheme and 0.472 for an UBS scheme. As a precautionary measure, the safety factor γ is set to 0.1.

To some extent, the definition of the porosity field, before smoothing, follows the principle of shaved cells presented in ([Adcroft et al., 1997](#)). The shaved cells approach provides a smooth representation of the slope by cutting the cells relative to the position of the boundary to account for the real volume of the water column. However, this approach introduces a misalignment of the center of mass of the trimmed cells with the adjacent cells, leading to corrections in the computation of the horizontal pressure gradient (HPG) and potential errors from interpolation. In contrast, within the BVP method, porous cells capture the modification of the volume while preserving their centers aligned with the other cells of the mesh, thereby avoiding any noise in the computation of the HPG.

To verify this assumption, we conducted a reproduction in NEMO of the idealised seamount testcase presented by [Beckmann and Haidvogel \(1993\)](#) and evaluated the treatment of partial cells using the penalisation method (results not shown). These findings confirm the validity of the assumption, consistent with the results of [Debreu et al. \(2020\)](#). In their Figure 10, they demonstrate that penalising the topography over an s -envelope does not introduce any additional errors in the residual currents.

3.2 Simulating overflows with the BVP method

The numerical discretisation is identical to the non penalised case presented in the Methods. Momentum advection is discretised with the modified UBS formulation ('CUz' combination of Table [III.1](#)), which improved conservation of the dense waters. We now evaluate the impact of widening the interface region for the conservation of dense waters.

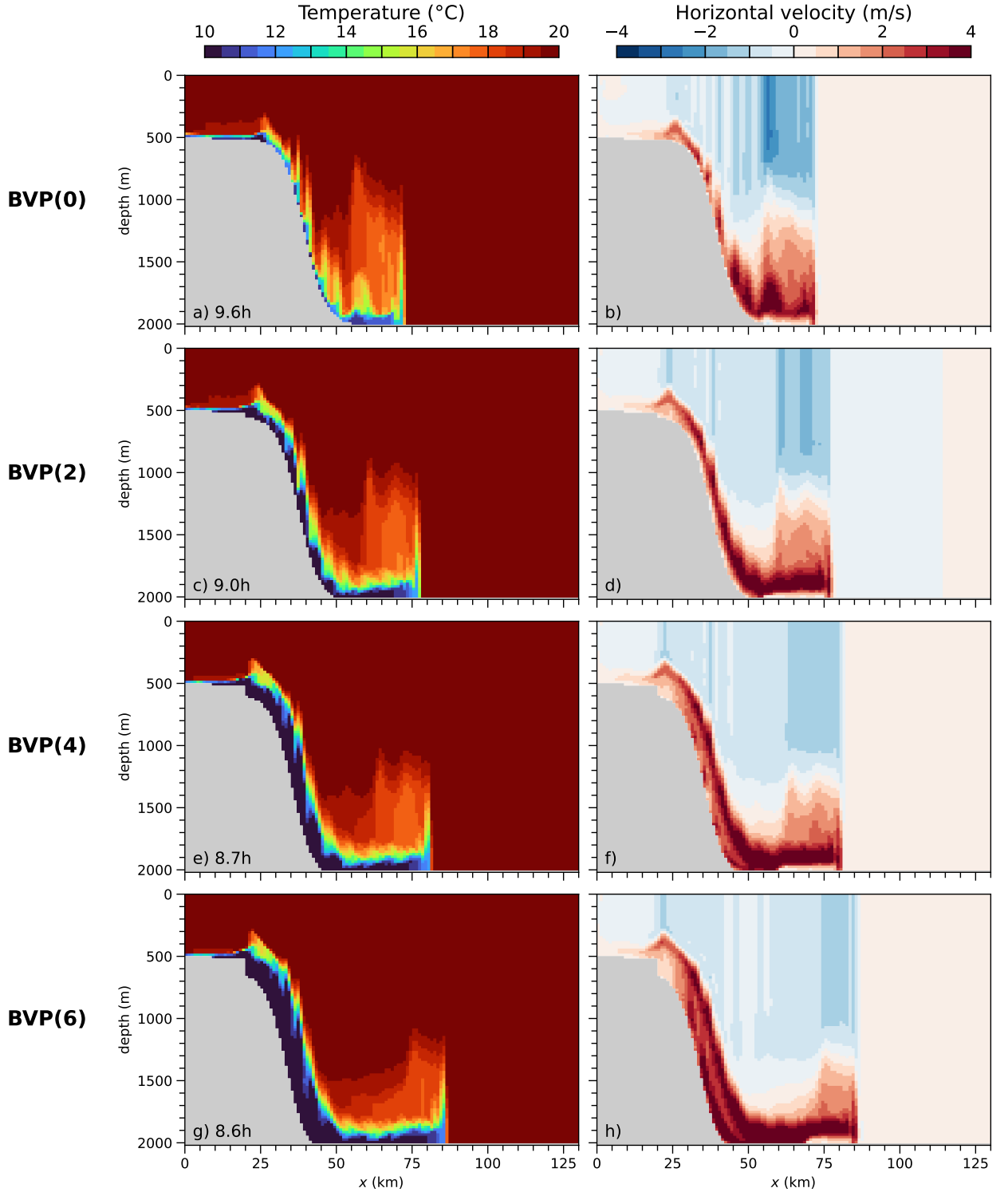


Figure III.5: Snapshots of the overflow simulations solved in z -coordinate with BVP and a varying degree of porosity smoothing. Bathymetry is shaded in grey. The left column displays the temperature field, while the right column shows the horizontal velocity field. Snapshots correspond to the time (indicated on each panel) at which 95% of the initial dense water volume has left the continental shelf. Each row corresponds to a degree of smoothing: zero (top row), two (second row), four (third row) or six (bottom row) passes of the Shapiro filter. It is worth noting the better preservation of cold water (dark blue colour in the left panels) and the widening of the bottom currents achieved through penalisation and smoothing.

Figure III.5 illustrates the overflow behavior in the presence of penalised topography. The left column shows the temperature field, while the right column displays the horizontal velocity field. The solutions are shown at $t_{95\%}$, i.e. when 95% of the dense shelf waters have left the shelf. The grey shading indicates the masked land domain underneath the penalised region, with its staircase pattern. For better comparison with the non penalised case, the first 20 km of the continental shelf remains non-penalised. The number of filtering passes of the porosity field is indicated in parentheses on the left. The widening of the transition zone from the top to bottom is visible in the apparent drop of topography at $x = 20$ km; mind that the true topography felt by the flow is much smoother because low porosity cells are located just above the grey shading.

When using the minimal smoothing level, there are no visible changes between the penalisation and partial cells approaches in terms of topography representation and dense water preservation (compare Figure III.5a with Figure III.2g). However, the sinking rate is slightly faster with the penalisation method. The case with no smoothing is equivalent to using shaved cells (Adcroft et al., 1997). This result thus confirms that a linear-wise representation of the topography cannot eliminate the spurious mixing emerging from stepped topography at a given resolution (Q. Wang et al., 2008).

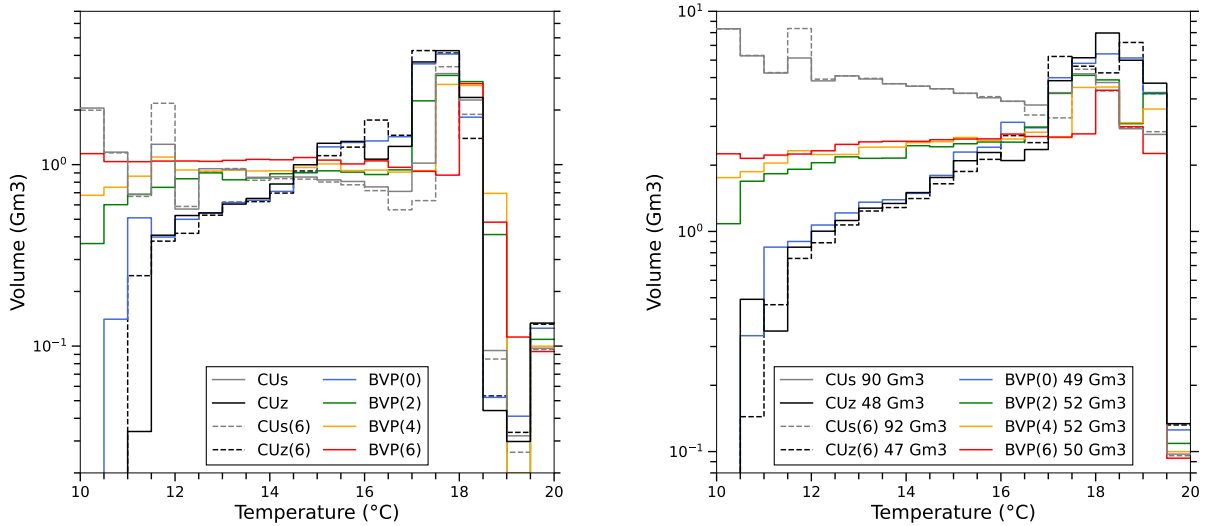
By widening the penalised region, the bottom waters reaching the abyssal plain become denser, as evident from the dark blue patches in Figure III.5c,e,g. The smoothing of porosity also leads to a reduction in the height of the mixed plume above the head region. These changes coincide with a faster sinking rate and the spreading of bottom currents across the porous interface (Figure III.5d,f,h). Hence, our simulations suggest that increasing the width of the land-ocean transition via penalisation tends to reduce spurious mixing occurring within downslope currents in z -coordinate.

When four or six passes of Shapiro filter are used, the eastward velocity has a double maximum structure that appears to be nonphysical (Figure III.5f,h). This should be tempered by recognising that the deeper maximum in velocity is associated with minor volume transport due to the low porosity of bottom cells. Nonetheless, these velocity snapshots indicate that additional constraints on the spatial structure of the friction parameter σ are desirable to avoid spurious behaviours.

In general, snapshots from the penalised simulations must be carefully interpreted since the effective volumes of the cell are modified by the use of porosity and invisible in Figure III.5. Analysing the temperature distributions presented in Figure III.6 provides more quantitative insight into the actual modification of dense waters that reach the foot of the slope. Distributions corresponding to overflows solved in s -coordinate ('CUs') and in traditional z -coordinate with partial cells ('CUz') are also shown for comparison. The diagnostic is computed in panel a when the same volume 20Gm^3 has reached the slope. In panel b, the diagnostic is computed for

the entire 17-hour simulation, with the total transported volume for each simulation indicated in the legend. One noteworthy aspect when comparing z and s -coordinate simulations is the strong difference in the total volume advected eastward (Figure III.6b).

In the previous case, comparing the distributions until the same volume reaches the foot of the slope highlighted the differences between solutions that use the same representation of the topography. Figure III.6a shows the diagnostic reproduced with the penalised solution, suggesting that the penalised solution may behave similarly to an s -coordinate representation. However, the difference in the total volume advected necessitates consideration of the temperature distributions throughout the entire 17-hour simulation (Figure III.6b). This provides a clear delineation of the behavior of downflow currents along topographies represented in either s -coordinate, partial cells, or the penalisation method.



a) Temperature distribution until 20Gm³ has reached the foot of the slope.

b) Temperature distribution throughout the entire 17-hour simulation

Figure III.6: Temperature distribution of dense waters reaching the foot of the slope at $x = 60\text{km}$. The color sequence (blue, green, orange, and red) represents penalised simulations with increasing levels of smoothing. The distributions corresponding to the s -coordinate and partial cells coordinates are shown in grey and black, respectively. The volume is displayed on the y-axis using a logarithmic scale (Gm³), with temperature bins of 0.5°C width. The total outflows for each simulation are indicated in the legend. It is worth noting the increasing volume of dense characteristics with the widening of the penalised region, resulting in performance comparable to an s -coordinate system.

Figure III.6b shows that with increasing size of the penalised region, there is a noticeable increase in cold water volume, down to 10°C, as well as a reduction in the peak volume around 18°C. The distributions thus move toward the s -coordinate reference when resorting to BVP and porosity smoothing. Importantly, only two passes of the Shapiro filter are sufficient to achieve

substantial gain in dense water preservation. This moderate level of smoothing may be optimal since it minimises distortion of the target boundary and maintains a coherent downslope current (Figure III.5d).

3.3 Overflowing a smoothed topography

By spreading the interface, the resulting topography is smoothed, so that the reduction in spurious mixing obtained with BVP could be partly due to the modified effective topography. Previous studies have shown that smoothing a z -coordinate topography can have positive effects on the dynamics (Penduff et al., 2002). However, we should assess whether the improvements obtained here with BVP and smoothing are merely due to modified topography.

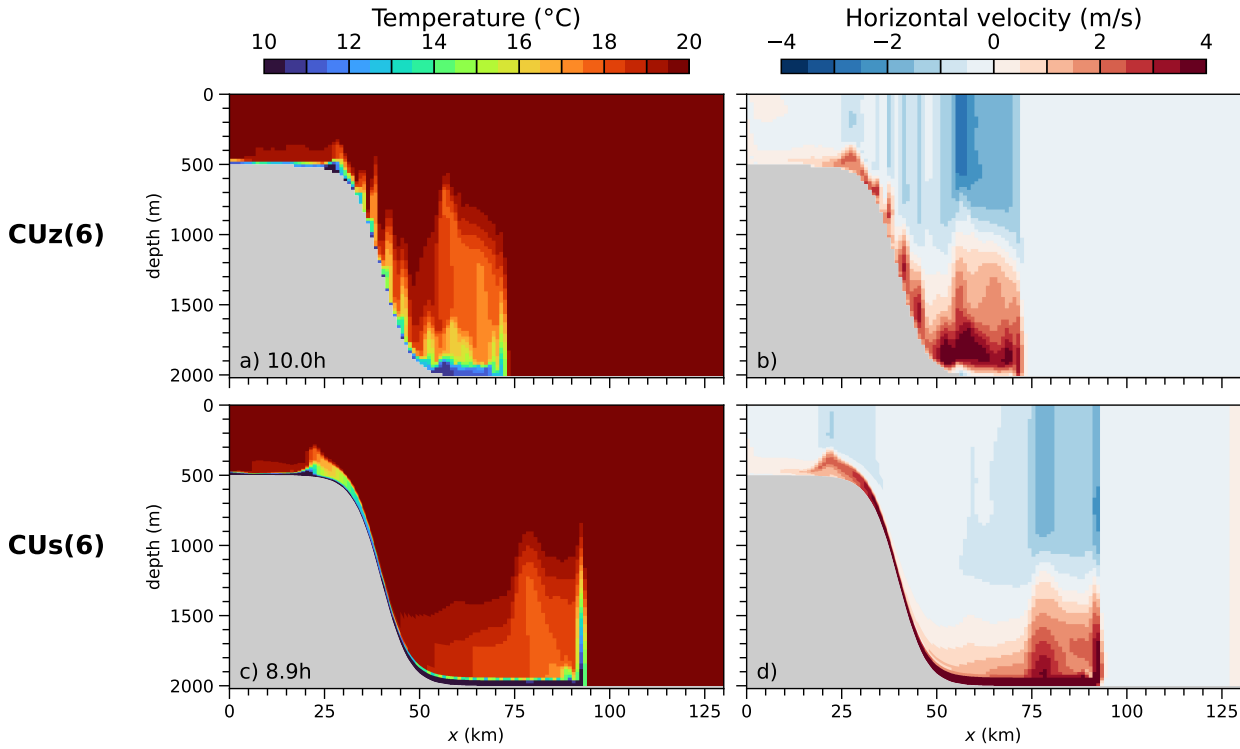


Figure III.7: Snapshots of the overflow simulations solved in z -coordinate and s -coordinate with a smoothed topography. Bathymetry is shaded in grey. Bathymetric profile is obtained after six passes of horizontal filtering of $b(x)$ with a Shapiro filter (1/4,1/2,1/4), giving depths similar to 'BVP(6)'. The left column displays the temperature field, while the right column shows the horizontal velocity field. Snapshots correspond to the time (indicated on each panel) at which 95% of the initial dense water volume has left the continental shelf. Panels a and b (c and d) display the solution solved in partial cells (s -coordinate). It is worth noting that these solutions are nearly indistinguishable from their non-smoothed counterparts (Figure III.2g and III.3g), but they are distinct from the penalised solutions (Figure III.5g).

Figure III.7 presents snapshots of the simulated overflow using partial cells and the s -coordinate system with a smoothed topography. The bathymetric profile is obtained by applying six passes of horizontal filtering to $b(x)$, resulting in water column heights equivalent to 'BVP(6)'. The case with partial cells is denoted as 'CUz(6)', while the terrain following solution

is labeled as 'CUs(6)'. We observe that the solution using partial cells (Figure III.7a) is largely unaffected by the smoothed topography and closely resembles the reference solution (Figure III.2g). This observation holds true for 'CUs(6)' as well (compare Figure III.7c and Figure III.3g).

To complete the evaluation, Figure III.6b displays the temperature distributions for the 'CUz(6)' and 'CUs(6)' combinations, indicated by dotted lines. The curves closely align with their non-smoothed counterparts (solid lines). Hence, the spreading of the penalised topography truly enables the simulated overflows to be less susceptible to spurious mixing; the improvements are not merely due to (slight) distortion of the effective topography.

4 Discussion and conclusions

Quantitative diagnostics of spurious mixing

In this chapter, we evaluated three numerical representations of a topographic slope (z -coordinate with partial cells, s -coordinate, and z -coordinate with penalisation) and several discrete representations of fluid transport in the context of an idealised two-dimensional overflow (Ilıcak et al., 2012). Consistent quantification and comparison of 'spurious mixing' across the simulations is challenging, because the differences occur in several aspects and at several stages of the overflow. In particular, the speed of the downslope flow varies across simulations, since it depends on the density difference between dense sinking water and surrounding waters (hence on the amount of diapycnal mixing). At a given elapsed time, different simulations will be in different stages of the overflow, thus blurring the comparison. Comparing the end state (17 hours) of the simulations is also insufficient, because the temperature distributions then integrate the effects of mixing on the flat abyssal plain which are not our focus here.

To quantify spurious mixing occurring during the downslope flow in a consistent way, we thus developed diagnostics based on the flux of water flowing eastward past the foot of the slope. We calculate both the temperature distribution and the cumulative volume of this flux, then compare temperature distributions for a given volume or at the end of the simulations. The results were shown in Figures III.4 and III.6. To summarise the sensitivity of spurious mixing and overflow strength to numerical choices, we construct a two-dimensional diagram (Figure III.8) showing, for each simulation, the proportion of water colder than 16°C flowing past the foot of the slope (x-axis) against the time to 95% discharge of the initial dense water volume (y-axis). This figure clearly shows the correlation between discharge speed and spurious mixing intensity: a lesser degree of mixing generally goes with a shorter discharge time. In z -coordinate, improvements in the momentum advection scheme increase the proportion of water colder than 16°C from 20 to 30%, with no increase in discharge rate. Use of BVP further increases this percentage, up to about 60% for a large degree of porosity smoothing, and also re-

duces the discharge time by 0.5 to 1.5 hour. Figure III.8 thus demonstrates that resorting to BVP brings the z -coordinate solutions fairly close to the s -coordinate solutions, which have about 75% of water flowing across $x = 60$ km colder than 16°C . These conclusions are insensitive to small changes in the chosen criteria for measuring spurious mixing and discharge time (not shown).

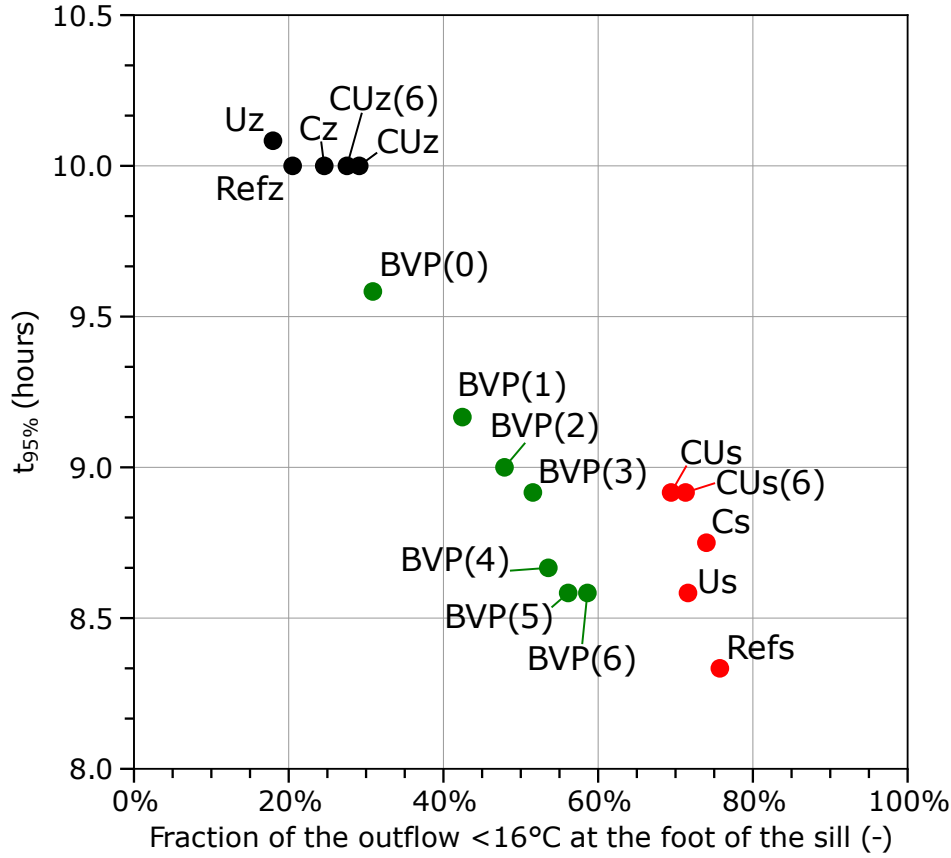


Figure III.8: Diagram of simulated overflows for the conservation of dense waters. The y-axis represents the time in hours at which 95% of the initial dense waters have left the continental shelf. The x-axis indicates the total volume fraction of waters colder than 16°C that crossed $x = 60\text{km}$ throughout the 17-hour simulation. Each dot corresponds to a combination listed in Table III.1. The colors black, green, and red represent simulations using partial cells, penalised z -coordinate, and s -coordinate, respectively. It is noteworthy to observe the migration of the penalised overflow (green) as the interface widens, from partial cells (black) to s -coordinate (red) solutions.

Insights on the benefits of BVP

We now discuss the potential origins of the positive impact of BVP on the simulated overflow. We evoke three potential causes that may explain the obtained reductions in discharge time and dense water dilution.

First, a significant source of spurious mixing arises from the width of cells being larger than the front located at the head of the dense water plume. Indeed, when the front is advected into a cell containing lighter waters, dense water to the left of the front mixes with lighter waters to the right of the front, within this cell and this time step. This cell-scale dilution tends to spread the frontal region of the overflow and hinder the sinking of dense shelf waters.

By penalising the topography, the volume of porous cells becomes smaller as the depth increases. When dense waters enter a porous cell with a reduced effective volume, there is potentially less dilution compared to a fully liquid cell. Improvements in the preservation and sinking of the frontal zone may thus owe to the reduction in the effective volume of cells along the bottom boundary.

Second, the widening of the land-ocean interface contributes to the smooth or spread bottom currents, effectively reducing spurious mixing of the advected tracer field. In the traditional approach, the no-flow condition at the topography is typically enforced on the cells adjacent to the boundary. However, the BVP method takes a different approach by incorporating the blocking effect of the topography within a few cells near the border. The resultant wider interface generates a more distributed topographic constraint on the bottom currents, extending throughout the penalised region. As a consequence, it may act like a broader stencil for the discrete advection scheme, rendering advection less sensitive to artificial steps (Chapter I) and thus naturally minimising spurious mixing.

Furthermore, it is known that advection schemes near walls or boundaries, where bottom currents are confined, can lead to accuracy loss. For example, the fourth-order advection scheme FCT44 degrades to a second-order FCT22 scheme adjacent to a wall, which introduces more diffusion of the tracer fields. Similarly, the diffusive off-centered UBS scheme becomes a second-order centered scheme, which is more prone to dispersive errors in the momentum advection. Therefore, one potential advantage of spreading the interface is to mitigate the accuracy loss of advection schemes at coasts or borders. However, this aspect has not been quantified and requires further investigation.

Third, spurious mixing in z -coordinate overflows is thought to occur partly because of convective instabilities: when dense water moves horizontally (here, to the right) past a step, it may be denser than the underlying water and mix convectively. This process can dilute the sinking dense water very rapidly and thicken the plume much more than realistic entrainment would. The thickening of the land-ocean interface implied by BVP may reduce the prevalence of convective mixing by damping the imprint of topographic slope discontinuities on bottom currents. In addition, the reduction of the effective volume of bottom grid cells with BVP may reduce dilution when convective mixing does occur.

Sources of spurious mixing in overflows simulated by z -coordinate climate models have been discussed and partially addressed in past studies (Snow et al., 2015). With coarse resolution meshes, spurious mixing often produces deep waters that are too light, affecting the simulated stratification and overturning on a global scale (Winton et al., 1998; Downes et al., 2011). To alleviate this problem, overflow parameterisations, such as the downslope transport scheme of Campin and Goosse (1999), are commonly employed in regional or global models. We performed an additional simulation with the parameterisation of Campin and Goosse (1999), which is commonly used in NEMO. The simulation, which used the z -coordinate with partial cells, revealed only minor improvements in the preservation of dense waters (not shown), consistent with our experience with global NEMO configurations. Further work is required to adequately combine BVP with such transport schemes.

Conclusion

Staircase topographies present a persistent challenge in ocean circulation models: artificial steps give rise to intense vertical velocities and excessive mixing as bottom currents descend along the staircase. Currently, effective and computationally affordable solutions to mitigate this spurious mixing in z -coordinate models are lacking. We explored potential avenues to improve the preservation of dense overflowing waters at fixed spatial resolution, using the idealised OVERFLOW configuration (Ilıcak et al., 2012) in NEMO (Madec & NEMO System Team, 2022).

We first showed an inconsistency between the discretisation of momentum advection and the formulation of continuity in NEMO. By employing a second-order accurate interpolation scheme for advective fluxes that adheres to the discrete formulation of the continuity equation, we ensure conservation of momentum and kinetic energy across the basin (in the absence of diffusion or source terms).

Furthermore, we find that adopting the upstream biased scheme (UBS) for vertical advection of momentum, as opposed to the second-order centered scheme, eliminates potential noise in the horizontal velocity field during overflows. The UBS scheme introduces numerical momentum diffusion, effectively eliminating numerical oscillations and promoting smooth flow throughout the water column.

The combination of these modifications significantly reduces spurious mixing in the advected tracer field. Notably, dense waters reaching the foot of the stepped topography are 2°C colder in the overflow simulations. The modified advection scheme will be incorporated in the upcoming release of NEMO (version 5.0). These results underscore the crucial role of discrete momentum advection in addressing spurious mixing in ocean models.

We also investigated the potential of the Brinkman Volume Penalisation (BVP) method to address spurious mixing in z -coordinate overflows. One notable advantage of this method is its ability to spread the interface by smoothing the porosity and friction parameters. This approach effectively reduces the dilution of dense water within cells and spreads bottom currents across the penalised region. The broader interface leads to smoother bottom currents, thereby reducing the sensitivity of advection schemes to artificial steps. Consequently, this improved interface significantly enhances the conservation of dense waters and reduces the discharge time, resembling the performance achieved in s -coordinate representations.

In conclusion, our study highlights that a significant source of spurious mixing in the presence of stepped topography in ocean models is attributed to the treatment of advection. The BVP method offers a practical solution for z -coordinate models to address this issue by spreading the interface without the need for further spatial resolution refinement. However, coarse spatial resolution used in typical climate models may impose limitations on the degree of porosity smoothing and the extent of the penalised region, thereby limiting the benefits of the BVP method. A possibly ideal approach would be to combine BVP with existing parameterisations of bottom boundary layer transport. Alternatively, a promising solution for improving overflow simulations in global or regional configurations is the use of an envelope s -coordinate system in conjunction with the penalisation method, as previously presented in (Debreu et al., 2022, 2020).

Toward Global Realistic Simulations

Introduction

In previous chapters, we have showed that the numerical stability of the Brinkman Volume Penalisation (BVP) method is guaranteed by spreading the penalised region and defining friction in a consistent way (chapter II). We have highlighted the potential of the BVP method as a promising approach for representing topography in ocean models, particularly in terms of removing the errors in the computation of the horizontal pressure gradient and ensuring a smooth discretisation of the bottom (chapter III). However, the advantages of spreading the penalised region may be limited in global configurations where the large vertical resolution of the bottom (approximately 200 m in an ORCA1 configuration ([Madec & NEMO System Team, 2022](#))) can propagate the penalisation too far into the ocean interior. Several questions still need to be addressed to be able to simulate a global ocean using BVP.

In this chapter, we aim to move towards realistic configurations by introducing penalisation in the re-scaled height coordinates proposed by ([Adcroft & Campin, 2004](#)), which are commonly used in ocean circulation models (section 1). While the BVP method ensures the preservation of the speed of internal waves within the porous region ([Kevlahan et al., 2015](#)), its impact on the behaviour of Rossby waves when smoothing coastlines has not been studied. Therefore, our second objective is to investigate the effects of penalisation smoothing on the characteristics of planetary waves (section 2).

1 Penalising the bottom topography

1.1 Re-scaled height coordinate with the BVP method

The free-surface of the ocean exhibits significant variations due to tides and atmospheric forcing. As a result, the thickness of the top layers may not be sufficient to accurately resolve the surface layer when using a fixed-resolution grid (Stacey et al., 1995). To address this issue, most circulation models incorporate the variations of the free-surface throughout the water column, allowing stretching or squeezing to be distributed across all vertical levels. Adcroft and Campin (2004) suggested a treatment which keeps the topography fixed in time while allowing a cleaner separation of the external and internal modes of variability. The vertical advection associated with the external mode is treated in a Lagrangian manner. Consequently, the re-scaling procedure of cell thicknesses due to free-surface variations also applies to the bottom cells, which require special treatment in the presence of penalisation.

In the NEMO model, the vertical scale factors Δz vary in time as a function of the free-surface η . They are expressed as:

$$\Delta z(t) = \Delta z^0 \left(1 + \frac{\eta(t)}{H_0} \right) \quad (\text{IV.1})$$

where Δz^0 represents the initial vertical scale factor and H_0 is the geometric (non-penalised) height of the water column. At time step $n + 1$, around a specific level k , the displacements of the interfaces relative to the initial state are determined as follows:

$$(\Delta h_k)^{n+1} = h_k^0 \left(1 + \frac{\eta^{n+1}}{H_0} \right) - h_k^0 \quad (\text{IV.2a})$$

$$= h_k^0 \frac{\eta^{n+1}}{H_0} \quad (\text{IV.2b})$$

Within the penalised region, the displacement Δh should take into account the penalised surface and the capacities of the cells. In studies by Debreu et al. (2022, 2020), the effective mass is interpolated at each time step based on the profile of porosity ϕ as a function of z , which allows for potential applications of wetting and drying with penalisation. Here, we assume that the oscillations of the free surface in a coarse global configuration are small compared to the entire column of the ocean, allowing us to consider that W-face porosity $\phi_{w,k}$ and volume porosity $\phi_{t,k}$ remain constant around their initial positions. By considering the liquid part of the grid cell, we obtain a balance equation:

$$(\phi_{t,k}\Delta z_k)^{n+1} = (\phi_{w,k}(\Delta h_k)^{n+1} - \phi_{w,k+1}(\Delta h_{k+1})^{n+1}) + (\phi_{t,k}\Delta z_k)^0 \quad (\text{IV.3a})$$

$$= \frac{\eta^{n+1}}{H_0} (\phi_{w,k}h_k^0 - \phi_{w,k+1}h_{k+1}^0) + \phi_{t,k}(\Delta z_k)^0 \quad (\text{IV.3b})$$

We establish a relation for the update of the layer thickness, reminiscent of the expression in Eq. (IV.1):

$$(\phi_{t,k}\Delta z_k)^{n+1} = \Delta z_k^0 \left[\phi_{t,k} + \left(\frac{\phi_{w,k}h_k^0 - \phi_{w,k+1}h_{k+1}^0}{\Delta z_k^0} \right) \frac{\eta^{n+1}}{H_0} \right] \quad (\text{IV.4a})$$

This implementation remains simple to implement and imposes a small computational overhead because it requires only to store one 3D array at the time of the initialisation. Supposing that the free surface is not penalised ($\phi_{w,top} = 1$), the sum across the column of the re-scaled vertical factor $(\phi_{t,k}\Delta z_k)^{n+1}$ provides the mass conservation of the water column:

$$\tilde{H}^{n+1} = \eta^{n+1} + \tilde{H}_0 \quad (\text{IV.5})$$

1.2 A preliminary simulation within ORCA1

We conducted a simulation of the BVP method in a global ocean using a forced ORCA1 configuration. In this preliminary test, we applied the penalisation method to treat the bottom partial cells without using the friction parameter. The vertical grid is stretched following the movement of the free-surface, accordingly to the relation derived in Eq. IV.4a.

In NEMO, the topography of the ORCA1 configuration is defined in a 'domain' file, which contains the horizontal and vertical scale factors for each node (T, U, V, F and W) of the 'C' staggered grid. The file is given as an input for the code and can be modified externally. Hence we built a Python routine to penalise the topography. To make the partial cells porous, the T, U, and V nodes are adjusted to the mid-point in the vertical direction.

Since NEMO already employs a finite volume/finite difference discretisation and handles surface fluxes, integrating the penalised equations into the dynamic core is straightforward. The calculation of the horizontal pressure gradient is also simplified with the penalisation method, as all grid points of a given level remain close to the same depth. This eliminates the need to store 3D arrays at each T, U, V, F, and W nodes. Instead, the depths can be computed

through 1D vertical lists, which vary only through the stretching of the grid with the free-surface (η^{n+1}/H_0 in Eq. IV.4a), and this stretching information can be stored in 2D arrays. This optimisation reduces the number of memory calls and results in a more efficient implementation.

During a 50-year period with a reference time step of 45 minutes, the partial cells treated with the penalisation method are compared with traditional partial cells. Both simulations exhibit similar bottom currents with no significant changes (not shown). However, the reduction in memory access led to a 5% reduction of the computational time.

The straightforward implementation of the BVP method in NEMO opens up possibilities for future simulations that incorporate more realistic penalised topography. Modifying the domain file is simple and can be easily handled through external routines, making it accessible to users. For future configurations that utilise face porosity at W nodes and penalty friction, minimal coding adjustments is also required.

2 Penalising the coastline

2.1 Impact of a smoothed coastline on Rossby waves

To assess the potential effects of smoothing the porosity field on wave propagation and prevent potential damping in the penalised region, we exclude friction in the upcoming study. We consider the two-dimensional penalised shallow water equations with reduced gravity, as presented in (Kevlahan et al., 2015), while applying the standard assumptions for the study of linear wave dynamics of inviscid, homogeneous fluids under rotation (refer to chapter 9 of Cushman-Roisin (2011)). The governing equations are expressed as follows:

$$\partial_t u - (f_0 + \beta y)v = -g' \partial_x \frac{\tilde{\eta}}{\phi} \quad (\text{IV.6a})$$

$$\partial_t v + (f_0 + \beta y)u = -g' \partial_y \frac{\tilde{\eta}}{\phi} \quad (\text{IV.6b})$$

$$\partial_t \tilde{\eta} + H(\partial_x(\phi u) + \partial_y(\phi v)) = 0 \quad (\text{IV.6c})$$

with $\tilde{\eta}(x, y, t) = \phi(x, y)\eta(x, y, t)$ the penalised free-surface, (u, v) the horizontal velocity vector, H the rest-state water column thickness, g' the reduced gravity, and $f = f_0 + \beta y$ the Coriolis parameter defined on a β -plane.

Planetary waves propagation in penalised continuous equations

To investigate the propagation of planetary waves, we begin by decomposing the velocity field into geostrophic and ageostrophic components. Assuming first-order velocities as $u \approx -(g'/f_0)\partial_y\eta$ and $v \approx (g'/f_0)\partial_x\eta$, we substitute these into the momentum equations Eq. (IV.6). Solving for u and v yields:

$$u = -\frac{g'}{f_0}\frac{\partial\eta}{\partial y} - \frac{g'}{f_0^2}\frac{\partial^2\eta}{\partial x\partial t} + \frac{\beta_0 g}{f_0^2}y\frac{\partial\eta}{\partial y} \quad (\text{IV.7a})$$

$$v = +\frac{g'}{f_0}\frac{\partial\eta}{\partial x} - \frac{g'}{f_0^2}\frac{\partial^2\eta}{\partial y\partial t} - \frac{\beta_0 g}{f_0^2}y\frac{\partial\eta}{\partial x} \quad (\text{IV.7b})$$

To incorporate the effects of varying porosity on planetary wave propagation, we assume that the two-dimensional porosity field varies gently in the y direction, we express $\phi(x, y) = \phi_0(1 + \alpha_0 y)$, where ϕ_0 is the mean reference porosity and α_0 the variation slope. Changes in porosity are required to be small, such that $|\alpha_0|L \ll 1$, where L is the horizontal length scale of the motion. As a result, the continuity equation can be simplified to the leading order of α_0 as:

$$\partial_t\eta + H(\partial_x u + \partial_y v + \alpha_0 v) = 0 \quad (\text{IV.8})$$

Substituting Eq. (IV.7) into the continuity equation IV.8 leads to a single equation for surface displacement, as follows:

$$\partial_t\eta - R^2\partial_t\nabla^2\eta + R^2(\alpha_0 f_0 - \beta)\partial_x\eta = 0 \quad (\text{IV.9})$$

Here, ∇^2 is the two-dimensional Laplacian operator, and $R = \sqrt{gH}/f_0$ is the deformation radius. A Fourier type solution $\cos(k_x x + k_y y - \omega t)$ provides the dispersion relation:

$$\omega = (\alpha_0 f_0 - \beta) R^2 \frac{k_x}{1 + R^2(k_x^2 + k_y^2)} \quad (\text{IV.10})$$

with ω the wave frequency and (k_x, k_y) the horizontal wavenumber vector.

In a uniform porous region ($\alpha_0 = 0$), this dispersion relation describes the classical westward drift of planetary waves under the β effect. The analysis of the dispersion relation reveals that both phase and group speeds of planetary waves are preserved within the penalised domain, echoing the results of [Kevlahan et al. \(2015\)](#). On the contrary, a gradient in the porosity field ($\alpha_0 \neq 0$) induces a steering effect similar to topographic waves on the boundary currents. This effectively mimics the presence of a varying topography, creating a bottom slope equal to α_0 . Notably, the smoothing coastline penalisation mask acts to modify the water column depth, akin to the impact of a topography. This finding is intriguing because, in the presence of actual

topography, the phase speed of gravity waves would typically be altered along with a reduction in the internal deformation radius R , which is not the case with the penalisation method proposed by [Kevlahan et al. \(2015\)](#).

In the discrete penalised case

We now investigate how the steering effect, observed in the continuous BVP method, arises in the discrete method formulated on a C-staggered grid. Assuming an exact temporal integration, the discrete formulation of the mass equation [IV.6c](#) is

$$\partial_t(\phi_t \eta) + H(\delta_x(\phi_u u) + \delta_y(\phi_v v)) = 0 \quad (\text{IV.11})$$

Here, the porosities ϕ_t , ϕ_u , and ϕ_v are defined at the centers, as well as at the U and V faces of the cells, respectively. By assuming discrete geostrophic velocities $u = -(g'/f_0)\delta_y \eta$ and $v = (g'/f_0)\delta_x \eta$, we obtain an expression for the displacement of the free surface:

$$\partial_t(\phi_t \eta) + R^2(\delta_y(\phi_v \delta_x \eta) - \delta_x(\phi_u \delta_y \eta)) = 0 \quad (\text{IV.12})$$

This relation shows that fluctuations solely in U-face and V-face porosities introduce an additional term that induce a steering effect. However, when the penalisation is restricted to cell porosities, the occurrence of topographic effect is prevented.

2.2 Numerical applications

To assess the steering effect of penalising the coastline, we compare three cases: two non-penalised simulations with idealised vertical walls—one with a flat bottom (taken as a reference) and one with a sloping bathymetry near the coastline—and a penalised simulation with a flat bottom.

Methods

We consider a similar configuration as presented in Chapter I. Specifically, a reduced gravity shallow water model is employed within a square basin of $L = 2000$ km in size, where an anticyclonic wind stress $\tau = (-\tau_0 \cos(\pi y/L), 0)$ is forcing the active layer. Nonlinear terms are excluded from the dynamic equations.

In a reduced gravity model, where the lowermost layer is assumed to be infinitely deep and motionless, visualising the presence of bathymetry is difficult. To circumvent this, an inverted bottom topography, denoted as b , is applied in the momentum equations, following a simi-

lar approach as described in (Kim & Yoon, 1996). The bathymetry $b(x, y) \geq 0$ comprises a flat seabed in the interior basin connecting to a gentle rise of $\Delta b_0 = 100$ meters near coastlines. The shape of b is determined by the indicator function χ , which smoothly varies between 1 in the interior ocean and 0 outside $[0, L]$. These functions are defined as:

$$\chi(x) = \frac{1}{2} \left(\tanh\left(\frac{x}{\Delta/4}\right) - \tanh\left(\frac{x-L}{\Delta/4}\right) \right) \quad (\text{IV.13a})$$

$$b(x, y) = \Delta b_0 (1 - \min(\chi(x), \chi(y))) \quad (\text{IV.13b})$$

Here, the width parameter Δ controls the size of the transition region, set to twice the spatial grid size ($\Delta x = \Delta y$), ensuring that bathymetry varies over a few grid points.

In absence of penalisation, the equations are formulated as follows:

$$\partial_t h + \text{div}(h\mathbf{u}) = 0 \quad (\text{IV.14a})$$

$$\partial_t \mathbf{u} + f\mathbf{k} \times \mathbf{u} = -g'\nabla(h-b) - r\mathbf{u} + \mathbf{D}_v + \frac{\tau}{\rho_0 h} \quad (\text{IV.14b})$$

where h is the active layer thickness, $\mathbf{u} = (u, v)$ represents the horizontal velocity vector, \mathbf{k} the vertical unit vector, f the Coriolis parameter, g' the reduced gravity, r the friction coefficient, \mathbf{D}_v the diffusion term and ρ_0 the density.

In the penalised case, a flat bottom is considered ($b = 0$) and the reduced gravity shallow water equations are modified following the penalisation method proposed by Kevlahan et al. (2015),

$$\partial_t \tilde{h} + \text{div}(\tilde{h}\mathbf{u}) = 0 \quad (\text{IV.15a})$$

$$\partial_t \mathbf{u} + f\mathbf{k} \times \mathbf{u} = -g'\nabla\left(\frac{\tilde{h}}{\phi}\right) - r\mathbf{u} + \mathbf{D}_v + \frac{\tau}{\rho_0 h} - \sigma\mathbf{u} \quad (\text{IV.15b})$$

where the penalised layer thickness is given by $\tilde{h} = \phi h$, with ϕ representing the porosity, and σ denoting the penalty friction exerted through the porous medium.

To replicate the gentle rise of the topography, the minimum porosity ϕ_{\min} is set to 0.8. The shape of the porosity field coincides with that of b , such that:

$$\phi(x, y) = \phi_{\min} + (1 - \phi_{\min}) \min(\chi(x), \chi(y)) \quad (\text{IV.16a})$$

To accommodate the spreading of the indicator function in the case of penalisation or when considering bathymetry, the computational domain is expanded by a few grid points, and the wind outside is extrapolated to the value at the exact coastline. We use for the numerical simulations the shallow water option (SWE) introduced in the version 4.2 of the NEMO general circulation model (Madec & NEMO System Team, 2022). A second-order Leap Frog Robert-

Asselin integration in time is employed on a uniform mesh, aligned with the straight coastline, with a spatial resolution of $1/4^\circ$. The time step Δt , determined by stability considerations, is set to 15 minutes. The simulation begins from a state of rest with a uniform initial layer thickness of $h = 500$ m throughout the entire basin. Lateral diffusion uses a Laplacian viscosity with a magnitude of $500 \text{ m}^2/\text{s}$, considering free-slip boundary conditions, and is solved under the rotation-divergence stress tensor. The penalty friction term is solved with explicit time integration.

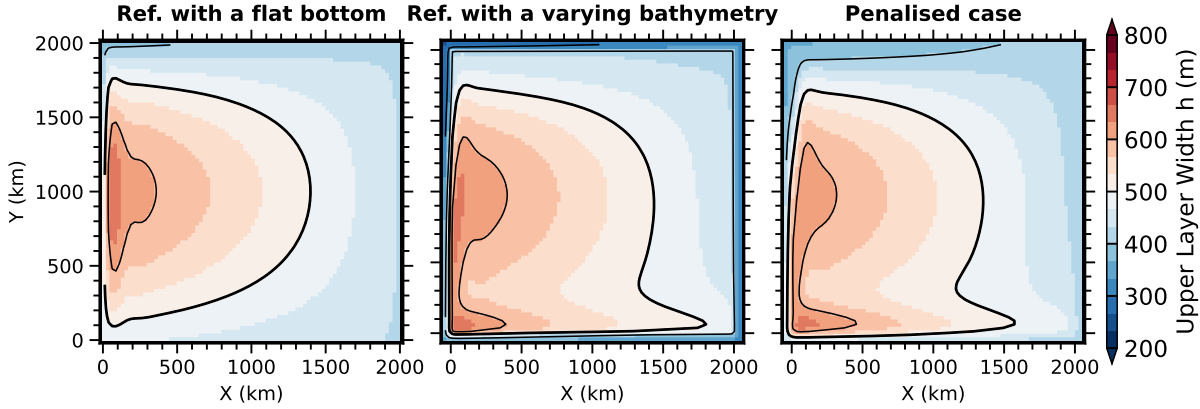


Figure IV.1: Steady state of the linear solutions. Shading and isolines (in black) depict the active layer thickness h (the 500 m isoline is thickened). The left panel shows the reference solution with a flat bottom. The middle panel shows the same solution with varying topography. In the right panel, the coastline is penalised and spread over a few grid points, without friction. Note the similarity between the penalised solution (right panel) and the reference solution with varying topography (middle panel).

Numerical results

Figure IV.1 presents the steady linear solutions for non-penalised simulations with a flat bottom (Figure IV.1a) or a varying topography (Figure IV.1b), as well as the penalised case (Figure IV.1c). The reference solution with a flat bottom (Figure IV.1a) displays the well-known Sverdrup anticyclonic gyre, accompanied by an intensified western boundary current. However, when a slope bottom is introduced, the solution exhibits a small recirculation gyre in the south-west corner of the basin (Figure IV.1b). Additionally, the active layer near the coastline becomes shallower due to the influence of the changing topography, as indicated by the light blue frame in Figure IV.1b. The penalised solution shown in Figure IV.1c presents the same recirculation cell as in the reference case using a varying bathymetry (Figure IV.1b).

To preserve the topographic effect of the spread interface and prevent damping, friction was not included in the penalised solution shown in Figure IV.1c. In Figure IV.2, the frictional parameter is gradually introduced in the porous region, which damps the steering effect induced by the porous coastline (from left to right in Figure IV.2), ultimately approaching the solution without penalisation depicted in Figure IV.1a.

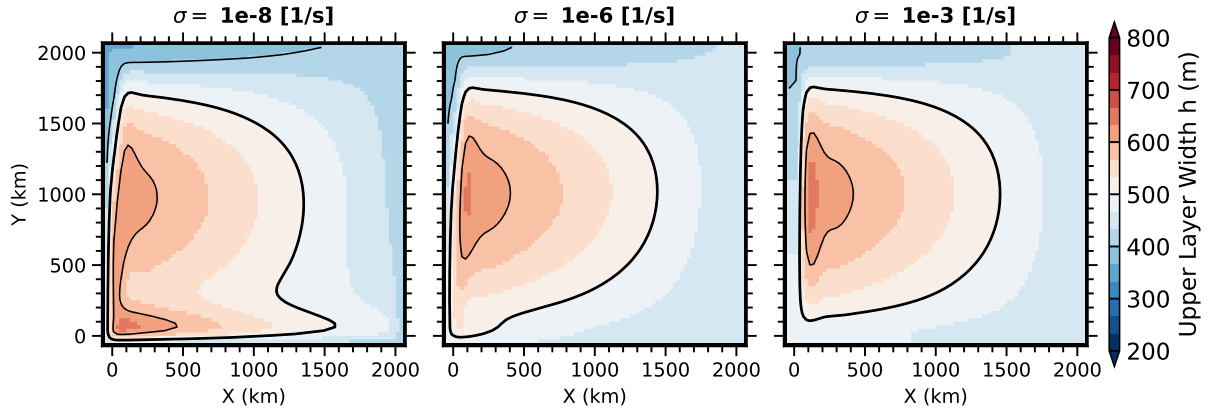


Figure IV.2: Steady state of the linear solutions resorting to the BVP method. Shading and isolines (in black) depict the active layer thickness h (the 500 m isoline is thickened). The coastline is rendered porous and spread over a few points. Friction is added beyond 0km and 2000km and increases from left to right as indicated in the titles above the panels. Notably, the small recirculation gyre in the southwest corner is removed as the penalised region becomes more dissipative.

Hence, results numerical applications that smoothing the penalisation mask along the coastlines induces a topographic steering effect similar to varying bathymetry. Applying high enough friction in the porous region appears to suppress this effect, restoring the idealised solution characterised by vertical walls and a flat bottom.

3 Conclusion

In this chapter, we prepare the application of the BVP method to global configurations. We modify the re-scaled height coordinates (Adcroft & Campin, 2004) to accommodate the penalisation, and investigate the effects of penalised coastlines on the propagation of planetary waves.

We find that the implementation of the BVP method in the re-scaled height coordinates is straightforward and adds minimal computational overhead. Moreover, this implementation is compatible with a penalised coastline, where the free surface at the boundary is modified by the porosity. This opens up the possibility of using the BVP method to represent partially immersed structures, such as mangroves (Marchesiello et al., 2019), by assuming a sub-grid profiling of the porosity.

We performed a preliminary test of the penalisation in an ORCA1 configuration with partial cells. The results highlight the benefits of treating stepped topographies with the penalisation method to simplify and enhance the performance of the code. Although initial testing reveals only moderate changes in the simulated currents with the BVP method, further evalu-

ation in global configurations is essential to fully assess its impact. These tests will contribute to the development of a global configuration that combines the BVP method with an envelope s -coordinate, building upon the work of [Debreu et al. \(2022\)](#).

Furthermore, our results show that penalising the coastlines does not alter the velocity of planetary waves, which is consistent with the findings of [Kevlahan et al. \(2015\)](#). However, we observe a vortex stretching effect in the boundary currents when the penalised coastline is spread, resembling actual topography. Using a high friction helps mitigate the steering effect within the penalised region. However, in coupled coarse-resolution models, the spreading of the coastline poses a challenge as the atmospheric forcing needs to be consistent across the land-sea transition. To address this issue, we propose restricting the application of the Brinkman Volume Penalisation method to bottom topography.

CHAPTER

V

General Conclusion

1 Conclusions

The impacts of artificial topographic steps in z -coordinate ocean circulation models are significant, but our understanding of these impacts is still limited. It is widely recognised that dense currents cascading along step-like slopes experience excessive diapycnal mixing, which deviates from observations. Additionally, the problem of spurious form drag induced by stepped coastlines (or isobaths) was demonstrated by [Adcroft and Marshall \(1998\)](#) and has remained largely unsolved since. The lack of effective solutions to mitigate the adverse effects of stepped topography has motivated the research presented in this thesis.

Using idealised configurations, we conducted a detailed examination of the sensitivity of boundary currents to stepped topography. Specifically, we elucidated long-standing issues associated to staircase-like coastlines, and explored the potential of the Brinkman Volume Penalisation (BVP) method for improved simulation of downslope currents over step-like topography.

The principal results of this thesis are presented around the three key questions that were outlined in the introduction (page 28).

Are there computationally efficient ways to reduce the adverse effects of stepped topographies in OGCMs?

Revisiting the lateral staircase problem shown by [Adcroft and Marshall \(1998\)](#), we examined the sensitivity of boundary currents to indented coastlines (or isobaths).

First, we show that simulated currents are insensitive to step-like coastlines when the model is physically converged; physical convergence meaning that the main characteristics of the flow are not affected by increasing spatial resolution while keeping viscosity and friction parameters constant. In fact, the discrepancies between the solutions solved at $1/4^\circ$ on the aligned and 45° -turned meshes (Figure 3 in chapter I) show that the numerical model is not converged at the resolution of the original problem ($1/4^\circ$). This aspect is often overlooked in z -coordinate numerical studies of boundary representation, where biases in the solutions are usually attributed solely to the presence of steps.

To become insensitive to stepped topography, ocean climate models should ideally achieve physical convergence. Notably, sizeable reductions in spurious mixing have been observed in realistic configurations when increasing spatial resolution while the viscosity was kept unchanged ([Holmes et al., 2021](#); [S. M. Griffies et al., 2000](#)). In many coarse resolution model configurations, it is plausible that the simulated currents are close to physical convergence due to the large viscosity employed for numerical stability. Nonetheless, physical convergence in OGCMs is rarely assessed.

Treatment of momentum advection plays an important role in reducing the sensitivity to steps. Within an idealised overflow (Ilıcak et al., 2012), opting for discrete advection schemes presenting consistency properties improved the conservation of dense water during the downslope flow. The use of higher-order schemes in potentially achieving more accurate solutions near stepped topography is questionable, given that their accuracy order drops near the boundary. However, solutions solved under the energy-*en*strophy conserving (EEN) vorticity scheme showed a faster convergence rate than the energy- (ENE) or *en*strophy- (ENS) conserving schemes within an idealised square basin (chapter I). There is thus potential to achieve more physically converged solutions without increasing spatial resolution.

Second, we show that the application of free-slip as a *true* mirror condition makes step-like coastlines slippery for all numerical formulations. In fact, we find that the accuracy in the usual implementation of the boundary condition varies with the orientation of the grid, thereby explaining the sensitivity to the presence of steps. When the numerical grid is misaligned with the physical shoreline, we show that the implementation of free-slip turns to no-slip when using a symmetric viscous tensor and flux-form advection. In contrast, application of free-slip on step-like topography when using the div-rot viscous tensor and vector-form advection mimics a smooth and straight boundary. Hence, the accuracy in the formulation of the lateral boundary condition determines the response to staircase coastlines (and isobaths).

In cases where stepped topography represents sharp turns, such as a cape leading to retroflexion of boundary currents (Deremble et al., 2016), perfect slipperiness is no longer desirable as it can suppress retroflexion. In such situations, the application of impermeability or no-slip conditions better represents the physical flow-topography interactions compared to free-slip (zero vorticity) boundary conditions. In fact, we find that staircase-like coastlines can be viewed as series of small isolated steps, contributing to the retroflexion of the boundary currents and altering the overall circulation. Therefore, it is expected that the choice of viscous boundary conditions should vary with location to accurately represent both the detachment of boundary currents at a cape and the unperturbed flow along a smooth continuous coastline.

Can Brinkman Volume Penalisation reduce the sensitivity to topographic steps?

In the BVP framework, distributing the no-flow condition across the penalised region leads to smoother bottom currents and reduced spurious mixing. Within an idealised overflow (Ilıcak et al., 2012), we find that spreading the penalised region significantly mitigates the adverse effects of step-like topographic slopes. In addition to this smoother representation of the topography,

one other potential explanation for this improvement could be the increase of the effective order of advection schemes that solve downslope currents, confining the accuracy drop to the lowest porosity region.

We have not yet explored the potential of the BVP method on the sensitivity to lateral steps. However, we believe that boundary currents would likely benefit from its application (Kevlahan et al., 2015). In fact, when applying the BVP method to the square basin configuration of Adcroft and Marshall (1998), we observed that spreading the penalised coastline acts as a topographic slope on the simulated currents, altering the nature of the staircase problem. This mixed representation of the coastline leads us to limit the use of the BVP method to the representation of bottom topographies, thus avoiding the delicate issue in defining the coupling between the ocean and atmosphere over penalised continents in coarse-resolution models.

Is Brinkman Volume Penalisation a viable solution in climate-scale ocean models?

We find that the BVP method is a versatile representation of topography that surpasses the use of shaved cells (Adcroft et al., 1997). Firstly, porous cells capture volume modifications while preserving their alignment with other cells of the mesh, thereby avoiding issues in the calculation of horizontal pressure gradients. Secondly, defining face porosities as the average of adjacent cells ensures a smooth discrete representation of the water column thickness, reducing noise in the barotropic component of circulation (Beckmann & Haidvogel, 1999; Adcroft et al., 1997). Moreover, this framework allows for the use of a penalty friction that, when properly tuned, prevents numerical instabilities when employing the BVP representation. Our initial results demonstrate that the unique ability of the BVP method to spread the porous interface contributes to reducing the spurious effects of stepped topographies.

The development of the BVP method was motivated by its potential for general applicability in numerical models, which raises questions about the restrictions on spatial resolution and time step. We find that the numerical stability for advection when resorting to the BVP method is sensitive to the minimum porosity. We show the numerical stability of the BVP method can be guaranteed by spreading the penalised interface and defining the friction in a purposeful and consistent way. We derive minimal conditions for friction that preserve numerical stability while allowing slippery conditions.

We find that treating stepped topographies with the BVP method can simplify and reduce the computation time of the code. Preliminary tests show only moderate changes in coarse resolution configurations with the BVP method. However, further testing in global configurations is necessary to fully evaluate its impact. Several questions remain regarding the incorporation of penalisation into a global realistic configuration, such as the integration of the penalisation

method with existing parameterisations of overflows, as well as the representation of geothermal fluxes within the penalised region. Finally, this approach easily accommodates complex geometries of the boundary and can be combined with other representations such as the s -coordinate, as shown by [Debreu et al. \(2022\)](#), offering promising avenues for representing topography in ocean circulation models.

The numerical studies conducted during this thesis have led to several changes in NEMO ([Madec & NEMO System Team, 2022](#)). I have introduced into NEMO v4.2 a new module for solving shallow water dynamics (SWE) along with a new testcase (SWG) that reproduces the square basin configuration of [Adcroft and Marshall \(1998\)](#). These additions have served as first steps for incorporating the third-order Runge-Kutta time-stepping scheme into NEMO (Madec et al., in prep). In the forthcoming release of NEMO v5.0, the modified UBS scheme, which is now energy-consistent and incorporates UBS in the vertical advection, will be the default formulation for flux-form advection. Additionally, based on the results obtained in this thesis, the penalisation technique has been chosen for treating partial cells. This choice simplifies the computation in the dynamics and avoids pressure gradient errors in the bottom cells.

2 Perspectives

This thesis has revealed several limitations associated with the representation of topography, highlighting the need for further investigation. The study of the Brinkman Volume Penalisation (BVP) method has also provided valuable insights and promising directions for future research.

Representing unresolved deep passages with the BVP method

In particular, the focus will be on addressing the representation of unresolved deep passages using the BVP method. In climate modelling, the inability to resolve narrow straits due to coarse grid meshes often results in crucial connections between water masses being disrupted. These straits play a critical role in climate simulations, especially for the deep circulation. Currently, two strategies are commonly employed in NEMO: preserving the observed cross-section without affecting the cell volume or introducing additional friction to match the observed transport. However, these approaches are highly specific to individual cases and difficult to generalise.

To overcome these limitations, the 'porous barriers' method developed by [Adcroft \(2013\)](#) provides an objective recognition algorithm, and the BVP method offers a sensible approach for incorporating this method. Accurately capturing the opening of these passages is essential, considering the geostrophic equilibrium of the exchange flow through the basins. One potential solution is to penalise the strait across two cells, while controlling the cross-section and induced drag using porosity and friction, respectively.

To investigate the potential of the BVP method for representing unresolved straits, I developed an idealised NEMO configuration called 'RIDGE' and inspired by [Ferron, Mercier, and Treguier \(2000\)](#). This configuration is depicted in Figure V.1a. It includes a Gaussian bump (in black) separating two basins (in white) connected by an underwater strait in the zonal direction (in grey). The stratification in the west basin, which is slightly denser than the east basin, initiates an exchange flow across the strait. By solving the strait meridionally across two cells, a geostrophic flow can be achieved, as shown in Figure V.1b.

To exploit the benefits of an s -coordinate in resolving bottom flows, topography is represented using a hybrid 'z-on-top-of-s' approach. The s -envelope comprises a Gaussian bump that reaches its peak at the sill level, and the walls of the ridge are superimposed through masking. A similar strategy can be adopted with the BVP method, enabling finer resolution over the width of the strait.

Future work will focus on implementing an s -coordinate combined with the BVP method in a global configuration to accurately represent the ocean geometry below 3000m and improve the simulation of the deep circulation. The impact of opening unresolved passages on the global overturning circulation will be tested through long integrations of the ORCA1 global configuration of NEMO.

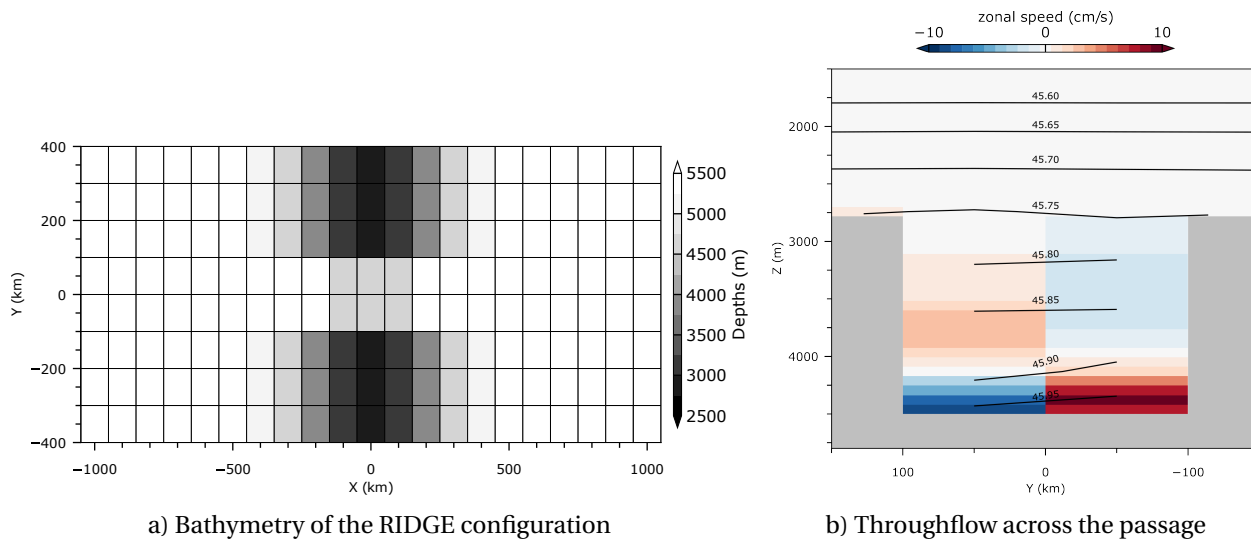


Figure V.1: Description of the RIDGE configuration implemented in NEMO. Panel a illustrates the geometry of the configuration, with depth indicated by black (shallower region) and white (deeper region) shadings. It represents a meridional mid-ocean ridge reaching a maximum depth of 2800m, with an underwater passage of 200km width and a sill at 4500m. The flat abyssal seafloor has a depth of 5500m. Panel b displays the simulated geostrophic flow across the underwater passage, with zonal velocities shaded from red (eastward) to blue (westward). The stratification across the passage is shown by black lines, indicating a sloping of the isopycnals in accordance with the geostrophic currents. Future work will focus on demonstrating the potential of the BVP method for representing underwater passages while enabling control over their actual shape and transport through the use of penalty porosity and friction.

Ice modelling with the BVP method

Despite their significant influence on the ocean circulation, ice shelf cavities around Antarctica are not routinely represented in global ocean and climate models. Modelling of the ice shelf-ocean interface with a z -coordinate system shares some similar difficulties with overflows as excessive diapycnal mixing occurs around steps (Losch, 2008).

Current methods do not allow for a smooth movement of the grounding line and the top boundary of the ice shelf cavities. Additionally, the bedrock topography of Antarctica consists of a network of deep basins connected through sills and covered by ice (Timmermann et al., 2010). The retreat of the grounding line may reveal a geometry that is too fine to be resolved but is essential for modelling and predicting the response of the Antarctic ice sheet and adjacent ocean to global warming.

I plan to apply the BVP method to improve the representation of ice shelf cavities. In the initial phase, I will develop an idealised configuration based on existing studies (Mathiot et al., 2017) and extend the BVP method to incorporate a moving boundary that responds to the melting and freezing along the ice shelf draft. Furthermore, I will incorporate the unresolved bedrock topography using the BVP method, following a similar approach as for representing underwater passages. Subsequently, I will assess the impact of this penalised representation of ice shelf cavities in a realistic eORCA1 configuration, following the approach of Hutchinson et al. (2023).

Breaking the monotony of overflows with the BVP method

Results presented in Chapter III showed that the BVP method offers a promising approach in reducing the spurious mixing occurring during overflows that use a z coordinate. Excessive spreading of the penalised region may not be recommended as the topographic constraint could affect a too large proportion of the ocean. The limited ocean volume means that spreading of the interface should be done carefully, depending on the spatial resolution of the mesh.

A first stage would be to use the idealised overflow configuration presented by Ilıcak et al. (2012) with varying mesh resolution to assess the benefit of penalisation in coarsely or highly resolved overflows. In addition, it would be useful to test the impact of spreading the interface horizontally, vertically or in both directions. The ratio of vertical to horizontal resolution varies widely across OGCM configurations and may play a role in the preservation of dense waters within overflows, as suggested by Winton et al. (1998). Furthermore, the computational cost of vertical grid refinement is substantially less than horizontal refinement, motivating an assessment of each effect.

A second stage would involve testing the impact of the BVP method on overflows in a global NEMO configuration. Additionally, it is tempting to combine penalisation with current overflow parameterisations (e.g., [Beckmann and Döscher \(1997\)](#); [Campin and Goosse \(1999\)](#)). There may be potential synergy in this approach since the spreading of the bottom interface offers a wider stencil for implementing the parameterised advection.

Exploring the impact of curved coastlines

I realised that the curvature of the coastline was overlooked in the usual formulation of the lateral viscous boundary condition. [Verron and Blayo \(1996\)](#) write in their section 2 the vorticity ζ_c at an impermeable boundary regular enough to define in the local frame the vectors (\mathbf{t}, \mathbf{n}) , where \mathbf{t} is tangential to the boundary and \mathbf{n} is directed toward the basin:

$$\zeta_c = \left(\kappa \mathbf{u} - \frac{\partial \mathbf{u}}{\partial \mathbf{n}} \right) \cdot \mathbf{t}, \quad (\text{V.1})$$

with κ the local curvature of the coastline (note that \mathbf{u} is a vector and $\partial \mathbf{u} / \partial \mathbf{n} = \nabla \mathbf{u} \cdot \mathbf{n}$ with $\nabla \mathbf{u}$ the 2×2 Jacobian matrix of \mathbf{u}). Hence, the usual definition of free-slip (zero vorticity) or no-slip (doubled vorticity) align with the definition in Eq.V.1 solely when the coastline is straight ($\kappa = 0$). In other cases ($\kappa \neq 0$), the local curvature of the coastline may act as a source or sink of vorticity depending on the convexity of the coast (sign of κ). A first test for exploring the possible effect of the curvature of the coastline would be to consider a circular closed basin where the curvature of the coastline is controlled by the radius of the basin and the boundary condition is implemented with an immersed boundary method.

Appendix A: Lipschitz condition for vertical advection

The Courant number-dependent method presented by [Shchepetkin \(2015\)](#) solves with implicit temporal integration the fraction of the vertical speed that would exceed the Courant number, if solved explicitly. This approach involves solving a system of equations, which is as large as the number of vertical levels. It is commonly assumed that the necessary condition ensuring the unconditional invertibility of such system is satisfied. However, we are interested in exploring the potential limitations of this condition in the presence of porosity.

The implicit treatment of vertical advection is performed, for conservation, on both mass and momentum transport. For simplicity, we derive the criterion only for tracers, with w_i the vertical velocity corresponding to a fraction of the total velocity w . We call w_e the component solved with explicit integration, such that $w = w_e + w_i$.

The equation for vertical advection and diffusion of a tracer T with penalisation writes

$$\partial_t(\phi_t h T) + h \partial_z(\phi_w w_i T) = \text{RHS} + h \partial_z(\phi_w k_z \partial_z T) \quad (\text{A.2})$$

where z is height (oriented upward). Although the vertical resolution generally varies along the column, for simplicity, we assume Δz to be uniform. An Euler implicit temporal scheme is used, with advection discretised with a first order upstream approach (UP1) and diffusion with centered differencing,

$$\frac{T^{n+1} - T^{n-1}}{2\Delta t} + \text{UP1}\left(\frac{1}{\phi_t} \partial_z(\phi_w w_i^n T^{n+1})\right) = \frac{1}{\phi_t \Delta z} \text{RHS}_k^n + \frac{1}{\phi_t \Delta z} \delta_k \left(\phi_w \frac{k_z}{\Delta z} [\delta_{k+1/2} T^{n+1}] \right) \quad (\text{A.3})$$

with k the vertical indexing increasing with depth, $\delta_{k+1/2}$ the vertical differencing operator, e.g. $\delta_{k+1/2}(T) = T_k - T_{k+1}$. The upstream scheme UP1 writes in its compact form:

$$\text{UP1}\left(\frac{1}{\phi_t} \partial_z(\phi_w w_i T)\right) = \frac{1}{\phi_t \Delta z} \left([\phi_w w_i]_k^- T_{k-1} + \left([\phi_w w_i]_k^+ - [\phi_w w_i]_{k+1}^- \right) T_k - [\phi_w w_i]_{k+1}^+ T_{k+1} \right) \quad (\text{A.4})$$

with $[\phi_w w_i]_k^+ = \max([\phi_w w_i]_k, 0)$ and $[\phi_w w_i]_k^- = \min([\phi_w w_i]_k, 0)$. The overall system to solve expresses as a matrix equation

$$AT^{n+1} = b \quad (\text{A.5})$$

with A a tridiagonal matrix defined by a_d , $-a_i$ and $-a_s$ the principal, inferior and superior diagonals, the tracer vector $T^n = (T_1^n, \dots, T_{k-1}^n, T_k^n, T_{k+1}^n, \dots, T_{N_k}^n)^t$ and the vector $b = (b(k))_k$. The complete system of equation takes the form of

$$-a_i(k)T_{k-1}^{n+1} + a_d(k)T_k^{n+1} - a_s(k)T_{k+1}^{n+1} = b(k) \quad (\text{A.6})$$

where a_d , a_i and a_s express as:

$$a_i(k) = \frac{2\Delta t}{\phi_t \Delta z} [\phi_w w_i]_k^- + \frac{2\Delta t}{\phi_t \Delta z^2} (\phi_w k_z)_{k-1} \quad (\text{A.7})$$

$$a_d(k) = 1 + \frac{2\Delta t}{\phi_t \Delta z} ([\phi_w w_i]_k^+ - [\phi_w w_i]_{k+1}^-) + \frac{2\Delta t}{\phi_t \Delta z^2} ((\phi_w k_z)_{k-1} + (\phi_w k_z)_{k+1}) \quad (\text{A.8})$$

$$a_s(k) = -\frac{2\Delta t}{\phi_t \Delta z} [\phi_w w_i]_{k+1}^+ + \frac{2\Delta t}{\phi_t \Delta z^2} (\phi_w k_z)_{k+1} \quad (\text{A.9})$$

$$b(k) = \frac{2\Delta t}{\phi_t \Delta z} \text{RHS}_k^n + T_k^{n-1} \quad (\text{A.10})$$

The Lipschitz Condition

The Thomas algorithm is widely used to solve tridiagonal systems, which helps reduce the number of operations and enhance computational efficiency. The method remains stable provided the matrix Eq. (A.6) is diagonal dominant, i.e.:

$$\forall k, \quad |a_d(k)| \geq |a_i(k)| + |a_s(k)| \quad (\text{A.11})$$

Omitting the diffusive term, the diagonal dominance condition is:

$$\left| 1 + \frac{2\Delta t}{\phi_t \Delta z} ([\phi_w w_i]_k^+ - [\phi_w w_i]_{k+1}^-) \right| \geq \left| \frac{2\Delta t}{\phi_t \Delta z} [\phi_w w_i]_k^- \right| + \left| \frac{2\Delta t}{\phi_t \Delta z} [\phi_w w_i]_{k+1}^+ \right| \quad (\text{A.12})$$

By dropping the absolute values using the corresponding signs for $[\phi_w w_i]_k^+$ and $[\phi_w w_i]_k^-$, the condition becomes:

$$1 + \frac{2\Delta t}{\phi_t \Delta z} ([\phi_w w_i]_k^+ - [\phi_w w_i]_{k+1}^-) \geq -\frac{2\Delta t}{\phi_t \Delta z} [\phi_w w_i]_k^- + \frac{2\Delta t}{\phi_t \Delta z} [\phi_w w_i]_{k+1}^+ \quad (\text{A.13})$$

Considering that $w_i = w_i^+ + w_i^-$, the condition can be rewritten as:

$$\frac{2\Delta t}{\phi_t \Delta z} \left((\phi_w w_i)_{k+1} - (\phi_w w_i)_k \right) \leq 1 \quad (\text{A.14})$$

Thus, the invertibility criterion writes as the Lipschitz condition for vertical advection:

$$-\frac{2\Delta t}{\phi_t \Delta z} \delta_k(\phi_w w_i) \leq 1 \quad (\text{A.15})$$

This condition imposes a constraint on the negative shear in the implicit velocity w_i . The relation shows that varying porosity could potentially amplify the local shear in vertical velocity, thereby compromising the Lipschitz condition. A similar condition applies to the vertical advection of horizontal momentum u or v . For example, the Lipschitz condition for u with the presence of permeability σ in an implicit integration method can be written as:

$$-2\Delta t \sigma - \frac{2\Delta t}{\phi_u \Delta z} \delta_k(\overline{\phi_w w_i}) \leq 1. \quad (\text{A.16})$$

In this case, the introduction of permeability ($\sigma > 0$) strengthens the diagonal and helps maintain the Lipschitz condition.

Hence, excessive negative shear in the implicit fraction of the vertical current can lead to a non-diagonal dominant invertible system. The results indicate that the violation of the Lipschitz condition can result in potential instabilities in simulations when using the Courant number-dependent treatments proposed by [Shchepetkin \(2015\)](#). There are three separate Lipschitz conditions that need to be satisfied for vertical mass advection and horizontal momentum advection. Moreover, the introduction of porosity can amplify local shear and pose a risk to the stability of the simulation.

To explore the stability of the BVP method concerning the Lipschitz condition, we conducted sensitivity tests within the idealised overflow configuration introduced by [Ilıcak et al., 2012](#)) by evaluating the local shear of w_i and $\overline{w_i}$ (results not shown). However, in all tested cases (section III.3), numerical instabilities likely arise from breaking the CFL condition for advection rather than from the Lipschitz condition. Thus, it remains unclear whether breaking the Lipschitz condition could be detrimental in realistic ocean configuration.

References

- Adcroft, A. (2013, July). Representation of topography by porous barriers and objective interpolation of topographic data. *Ocean Modelling*, 67, 13–27. Retrieved 2020-02-27, from <http://www.sciencedirect.com/science/article/pii/S1463500313000425> doi: 10.1016/j.ocemod.2013.03.002
- Adcroft, A., Anderson, W., Balaji, V., Blanton, C., Bushuk, M., Dufour, C. O., ... Zhang, R. (2019). The GFDL Global Ocean and Sea Ice Model OM4.0: Model Description and Simulation Features. *Journal of Advances in Modeling Earth Systems*, 11(10), 3167–3211. Retrieved 2023-06-29, from <https://onlinelibrary.wiley.com/doi/abs/10.1029/2019MS001726> (eprint: <https://onlinelibrary.wiley.com/doi/pdf/10.1029/2019MS001726>) doi: 10.1029/2019MS001726
- Adcroft, A., & Campin, J.-M. (2004, January). Rescaled height coordinates for accurate representation of free-surface flows in ocean circulation models. *Ocean Modelling*, 7(3), 269–284. Retrieved 2021-02-22, from <https://www.sciencedirect.com/science/article/pii/S1463500303000544> doi: 10.1016/j.ocemod.2003.09.003
- Adcroft, A., Hill, C., & Marshall, J. (1997, September). Representation of Topography by Shaved Cells in a Height Coordinate Ocean Model. *Monthly Weather Review*, 125(9), 2293–2315. Retrieved 2020-02-13, from <https://journals.ametsoc.org/doi/full/10.1175/1520-0493%281997%29125%3C2293%3AROTBSC%3E2.0.CO%3B2> doi: 10.1175/1520-0493(1997)125<2293:ROTBSC>2.0.CO;2
- Adcroft, A., & Marshall, D. (1998, January). How slippery are piecewise-constant coastlines in numerical ocean models? *Tellus A: Dynamic Meteorology and Oceanography*, 50(1), 95–108. Retrieved 2020-02-19, from <https://doi.org/10.3402/tellusa.v50i1.14514> doi: 10.3402/tellusa.v50i1.14514
- Angot, P. (1999). Analysis of singular perturbations on the Brinkman problem for fictitious domain models of viscous flows. *Mathematical Methods in the Applied Sciences*, 22(16), 1395–1412. Retrieved 2020-06-18, from <https://onlinelibrary.wiley.com/doi/abs/10.1002/%28SICI%291099-1476%2819991110%2922%3A16%3C1395%3A%3AAID-MMA84%3E3.0.CO%3B2-3>

- (eprint: <https://onlinelibrary.wiley.com/doi/pdf/10.1002/%28SICI%291099-1476%2819991110%2922%3A16%3C1395%3A%3AAID-MMA84%3E3.0.CO%3B2-3>) doi: 10.1002/(SICI)1099-1476(19991110)22:16<1395::AID-MMA84>3.0.CO;2-3
- Angot, P., Bruneau, C.-H., & Fabrie, P. (1999). A penalization method to take into account obstacles in incompressible viscous flows. *Numerische Mathematik*, 81(4), 497–520. (Publisher: Springer)
- Arakawa, A., & Lamb, V. R. (1977, January). Computational Design of the Basic Dynamical Processes of the UCLA General Circulation Model. In J. Chang (Ed.), *Methods in Computational Physics: Advances in Research and Applications* (Vol. 17, pp. 173–265). Elsevier. Retrieved 2021-01-21, from <http://www.sciencedirect.com/science/article/pii/B9780124608177500094> doi: 10.1016/B978-0-12-460817-7.50009-4
- Barnier, B., Madec, G., Penduff, T., Molines, J.-M., Treguier, A.-M., Le Sommer, J., ... De Cuevas, B. (2006, December). Impact of partial steps and momentum advection schemes in a global ocean circulation model at eddy-permitting resolution. *Ocean Dynamics*, 56(5-6), 543–567. Retrieved 2022-10-04, from <http://link.springer.com/10.1007/s10236-006-0082-1> doi: 10.1007/s10236-006-0082-1
- Beckmann, A., & Döscher, R. (1997, April). A Method for Improved Representation of Dense Water Spreading over Topography in Geopotential-Coordinate Models. *Journal of Physical Oceanography*, 27(4), 581–591. Retrieved 2020-02-07, from <https://journals.ametsoc.org/doi/full/10.1175/1520-0485%281997%29027%3C0581%3AAMFIRO%3E2.0.CO%3B2> doi: 10.1175/1520-0485(1997)027<0581:AMFIRO>2.0.CO;2
- Beckmann, A., & Haidvogel, D. B. (1993, August). Numerical Simulation of Flow around a Tall Isolated Seamount. Part I: Problem Formulation and Model Accuracy. *Journal of Physical Oceanography*, 23(8), 1736–1753. Retrieved 2022-03-03, from https://journals.ametsoc.org/view/journals/phoc/23/8/1520-0485_1993_023_1736_nsofaa_2_0_co_2.xml (Publisher: American Meteorological Society Section: Journal of Physical Oceanography) doi: 10.1175/1520-0485(1993)023<1736:NSOFAA>2.0.CO;2
- Beckmann, A., & Haidvogel, D. B. (1999). *Numerical ocean circulation modeling*. Retrieved 2020-11-23, from <https://b-ok.cc/book/593889/ab7eff>
- Bensiali, B., Chiavassa, G., & Liandrat, J. (2015, October). Penalization of Robin boundary conditions. *Applied Numerical Mathematics*, 96, 134–152. Retrieved 2020-10-06, from <https://linkinghub.elsevier.com/retrieve/pii/S0168927415000902> doi: 10.1016/j.apnum.2015.06.001
- Berann, H. C., Heezen, B. C., & Tharp, M. (1977). [Manuscript painting of Heezen-Tharp "World ocean floor" map by Berann]. Retrieved 2023-07-16, from <https://www.loc.gov/item/2010586277/>

- Bleck, R., & Smith, L. T. (1990). A wind-driven isopycnic coordinate model of the north and equatorial Atlantic Ocean: 1. Model development and supporting experiments. *Journal of Geophysical Research: Oceans*, 95(C3), 3273–3285. Retrieved 2023-03-03, from <https://onlinelibrary.wiley.com/doi/abs/10.1029/JC095iC03p03273> (eprint: <https://onlinelibrary.wiley.com/doi/pdf/10.1029/JC095iC03p03273>) doi: 10.1029/JC095iC03p03273
- Bonaventura, L. (2000, March). A Semi-implicit Semi-Lagrangian Scheme Using the Height Coordinate for a Nonhydrostatic and Fully Elastic Model of Atmospheric Flows. *Journal of Computational Physics*, 158(2), 186–213. Retrieved 2020-07-08, from <https://linkinghub.elsevier.com/retrieve/pii/S0021999199964148> doi: 10.1006/jcph.1999.6414
- Bryan, K., & Cox, M. D. (1967). A numerical investigation of the oceanic general circulation. *Tellus*, 19(1), 54–80. Retrieved 2023-07-14, from <https://onlinelibrary.wiley.com/doi/abs/10.1111/j.2153-3490.1967.tb01459.x> (eprint: <https://onlinelibrary.wiley.com/doi/pdf/10.1111/j.2153-3490.1967.tb01459.x>) doi: 10.1111/j.2153-3490.1967.tb01459.x
- Burridge, D., & Haseler, J. (1977). A model for medium range weather forecasting. *Tech. Rep. No.4, ECMWF*. Retrieved from <https://www.ecmwf.int/en/elibrary/73863-model-medium-range-weather-forecasts-adiabatic-formulation>
- Caltagirone, J.-P. (1994). Sur l'interaction fluide-milieu poreux ; application au calcul des efforts exercés sur un obstacle par un fluide visqueux. *Sur l'interaction fluide-milieu poreux ; application au calcul des efforts exercés sur un obstacle par un fluide visqueux*, 318(5), 571–577. Retrieved from <https://gallica.bnf.fr/ark:/12148/cb343942015/date1994.r> (Place: Paris Publisher: Elsevier)
- Campin, J.-M., & Goosse, H. (1999, January). Parameterization of density-driven downsloping flow for a coarse-resolution ocean model in z-coordinate. *Tellus A: Dynamic Meteorology and Oceanography*, 51(3), 412–430. Retrieved 2021-01-25, from <https://doi.org/10.3402/tellusa.v51i3.13468> (Publisher: Taylor & Francis eprint: <https://doi.org/10.3402/tellusa.v51i3.13468>) doi: 10.3402/tellusa.v51i3.13468
- Colombo, P., Barnier, B., Penduff, T., Chanut, J., Deshayes, J., Molines, J.-M., ... Treguier, A.-M. (2020, July). Representation of the Denmark Strait overflow in a z -coordinate eddy configuration of the NEMO (v3.6) ocean model: resolution and parameter impacts. *Geoscientific Model Development*, 13, 3347–3371. doi: 10.5194/gmd-13-3347-2020
- Cox, M. D. (1979, March). A Numerical Study of Somali Current Eddies. *Journal of Physical Oceanography*, 9(2), 311–326. Retrieved 2021-11-08, from https://journals.ametsoc.org/view/journals/phoc/9/2/1520-0485_1979_009_0311_ansosc_2_0_co_2.xml (Publisher: American Meteorological Society Section: Journal of Physical Oceanography) doi: 10.1175/1520-0485(1979)009<0311:ANSOSC>2.0.CO;2

- Cushman-Roisin, B. (2011). *Introduction to Geophysical Fluid Dynamics* (2nd ed., Vol. 101).
- Dalibard, A.-L., & Gérard-Varet, D. (2011, December). Effective boundary condition at a rough surface starting from a slip condition. *Journal of Differential Equations*, 251(12), 3450–3487. Retrieved 2022-09-08, from <https://www.sciencedirect.com/science/article/pii/S0022039611002683> doi: 10.1016/j.jde.2011.07.017
- Debreu, L., Kevlahan, N. K. R., & Marchesiello, P. (2020, January). Brinkman volume penalization for bathymetry in three-dimensional ocean models. *Ocean Modelling*, 145, 101530. Retrieved 2020-02-07, from <http://www.sciencedirect.com/science/article/pii/S146350031930174X> doi: 10.1016/j.ocemod.2019.101530
- Debreu, L., Kevlahan, N. K. R., & Marchesiello, P. (2022, November). Improved Gulf Stream separation through Brinkman penalization. *Ocean Modelling*, 179, 102121. Retrieved 2022-10-25, from <https://www.sciencedirect.com/science/article/pii/S1463500322001354> doi: 10.1016/j.ocemod.2022.102121
- de Lavergne, C., Madec, G., Roquet, F., Holmes, R. M., & McDougall, T. J. (2017, November). Abyssal ocean overturning shaped by seafloor distribution. *Nature*, 551(7679), 181–186. Retrieved 2021-11-04, from <https://www.nature.com/articles/nature24472> (Bandiera_abtest: a Cg_type: Nature Research Journals Number: 7679 Primary_atype: Research Publisher: Nature Publishing Group Subject_term: Palaeoceanography;Physical oceanography Subject_term_id: palaeoceanography;physical-oceanography) doi: 10.1038/nature24472
- Dengg, J. (1993, October). The Problem of Gulf Stream Separation: A Barotropic Approach. *Journal of Physical Oceanography*, 23(10), 2182–2200. Retrieved 2023-03-07, from https://journals.ametsoc.org/view/journals/phoc/23/10/1520-0485_1993_023_2182_tpgoss_2_0_co_2.xml (Publisher: American Meteorological Society Section: Journal of Physical Oceanography) doi: 10.1175/1520-0485(1993)023<2182:TPOGSS>2.0.CO;2
- Deremble, B., Dewar, W. K., & Chassignet, E. P. (2016, November). Vorticity dynamics near sharp topographic features. *Journal of Marine Research*, 74(6), 249–276. doi: 10.1357/002224016821744142
- Deremble, B., Hogg, A. M., Berloff, P., & Dewar, W. K. (2011, January). On the application of no-slip lateral boundary conditions to ‘coarsely’ resolved ocean models. *Ocean Modelling*, 39(3), 411–415. Retrieved 2021-12-06, from <https://www.sciencedirect.com/science/article/pii/S1463500311000874> doi: 10.1016/j.ocemod.2011.05.002
- Dickson, B., Meincke, J., & Rhines, P. (2008). Arctic–Subarctic Ocean Fluxes: Defining the Role of the Northern Seas in Climate. In R. R. Dickson, J. Meincke, & P. Rhines (Eds.), *Arctic–Subarctic Ocean Fluxes: Defining the Role of the Northern Seas in Climate* (pp. 1–13). Dordrecht: Springer Netherlands. Retrieved 2023-07-02, from https://doi.org/10.1007/978-1-4020-6774-7_1 doi: 10.1007/978-1-4020-6774-7_1

- Downes, S. M., Gnanadesikan, A., Griffies, S. M., & Sarmiento, J. L. (2011, September). Water Mass Exchange in the Southern Ocean in Coupled Climate Models. *Journal of Physical Oceanography*, 41(9), 1756–1771. Retrieved 2023-01-22, from <https://journals.ametsoc.org/view/journals/phoc/41/9/2011jpo4586.1.xml> (Publisher: American Meteorological Society Section: Journal of Physical Oceanography) doi: 10.1175/2011JPO4586.1
- Dupont, F., & Straub, D. N. (2004, January). Effect of a wavy wall on the single gyre Munk problem. *Tellus A: Dynamic Meteorology and Oceanography*, 56(4), 387–399. Retrieved 2021-09-16, from <https://www.tandfonline.com/doi/full/10.3402/tellusa.v56i4.14422> doi: 10.3402/tellusa.v56i4.14422
- Dupont, F., Straub, D. N., & Lin, C. A. (2003, January). Influence of a step-like coastline on the basin scale vorticity budget of mid-latitude gyre models. *Tellus A: Dynamic Meteorology and Oceanography*, 55(3), 255–272. Retrieved 2020-02-20, from <https://doi.org/10.3402/tellusa.v55i3.12094> doi: 10.3402/tellusa.v55i3.12094
- Edwards, C. A., & Pedlosky, J. (1998, December). Dynamics of Nonlinear Cross-Equatorial Flow. Part I: Potential Vorticity Transformation. *Journal of Physical Oceanography*, 28(12), 2382–2406. Retrieved 2021-11-08, from https://journals.ametsoc.org/view/journals/phoc/28/12/1520-0485_1998_028_2382_doncef_2.0.co_2.xml (Publisher: American Meteorological Society Section: Journal of Physical Oceanography) doi: 10.1175/1520-0485(1998)028<2382:DONCEF>2.0.CO;2
- Ezer, T. (2016, August). Revisiting the problem of the Gulf Stream separation: on the representation of topography in ocean models with different types of vertical grids. *Ocean Modelling*, 104, 15–27. Retrieved 2022-10-11, from <https://linkinghub.elsevier.com/retrieve/pii/S1463500316300397> doi: 10.1016/j.ocemod.2016.05.008
- Ferrari, R., Mashayek, A., McDougall, T. J., Nikurashin, M., & Campin, J.-M. (2016, July). Turning Ocean Mixing Upside Down. *Journal of Physical Oceanography*, 46(7), 2239–2261. Retrieved 2023-07-17, from <https://journals.ametsoc.org/view/journals/phoc/46/7/jpo-d-15-0244.1.xml> (Publisher: American Meteorological Society Section: Journal of Physical Oceanography) doi: 10.1175/JPO-D-15-0244.1
- Ferreira, D., Cessi, P., Coxall, H. K., de Boer, A., Dijkstra, H. A., Drijfhout, S. S., ... Wills, R. C. (2018). Atlantic-Pacific Asymmetry in Deep Water Formation. *Annual Review of Earth and Planetary Sciences*, 46(1), 327–352. Retrieved 2023-06-30, from <https://doi.org/10.1146/annurev-earth-082517-010045> (eprint: <https://doi.org/10.1146/annurev-earth-082517-010045>) doi: 10.1146/annurev-earth-082517-010045
- Ferron, B., Mercier, H., Speer, K., Gargett, A., & Polzin, K. (1998). Mixing in the Romanche Fracture Zone. *JOURNAL OF PHYSICAL OCEANOGRAPHY*, 28, 17.

- Ferron, B., Mercier, H., & Treguier, A.-M. (2000, November). Modeling of the bottom water flow through the Romanche Fracture Zone with a primitive equation model- Part I: Dynamics. *Journal of Marine Research*, 58(6), 837–862. Retrieved 2020-11-30, from <http://www.ingentaselect.com/rpsv/cgi-bin/cgi?ini=xref&body=linker&reqdoi=10.1357/002224000763485728> doi: 10.1357/002224000763485728
- Forget, G., & Ferreira, D. (2019, May). Global ocean heat transport dominated by heat export from the tropical Pacific. *Nature Geoscience*, 12(5), 351–354. Retrieved 2023-07-18, from <https://www.nature.com/articles/s41561-019-0333-7> (Number: 5 Publisher: Nature Publishing Group) doi: 10.1038/s41561-019-0333-7
- Gallus, W. A., & Klemp, J. B. (2000, April). Behavior of Flow over Step Orography. *Monthly Weather Review*, 128(4), 1153–1164. Retrieved 2023-05-09, from https://journals.ametsoc.org/view/journals/mwre/128/4/1520-0493_2000_128_1153_bofoso_2.0.co_2.xml (Publisher: American Meteorological Society Section: Monthly Weather Review) doi: 10.1175/1520-0493(2000)128<1153:BOFOSO>2.0.CO;2
- Greenberg, D. A., Dupont, F., Lyard, F. H., Lynch, D. R., & Werner, F. E. (2007, May). Resolution issues in numerical models of oceanic and coastal circulation. *Continental Shelf Research*, 27(9), 1317–1343. Retrieved 2020-10-06, from <https://linkinghub.elsevier.com/retrieve/pii/S0278434307000374> doi: 10.1016/j.csr.2007.01.023
- Griffies, N. Z. a. S. (2012). *The MOM 2012 User Guide*. Retrieved 2023-01-27, from <https://mom-ocean.github.io/docs/userguide/>
- Griffies, S. M. (2004). *Fundamentals of Ocean Climate Models*. Princeton University Press. Retrieved 2023-01-27, from <https://www.jstor.org/stable/j.ctv301gzg> doi: 10.2307/j.ctv301gzg
- Griffies, S. M., Pacanowski, R. C., & Hallberg, R. W. (2000, March). Spurious Diapycnal Mixing Associated with Advection in a z-Coordinate Ocean Model. *Monthly Weather Review*, 128(3), 538–564. Retrieved 2021-01-06, from https://journals.ametsoc.org/view/journals/mwre/128/3/1520-0493_2000_128_0538_sdmawa_2.0.co_2.xml (Publisher: American Meteorological Society Section: Monthly Weather Review) doi: 10.1175/1520-0493(2000)128<0538:SDMAWA>2.0.CO;2
- Griffiths, S. D. (2013, December). Kelvin wave propagation along straight boundaries in C-grid finite-difference models. *Journal of Computational Physics*, 255, 639–659. Retrieved 2020-09-21, from <https://linkinghub.elsevier.com/retrieve/pii/S0021999113005846> doi: 10.1016/j.jcp.2013.08.040
- Guinot, V., Delenne, C., Rousseau, A., & Boutron, O. (2018, December). Flux closures and source term models for shallow water models with depth-dependent integral porosity. *Advances in Water Resources*, 122, 1–26. Retrieved 2020-02-11, from <http://www.sciencedirect.com/science/article/pii/S0309170818300484> doi: 10.1016/j.advwatres.2018.09.014

- Haidvogel, D. B., McWilliams, J. C., & Gent, P. R. (1992, August). Boundary Current Separation in a Quasigeostrophic, Eddy-resolving Ocean Circulation Model. *Journal of Physical Oceanography*, 22(8), 882–902. Retrieved 2023-03-07, from https://journals.ametsoc.org/view/journals/phoc/22/8/1520-0485_1992_022_0882_bcsiaq_2_0_co_2.xml (Publisher: American Meteorological Society Section: Journal of Physical Oceanography) doi: 10.1175/1520-0485(1992)022<0882:BCSIAQ>2.0.CO;2
- Holmes, R. M., Lavergne, C. d., & McDougall, T. J. (2019, October). Tracer Transport within Abyssal Mixing Layers. *Journal of Physical Oceanography*, 49(10), 2669–2695. Retrieved 2022-02-02, from <https://journals.ametsoc.org/view/journals/phoc/49/10/jpo-d-19-0006.1.xml> (Publisher: American Meteorological Society Section: Journal of Physical Oceanography) doi: 10.1175/JPO-D-19-0006.1
- Holmes, R. M., Zika, J. D., Griffies, S. M., Hogg, A. M., Kiss, A. E., & England, M. H. (2021). The Geography of Numerical Mixing in a Suite of Global Ocean Models. *Journal of Advances in Modeling Earth Systems*, 13(7), e2020MS002333. Retrieved 2023-04-06, from <https://onlinelibrary.wiley.com/doi/abs/10.1029/2020MS002333> (eprint: <https://onlinelibrary.wiley.com/doi/pdf/10.1029/2020MS002333>) doi: 10.1029/2020MS002333
- Hughes, C. W., & Cuevas, B. A. d. (2001, October). Why Western Boundary Currents in Realistic Oceans are Inviscid: A Link between Form Stress and Bottom Pressure Torques. *Journal of Physical Oceanography*, 31(10), 2871–2885. Retrieved 2021-12-20, from https://journals.ametsoc.org/view/journals/phoc/31/10/1520-0485_2001_031_2871_wwbcir_2.0.co_2.xml (Publisher: American Meteorological Society Section: Journal of Physical Oceanography) doi: 10.1175/1520-0485(2001)031<2871:WWBCIR>2.0.CO;2
- Hutchinson, K., Deshayes, J., Éthé, C., Rousset, C., de Lavergne, C., Vancoppenolle, M., ... Mathiot, P. (2023, June). Improving Antarctic Bottom Water precursors in NEMO for climate applications. *Geoscientific Model Development*, 16(12), 3629–3650. Retrieved 2023-06-30, from <https://gmd.copernicus.org/articles/16/3629/2023/> (Publisher: Copernicus GmbH) doi: 10.5194/gmd-16-3629-2023
- Ilicak, M., Adcroft, A. J., Griffies, S. M., & Hallberg, R. W. (2012, January). Spurious diapycnal mixing and the role of momentum closure. *Ocean Modelling*, 45-46, 37–58. Retrieved 2019-12-19, from <http://www.sciencedirect.com/science/article/pii/S1463500311001685> doi: 10.1016/j.ocemod.2011.10.003

- Jackson, L., Hughes, C. W., & Williams, R. G. (2006, September). Topographic Control of Basin and Channel Flows: The Role of Bottom Pressure Torques and Friction. *Journal of Physical Oceanography*, 36(9), 1786–1805. Retrieved 2023-03-03, from <https://journals.ametsoc.org/view/journals/phoc/36/9/jpo2936.1.xml> (Publisher: American Meteorological Society Section: Journal of Physical Oceanography) doi: 10.1175/JPO2936.1
- Jullien, S., Caillaud, M., Benshila, R., Bordoïs, L., Cambon, G., Dufois, F., ... Theetten, S. (2022). *Technical and numerical doc CROCO*.
- Kazantsev, E. (2015). Optimized boundary conditions at staircase-shaped coastlines. *Ocean Dynamics*, 15.
- Kevlahan, N. K.-R., Dubos, T., & Aechtner, M. (2015, December). Adaptive wavelet simulation of global ocean dynamics using a new Brinkman volume penalization. *Geoscientific Model Development*, 8(12), 3891–3909. Retrieved 2020-02-18, from <https://www.geoscientific-model-dev.net/8/3891/2015/> doi: <https://doi.org/10.5194/gmd-8-3891-2015>
- Killworth, P. D., & Edwards, N. R. (1999, June). A Turbulent Bottom Boundary Layer Code for Use in Numerical Ocean Models. *Journal of Physical Oceanography*, 29(6), 1221–1238. Retrieved 2023-03-02, from https://journals.ametsoc.org/view/journals/phoc/29/6/1520-0485_1999_029_1221_atbbbc_2.0.co_2.xml (Publisher: American Meteorological Society Section: Journal of Physical Oceanography) doi: 10.1175/1520-0485(1999)029<1221:ATBBLC>2.0.CO;2
- Kim, C.-H., & Yoon, J.-H. (1996, May). Modeling of the wind-driven circulation in the Japan Sea using a reduced gravity model. *Journal of Oceanography*, 52(3), 359–373. Retrieved 2020-10-27, from <https://doi.org/10.1007/BF02235930> doi: 10.1007/BF02235930
- Kösters, F., Käse, R. H., Schmittner, A., & Herrmann, P. (2005). The effect of Denmark Strait overflow on the Atlantic Meridional Overturning Circulation. *Geophysical Research Letters*, 32(4). Retrieved 2023-07-02, from <https://onlinelibrary.wiley.com/doi/abs/10.1029/2004GL022112> (eprint: <https://onlinelibrary.wiley.com/doi/pdf/10.1029/2004GL022112>) doi: 10.1029/2004GL022112
- Laanaia, N., Wirth, A., Molines, J. M., Barnier, B., & Verron, J. (2010, June). On the numerical resolution of the bottom layer in simulations of oceanic gravity currents. *Ocean Science*, 6(2), 563–572. Retrieved 2023-01-20, from <https://os.copernicus.org/articles/6/563/2010/os-6-563-2010.html> (Publisher: Copernicus GmbH) doi: 10.5194/os-6-563-2010
- Lavergne, C. d., Madec, G., Sommer, J. L., Nurser, A. J. G., & Garabato, A. C. N. (2016, February). On the Consumption of Antarctic Bottom Water in the Abyssal Ocean. *Journal of Physical Oceanography*, 46(2), 635–661. Retrieved 2022-11-28, from <https://journals>

- [.ametsoc.org/view/journals/phoc/46/2/jpo-d-14-0201.1.xml](https://journals.ametsoc.org/view/journals/phoc/46/2/jpo-d-14-0201.1.xml) (Publisher: American Meteorological Society Section: Journal of Physical Oceanography) doi: 10.1175/JPO-D-14-0201.1
- Leclair, M., & Madec, G. (2009, January). A conservative leapfrog time stepping method. *Ocean Modelling*, 30(2), 88–94. Retrieved 2021-11-18, from <https://www.sciencedirect.com/science/article/pii/S1463500309001206> doi: 10.1016/j.ocemod.2009.06.006
- Legg, S., Briegleb, B., Chang, Y., Chassignet, E. P., Danabasoglu, G., Ezer, T., ... Yang, J. (2009, May). Improving Oceanic Overflow Representation in Climate Models: The Gravity Current Entrainment Climate Process Team. *Bulletin of the American Meteorological Society*, 90(5), 657–670. Retrieved 2020-09-16, from <http://journals.ametsoc.org/doi/10.1175/2008BAMS2667.1> doi: 10.1175/2008BAMS2667.1
- Legg, S., Hallberg, R. W., & Girton, J. B. (2006). Comparison of entrainment in overflows simulated by z-coordinate, isopycnal and non-hydrostatic models. *Ocean Modelling*, 11(1–2), 69–97. Retrieved 2016-07-22, from <http://www.sciencedirect.com/science/article/pii/S1463500304001064> doi: 10.1016/j.ocemod.2004.11.006
- Legg, S., Jackson, L., & Hallberg, R. W. (2008). Eddy-Resolving Modeling of Overflows. In *Ocean Modeling in an Eddying Regime* (pp. 63–81). American Geophysical Union (AGU). Retrieved 2023-02-28, from <https://onlinelibrary.wiley.com/doi/abs/10.1029/177GM06> (eprint: <https://onlinelibrary.wiley.com/doi/pdf/10.1029/177GM06>) doi: 10.1029/177GM06
- Lemarié, F., Debreu, L., Madec, G., Demange, J., Molines, J., & Honnorat, M. (2015, August). Stability constraints for oceanic numerical models: implications for the formulation of time and space discretizations. *Ocean Modelling*, 92, 124–148. Retrieved 2020-04-20, from <https://linkinghub.elsevier.com/retrieve/pii/S1463500315001055> doi: 10.1016/j.ocemod.2015.06.006
- Lemarié, F., Kurian, J., Shchepetkin, A. F., Jeroen Molemaker, M., Colas, F., & McWilliams, J. C. (2012, January). Are there inescapable issues prohibiting the use of terrain-following coordinates in climate models? *Ocean Modelling*, 42, 57–79. Retrieved 2023-01-23, from <https://www.sciencedirect.com/science/article/pii/S1463500311001831> doi: 10.1016/j.ocemod.2011.11.007
- Le Sommer, J., Penduff, T., Theetten, S., Madec, G., & Barnier, B. (2009, January). How momentum advection schemes influence current-topography interactions at eddy permitting resolution. *Ocean Modelling*, 29(1), 1–14. Retrieved 2021-12-26, from <https://www.sciencedirect.com/science/article/pii/S1463500308001753> doi: 10.1016/j.ocemod.2008.11.007

- Liu, Q., & Vasilyev, O. V. (2007, December). A Brinkman penalization method for compressible flows in complex geometries. *Journal of Computational Physics*, 227(2), 946–966. Retrieved 2020-05-12, from <https://linkinghub.elsevier.com/retrieve/pii/S0021999107003403> doi: 10.1016/j.jcp.2007.07.037
- Losch, M. (2008). Modeling ice shelf cavities in a z coordinate ocean general circulation model. *Journal of Geophysical Research: Oceans*, 113(C8). Retrieved 2023-02-15, from <https://onlinelibrary.wiley.com/doi/abs/10.1029/2007JC004368> (_eprint: <https://onlinelibrary.wiley.com/doi/pdf/10.1029/2007JC004368>) doi: 10.1029/2007JC004368
- Lundquist, K. A., Chow, F. K., & Lundquist, J. K. (2010, March). An Immersed Boundary Method for the Weather Research and Forecasting Model. *Monthly Weather Review*, 138(3), 796–817. Retrieved 2020-07-09, from <https://journals.ametsoc.org/mwr/article/138/3/796/71046/An-Immersed-Boundary-Method-for-the-Weather> doi: 10.1175/2009MWR2990.1
- Lévy, M., Estublier, A., & Madec, G. (2001). Choice of an advection scheme for biogeochemical models. *Geophysical Research Letters*, 28(19), 3725–3728. Retrieved 2023-05-23, from <https://onlinelibrary.wiley.com/doi/abs/10.1029/2001GL012947> (_eprint: <https://onlinelibrary.wiley.com/doi/pdf/10.1029/2001GL012947>) doi: 10.1029/2001GL012947
- MacKinnon, J. A., Johnston, T. M. S., & Pinkel, R. (2008, November). Strong transport and mixing of deep water through the Southwest Indian Ridge. *Nature Geoscience*, 1(11), 755–758. Retrieved 2020-08-19, from <http://www.nature.com/articles/ngeo340> doi: 10.1038/ngeo340
- Madec, G., & Imbard, M. (1996, May). A global ocean mesh to overcome the North Pole singularity. *Climate Dynamics*, 12(6), 381–388. Retrieved 2021-03-17, from <https://doi.org/10.1007/BF00211684> doi: 10.1007/BF00211684
- Madec, G., & NEMO System Team. (2022). *NEMO ocean engine*. Zenodo.
- Magaldi, M. G., Özgökmen, T. M., Griffa, A., Chassignet, E. P., Iskandarani, M., & Peters, H. (2008, January). Turbulent flow regimes behind a coastal cape in a stratified and rotating environment. *Ocean Modelling*, 25(1), 65–82. Retrieved 2022-02-18, from <https://www.sciencedirect.com/science/article/pii/S1463500308000887> doi: 10.1016/j.ocemod.2008.06.006
- Marchand, P. (2014). *Rapport - Vers une meilleure prise en compte de la côte dans les modèles d'océan* (Tech. Rep.). Grenoble, France: LJK.

- Marchesiello, P., Nguyen, N. M., Gratiot, N., Loisel, H., Anthony, E. J., Dinh, C. S., ... Kestenare, E. (2019, June). Erosion of the coastal Mekong delta: Assessing natural against man induced processes. *Continental Shelf Research*, 181, 72–89. Retrieved 2023-07-16, from <https://www.sciencedirect.com/science/article/pii/S0278434318305508> doi: 10.1016/j.csr.2019.05.004
- Mariano, A. J., Chin, T. M., & Özgökmen, T. M. (2003). Stochastic boundary conditions for coastal flow modeling. *Geophysical Research Letters*, 30(9). Retrieved 2023-03-26, from <https://onlinelibrary.wiley.com/doi/abs/10.1029/2003GL016972> (eprint: <https://onlinelibrary.wiley.com/doi/pdf/10.1029/2003GL016972>) doi: 10.1029/2003GL016972
- Marshall, J., & Speer, K. (2012, March). Closure of the meridional overturning circulation through Southern Ocean upwelling. *Nature Geoscience*, 5(3), 171–180. Retrieved 2023-07-18, from <https://www.nature.com/articles/ngeo1391> (Number: 3 Publisher: Nature Publishing Group) doi: 10.1038/ngeo1391
- Masson-Delmotte, V., Zhai, P., Pirani, A., Connors, S. L., Pean, C., Berger, S., ... Zhou, B. (2021). *IPCC, 2021: Climate Change 2021: The Physical Science Basis. Contribution of Working Group I to the Sixth Assessment Report of the Intergovernmental Panel on Climate Change* (Report). Cambridge, UK: Cambridge University Press. Retrieved 2023-07-16, from <https://www.ipcc.ch/report/ar6/wg1/> (ISBN: 9781009157896 Num Pages: 2391)
- Mathiot, P., Jenkins, A., Harris, C., & Madec, G. (2017, July). Explicit representation and parametrised impacts of under ice shelf seas in the Σ^{z} coordinate ocean model NEMO 3.6. *Geoscientific Model Development*, 10(7), 2849–2874. Retrieved 2023-02-15, from <https://gmd.copernicus.org/articles/10/2849/2017/> (Publisher: Copernicus GmbH) doi: 10.5194/gmd-10-2849-2017
- Melet, A., Hallberg, R., Legg, S., & Nikurashin, M. (2014, March). Sensitivity of the Ocean State to Lee Wave–Driven Mixing. *Journal of Physical Oceanography*, 44(3), 900–921. Retrieved 2023-07-18, from <https://journals.ametsoc.org/view/journals/phoc/44/3/jpo-d-13-072.1.xml> (Publisher: American Meteorological Society Section: Journal of Physical Oceanography) doi: 10.1175/JPO-D-13-072.1
- Mittal, R., & Iaccarino, G. (2005). Immersed Boundary Methods. *Annual Review of Fluid Mechanics*, 37(1), 239–261. Retrieved 2023-01-06, from <https://doi.org/10.1146/annurev.fluid.37.061903.175743> (eprint: <https://doi.org/10.1146/annurev.fluid.37.061903.175743>) doi: 10.1146/annurev.fluid.37.061903.175743

- Naveira Garabato, A. C. (2012, December). A perspective on the future of physical oceanography. *Philosophical Transactions of the Royal Society A: Mathematical, Physical and Engineering Sciences*, 370(1980), 5480–5511. Retrieved 2023-07-18, from <https://royalsocietypublishing.org/doi/10.1098/rsta.2012.0400> (Publisher: Royal Society) doi: 10.1098/rsta.2012.0400
- Naveira Garabato, A. C., Nurser, A. J. G., Scott, R. B., & Goff, J. A. (2013, March). The Impact of Small-Scale Topography on the Dynamical Balance of the Ocean. *Journal of Physical Oceanography*, 43(3), 647–668. Retrieved 2023-01-20, from <https://eprints.soton.ac.uk/352263/> (Number: 3) doi: 10.1175/JPO-D-12-056.1
- Pacanowski, R. C., & Gnanadesikan, A. (1998, December). Transient Response in a Z-Level Ocean Model That Resolves Topography with Partial Cells. *Monthly Weather Review*, 126(12), 3248–3270. Retrieved 2022-12-21, from https://journals.ametsoc.org/view/journals/mwre/126/12/1520-0493_1998_126_3248_triazl_2.0.co_2.xml (Publisher: American Meteorological Society Section: Monthly Weather Review) doi: 10.1175/1520-0493(1998)126<3248:TRIAZL>2.0.CO;2
- Pedersen, G. (1986). On the effects of irregular boundaries in finite difference models. *International Journal for Numerical Methods in Fluids*, 6(8), 497–505. Retrieved 2022-01-26, from <https://onlinelibrary.wiley.com/doi/abs/10.1002/fld.1650060802> (eprint: <https://onlinelibrary.wiley.com/doi/pdf/10.1002/fld.1650060802>) doi: 10.1002/fld.1650060802
- Pedlosky, J. (1987). *Geophysical Fluid Dynamics*. Retrieved 2022-02-07, from <https://www.springerprofessional.de/geophysical-fluid-dynamics/13363156>
- Penduff, T., Barnier, B., Kerbiriou, M.-A., & Verron, J. (2002, January). How Topographic Smoothing Contributes to Differences between the Eddy Flows Simulated by Sigma- and Geopotential-Coordinate Models. *Journal of Physical Oceanography*, 32(1), 122–137. Retrieved 2023-05-19, from https://journals.ametsoc.org/view/journals/phoc/32/1/1520-0485_2002_032_0122_htsctd_2.0.co_2.xml (Publisher: American Meteorological Society Section: Journal of Physical Oceanography) doi: 10.1175/1520-0485(2002)032<0122:HTSCTD>2.0.CO;2
- Penduff, T., Le Sommer, J., Barnier, B., Treguier, A.-M., Molines, J.-M., & Madec, G. (2007, December). Influence of numerical schemes on current-topography interactions in 1/4°; global ocean simulations. *Ocean Science*, 3(4), 509–524. Retrieved 2022-07-19, from <https://os.copernicus.org/articles/3/509/2007/> (Publisher: Copernicus GmbH) doi: 10.5194/os-3-509-2007
- Rasmussen, J. T., Cottet, G.-H., & Walther, J. H. (2011, July). A multiresolution remeshed Vortex-In-Cell algorithm using patches. *Journal of Computational Physics*, 230(17), 6742–6755. Retrieved 2023-01-25, from <https://www.sciencedirect.com/science/article/pii/S0021999111003032> doi: 10.1016/j.jcp.2011.05.006

- Reckinger, S. M., Petersen, M. R., & Reckinger, S. J. (2015, December). A study of overflow simulations using MPAS-Ocean: Vertical grids, resolution, and viscosity. *Ocean Modelling*, 96, 291–313. Retrieved 2020-08-20, from <https://linkinghub.elsevier.com/retrieve/pii/S146350031500164X> doi: 10.1016/j.ocemod.2015.09.006
- Reckinger, S. M., Vasilyev, O. V., & Fox-Kemper, B. (2012, August). Adaptive volume penalization for ocean modeling. *Ocean Dynamics*, 62(8), 1201–1215. Retrieved 2020-02-18, from <http://link.springer.com/10.1007/s10236-012-0555-3> doi: 10.1007/s10236-012-0555-3
- Richardson, S. (1973, August). On the no-slip boundary condition. *Journal of Fluid Mechanics*, 59(4), 707–719. Retrieved 2023-03-10, from <https://www.cambridge.org/core/journals/journal-of-fluid-mechanics/article/abs/on-the-noslip-boundary-condition/F276023140D425C047F71EAC8AD46FFA> (Publisher: Cambridge University Press) doi: 10.1017/S0022112073001801
- Riemenschneider, U., & Legg, S. (2007, January). Regional simulations of the Faroe Bank Channel overflow in a level model. *Ocean Modelling*, 17(2), 93–122. Retrieved 2023-01-22, from <https://www.sciencedirect.com/science/article/pii/S146350030700011X> doi: 10.1016/j.ocemod.2007.01.003
- Roquet, F. (2013, February). Dynamical Potential Energy: A New Approach to Ocean Energetics. *Journal of Physical Oceanography*, 43(2), 457–476. Retrieved 2023-06-03, from <https://journals.ametsoc.org/view/journals/phoc/43/2/jpo-d-12-098.1.xml> (Publisher: American Meteorological Society Section: Journal of Physical Oceanography) doi: 10.1175/JPO-D-12-098.1
- Sadourny, R. (1975, April). The Dynamics of Finite-Difference Models of the Shallow-Water Equations. *Journal of the Atmospheric Sciences*, 32(4), 680–689. Retrieved 2020-02-27, from [https://journals.ametsoc.org/doi/abs/10.1175/1520-0469\(1975\)032%3C0680:TDOFDM%3E2.0.CO;2](https://journals.ametsoc.org/doi/abs/10.1175/1520-0469(1975)032%3C0680:TDOFDM%3E2.0.CO;2) (Publisher: American Meteorological Society) doi: 10.1175/1520-0469(1975)032<0680:TDOFDM>2.0.CO;2
- Schoonover, J., Dewar, W., Wienders, N., Gula, J., McWilliams, C., Molemaker, J., ... Yeager, S. (2016). North Atlantic barotropic vorticity balances in numerical models. *Journal of Physical Oceanography*, 289–303. Retrieved 2023-03-28, from <https://opensky.ucar.edu/islandora/object/articles%3A17912/> doi: 10.1175/JPO-D-15-0133.1
- Schwab, D. J., & Beletsky, D. (1998, November). Propagation of Kelvin waves along irregular coastlines in finite-difference models. *Advances in Water Resources*, 22(3), 239–245. Retrieved 2022-01-26, from <https://www.sciencedirect.com/science/article/pii/S0309170898000153> doi: 10.1016/S0309-1708(98)00015-3

- Shapiro, R. (1970). Smoothing, filtering, and boundary effects. *Reviews of Geophysics*, 8(2), 359–387. Retrieved 2020-08-24, from <https://agupubs.onlinelibrary.wiley.com/doi/abs/10.1029/RG008i002p00359> (eprint: <https://agupubs.onlinelibrary.wiley.com/doi/pdf/10.1029/RG008i002p00359>) doi: 10.1029/RG008i002p00359
- Shchepetkin, A. F. (2015, July). An adaptive, Courant-number-dependent implicit scheme for vertical advection in oceanic modeling. *Ocean Modelling*, 91, 38–69. Retrieved 2022-05-18, from <https://linkinghub.elsevier.com/retrieve/pii/S1463500315000530> doi: 10.1016/j.ocemod.2015.03.006
- Smith, M. W. (2014, September). Roughness in the Earth Sciences. *Earth-Science Reviews*, 136, 202–225. Retrieved 2023-07-01, from <https://www.sciencedirect.com/science/article/pii/S0012825214001081> doi: 10.1016/j.earscirev.2014.05.016
- Snow, K., Hogg, A. M., Downes, S. M., Sloyan, B. M., Bates, M. L., & Griffies, S. M. (2015, May). Sensitivity of abyssal water masses to overflow parameterisations. *Ocean Modelling*, 89, 84–103. Retrieved 2023-01-20, from <https://www.sciencedirect.com/science/article/pii/S1463500315000517> doi: 10.1016/j.ocemod.2015.03.004
- Stacey, M. W., Pond, S., & Nowak, Z. P. (1995, June). A Numerical Model of the Circulation in Knight Inlet, British Columbia, Canada. *Journal of Physical Oceanography*, 25(6), 1037–1062. Retrieved 2023-07-16, from https://journals.ametsoc.org/view/journals/phoc/25/6/1520-0485_1995_025_1037_anmotc_2_0_co_2.xml (Publisher: American Meteorological Society Section: Journal of Physical Oceanography) doi: 10.1175/1520-0485(1995)025<1037:ANMOTC>2.0.CO;2
- Steppeler, J. R. (2002). Nonhydrostatic Atmospheric Modeling using a z-Coordinate Representation. *MONTHLY WEATHER REVIEW*, 130, 7.
- Timmermann, R., Le Brocq, A., Deen, T., Domack, E., Dutrieux, P., Galton-Fenzi, B., ... Smith, W. H. F. (2010, December). A consistent data set of Antarctic ice sheet topography, cavity geometry, and global bathymetry. *Earth System Science Data*, 2(2), 261–273. Retrieved 2023-07-20, from <https://essd.copernicus.org/articles/2/261/2010/> (Publisher: Copernicus GmbH) doi: 10.5194/essd-2-261-2010
- Vasilyev, O. V., & Kevlahan, N. K.-R. (2002). Hybrid wavelet collocation–Brinkman penalization method for complex geometry flows. *International Journal for Numerical Methods in Fluids*, 40(3-4), 531–538. Retrieved 2023-01-06, from <https://onlinelibrary.wiley.com/doi/abs/10.1002/fld.307> (eprint: <https://onlinelibrary.wiley.com/doi/pdf/10.1002/fld.307>) doi: 10.1002/fld.307

- Verron, J., & Blayo, E. (1996, September). The No-Slip Condition and Separation of Western Boundary Currents. *Journal of Physical Oceanography*, 26(9), 1938–1951. Retrieved 2020-11-23, from <https://journals.ametsoc.org/jpo/article/26/9/1938/8943/The-No-Slip-Condition-and-Separation-of-Western> (Publisher: American Meteorological Society) doi: 10.1175/1520-0485(1996)026<1938:TNSCAS>2.0.CO;2
- Wang, H., Legg, S. A., & Hallberg, R. W. (2015, February). Representations of the Nordic Seas overflows and their large scale climate impact in coupled models. *Ocean Modelling*, 86, 76–92. Retrieved 2023-02-16, from <https://www.sciencedirect.com/science/article/pii/S1463500314001802> doi: 10.1016/j.ocemod.2014.12.005
- Wang, Q., Danilov, S., & Schröter, J. (2008, January). Comparison of overflow simulations on different vertical grids using the Finite Element Ocean circulation Model. *Ocean Modelling*, 20(4), 313–335. Retrieved 2023-01-27, from <https://www.sciencedirect.com/science/article/pii/S1463500307001291> doi: 10.1016/j.ocemod.2007.10.005
- Warner, S. J., & MacCready, P. (2009, November). Dissecting the Pressure Field in Tidal Flow past a Headland: When Is Form Drag “Real”? *Journal of Physical Oceanography*, 39(11), 2971–2984. Retrieved 2022-02-18, from <https://journals.ametsoc.org/view/journals/phoc/39/11/2009jpo4173.1.xml> (Publisher: American Meteorological Society Section: Journal of Physical Oceanography) doi: 10.1175/2009JPO4173.1
- Winton, M., Hallberg, R., & Gnanadesikan, A. (1998, November). Simulation of Density-Driven Frictional Downslope Flow in Z-Coordinate Ocean Models. *Journal of Physical Oceanography*, 28(11), 2163–2174. Retrieved 2021-12-25, from https://journals.ametsoc.org/view/journals/phoc/28/11/1520-0485_1998_028_2163_soddfd_2.0.co_2.xml (Publisher: American Meteorological Society Section: Journal of Physical Oceanography) doi: 10.1175/1520-0485(1998)028<2163:SODDFD>2.0.CO;2
- Zalesak, S. T. (1979, June). Fully multidimensional flux-corrected transport algorithms for fluids. *Journal of Computational Physics*, 31(3), 335–362. Retrieved 2023-05-23, from <https://www.sciencedirect.com/science/article/pii/0021999179900512> doi: 10.1016/0021-9991(79)90051-2
- Özgökmen, T. M., & Fischer, P. F. (2008, January). On the role of bottom roughness in overflows. *Ocean Modelling*, 20(4), 336–361. Retrieved 2022-09-20, from <https://www.sciencedirect.com/science/article/pii/S1463500307001308> doi: 10.1016/j.ocemod.2007.10.004

